Optical spectroscopy investigation of fiber optic high temperature sensors

Thèse présentée pour l'obtention du grade de
Philosophiae Doctor (Ph.D.)
en Sciences de l'énergie et des matériaux
par

Binod Bastola

Jury d'évaluation

Président du jury	Professeur Luca Razzari
	Université INRS–EMT, Canada
Examinateur externe	Professeur Pablo Bianucci
	Université Concordia, Canada
Examinateur externe	Professeur Florian Hausen
	Université RWTH Aachen, Allemagne
Directeur de recherche	Professeur Andreas Rüdiger
	Université INRS–EMT, Canada

Institut National de la Recherche Scientifique
Énergie Matériaux Télécommunications

Université du Québec 2018

Abstract

Optical Spectroscopy Investigation of Fiber Optic High Temperature Sensors
by Binod Bastola

Optical fibers have become an integral part of our daily life in a variety of applications, most notably in telecommunications and non-invasive medical diagnostics. Derived products, including fiber Bragg gratings (FBGs) extend the field of applications to e.g. temperature and strain sensors that are already beyond the laboratory proof-of-concept level and that hold the promise to transform many areas of industries in an ever increasing number of applications in aerospace, structural integrity monitoring as well as in-site sensing in turbines and reactors. Especially the latter represent a harsh environment which makes the use of electronic sensors either completely impossible or which implies short service intervals. Often these industries employ optical techniques to conduct measurement in the optical fibers themselves, e.g. based on evanescent fields but only a few fiber-based techniques allow for distributed multiplexed sensing. The idea is to operate different sensors along the length of the fiber at different wavelengths, a concept that also capitalizes on the fact that most optical sensors are passive so that the fiber only carries the signal rather than the power supply. The aforementioned points translate into the many advantages of fiber based sensors: reliability, good sensitivity, multiplexing, and low maintenance costs so that in many industries, the technology is now already seen as a worthwhile alternative to established electronic sensors. Optical fibers are immune to electromagnetic field (EMI), compact and can be functionalized. This collaborative dissertation with an industrial partner specialized in developing practical, end–user–focused commercial sensor solutions, is based largely on fiber optic sensing. While the overall project dealt with glass fiber and Fiber Bragg Gratings (FBG) for temperature sensing at elevated temperature and in otherwise harsh environment, the focus of my work is on the physics and material science of FBGs at elevated temperatures.

As typical application example, the atmospheric re–entry, of space vessels exposes materials to extreme thermal conditions under the influence of hypersonic velocity, which lead to critically high temperatures that might affect the structural integrity

and thus the operational safety. These temperatures must therefore be monitored at a high repetition rate with sufficient precision to provide real time feedback to the crew. The reason of choosing optical fiber technology is not only because of fibers being themselves relatively inert but also because they are the ideal choice for long–term monitoring with embedding capability in composite structures. So, the thesis primarily addresses the capability of FBG to track temperatures, a property readily known and thoroughly investigated as such at low and moderate temperatures but which holds a couple of surprises and challenges for temperatures above 300 °C.

Fiber Bragg gratings are periodic refractive index modulations in the core of a fiber for which the Bragg condition is met at a specific wavelength referred to as the Bragg wavelength. This wavelength is reflected and contains information about the grating. The length of this periodic structure is typically a few millimeters while the distance between two maxima of the refractive index modulation is in the range of 500 nm for an FBG matching the C-band of telecom. The permanent change in the physical characteristics with a spatial periodic modulation of the core index of refraction is most commonly created through transversely exposing the fiber core with a UV–beam and using a phase mask to generate an interference pattern of UV–optical field. The temperature sensitivity of the Bragg wavelength depends on the periodicity of the grating and on the effective refractive index of the fiber core. The dominant contribution to this stems from the temperature dependence of refractive index (thermo–optic effect) as compared to the thermal expansion of silica. At high temperatures, the FBG is however unstable which leads to a loss in reflectivity to the point that the signal becomes undetectable.

For specific conditions during the post-fabrication process of the FBG, the reflectivity recovers after a certain time providing what is referred to as a regenerated FBG. These regenerated FBGs have a much better temperature stability but suffer from a substantially reduced reflectivity, typically in the range of 10–15 % of the initial value. While this regeneration process is now widely used, it still lacks fundamental understanding, in particular as the description of FBGs so far relies on a single grating that, once it has been erased, should not regenerate. The fundamental understanding of the regeneration process is furthermore complicated by the complexity of glass as a material system so that e.g., chemical compositions, stress relaxation phenomena, densification etc. are barely understood and models of the underlying mechanisms are still in their infancy. Therefore, in this thesis, I aim at correlating temperature dependent a) FBG parameters with b) *in situ* Raman spectroscopy and c) photoluminescence data to characterize the optical fibers and FBGs and the way fiber parameters (e.g., hydrogen loading, relaxation of the glass,

fiber dopants and stresses) mitigate or impact the FBG regeneration process has been investigated.

In the macroscopic study, an Erbium (Er) broadband source between $1530-1565\,\mathrm{nm}$ is coupled to an optical spectrum analyzer (OSA) through different fibers containing FBGs and their sensing capacities were investigated by monitoring wavelength shifts with changes in temperature. Annealing behavior of gratings in standard telecom grade fibers were investigated with a dedicated setup that allowed for temperature cycles below $1000\,^{\circ}\mathrm{C}$. The linear temperature response is influenced upon heating to $900\,^{\circ}\mathrm{C}$ and subsequent cooling of FBGs back to ambient temperature and the observed temperature sensitivity is determined to be approximately $13\,pm/K$. The calibration curves are obtained to test the characteristics of RFBGs. This was done through a dedicated program in MATLAB to automatically extract all relevant experimental parameters from a time– and temperature–dependent sequence of spectra and led to a new methodology to enhance the recovered reflectivity of FBGs through regeneration between $700-1000°\mathrm{C}$, exceeding the state of the art by over $400\,\%$. The objectives of this work are thus to provide a better understanding of the regeneration mechanism from a phenomenological and microscopic perspective as well as suggestions on how to enhance the performance of regenerated FBGs.

Regarding the methodology, the observation of the key parameters of FBGs was accomplished in collaboration with our industrial partner. I developed a dedicated Matlab code to improve the precision with which critical parameters could be extracted from the large amount of data which allowed me to systematically investigate the peak width that provides a direct handle on the core refractive index modulation. Still, the fundamental question remained about the mechanism of regeneration or in other words, what provides the memory to generate a new grating after the initial one was erased. I address this challenge through the introduction of a second grating that coexists from the very beginning and which is of opposite phase to the first while having a stronger thermal stability. All qualitative observations are covered through this simple model. With respect to the microscopic identification, Raman spectroscopy allowed me to identify fluorine as an undocumented component of the core in GF1B fibers. A comprehensive description of the glass composition, as it would be required to establish a complete microscopic model, is however still out of reach. In order to push for additional indicators at the microscopic level, I exploited the temperature dependence of a strong visible luminescence from the FBG under excitation of a blue cw laser and report on reversible and irreversible contributions of this luminescence.

The two-grating model paves the way towards regeneration efficiencies above $100\,\%$, an exciting perspective worth exploring further. As far as the spectroscopic investigation of the microstructure is concerned, two principle directions should be followed in the near future: for one, it is worthwhile investigating if any of the already observable properties (Raman signature and luminescence) correlates with the regeneration process of FBGs and for the other, it should be possible to extract thermal activation energies for these processes as a fingerprint of defects that can then be compared with independent studies in other fibers and by other experimental techniques.

Publications and conference presentations

[1] **B. Bastola**, B. Fischer, J. Roths, and A. Ruediger, "Qualitative photoluminescence study of Defect activation in telecommunication fibers and Bragg gratings," Optical Materials, vol. 81, pp. 134-139, 2018.

[2] **B. Bastola**, B. Fischer, J. Roths, and A. Ruediger, "Raman microstructural investigation of optical fiber at elevated temperature," Optical Engineering, vol. 56, pp. 097104, 2017.

[3] M. Celikin, D. Barba, **B. Bastola**, A. Ruediger, F. Rosei, "Development of regenerated fiber Bragg grating sensors with long-term stability," Optics Express, vol. 24, pp. 21897, 2016.

[4] **B. Bastola**, B. Fischer, J. Roths, and A. Ruediger, "*In-situ* Raman investigation of optical fiber glass structural changes at high temperature," Proc., Fiber Optic Sensors and Applications XIV, vol. 10208L, 2017 [SPIE Defense + Commercial Sensing, California].

[5] **B. Bastola**, D. Barba, M. Celikin, K. Tagziria, E. Haddad, F. Rosei, and A. Ruediger, "Temperature-dependent Raman spectroscopy studies of fibers," Proc., Photonics and Fiber Technology, vol. JT4A.28, 2016 [OSA Advanced Photonics Congress, Australia].

Résumé en Français (French Abstract)

Étude par spectroscopie optique de capteurs de fibres optiques à températures élevées
par Binod Bastola

Les fibres optiques sont faites de silice (SiO_2), d'oxyde de silicium pur, une sorte de sable ou de quartz raffiné qui peut être dopé par une série de matériaux. Par exemple, le cœur de la plupart des fibres monomode intègre du germanium (Ge) qui donne lieu à un mélange homogène appelé verre germanosilicate. Cela a pour effet de modifier l'indice de réfraction du cœur de la fibre et conséquemment l'absorption et l'émission optique, menant à des changements caractéristiques de la fibre. Ainsi, c'est le système bi-matériel composé du cœur dopé de germanium et de la gaine extérieure de silice, tel que la fibre SMF–28 ou la structure tri-matérielle ayant comme revêtement interne des dopants additionnels tel que la fibre GF1B (se référer au tableau 3.1.1 pour les paramètres importants des différents type des fibres). Ces fibres optiques et ces fibres à réseaux de Bragg (FRBs) qui sont considérées comme des canaux à lumière soit pour un réseau de communication rapide ou pour une illumination, les exploits de la technologie qui promettent au–delà de la preuve de faisabilité en laboratoire, contribuent à transformer plusieurs secteurs d'industries pour un nombre croissant d'applications dans, par exemple, les amplificateurs utilisées en télécommunication, les gyroscopes en fibre optique utilisés en aérospatiale, les capteurs 3D chirurgicaux, les turbines et les réacteurs. Ces industries doivent constamment inspecter leurs installations régulièrement et de manière rentable, entre autres pour une meilleure détection de température et de pression. Très souvent, ils utilisent des techniques de mesures de fibres optiques, exploitant normalement des effets au sujet des limitations des systèmes de télécommunication. Leurs avantages incluent la fiabilité, la rentabilité et, dans plusieurs secteurs, la technique est considérée comme étant plus fiable lorsque exposée à un traitement dur, et ne nécessitant pas de puissance électrique à la tête du capteur. Les fibres optiques sont protégées contre les interférences électromagnétiques, elles sont de petites tailles, ont une haute résolution, et offrent des configurations décentralisées.

Dans cette dissertation collaborative avec l'industrie–partenaire spécialisée de développer des solutions de capteurs commerciaux, pratiques et destinées à l'intention de l'utilisateur final, ce projet, qui est basé principalement sur la détection par les fibres optiques, traite des fibres de verre et des FRBs pour la détection à de hautes températures et dans des environnements rudes, principalement pour des applications en aérospatiale. Durant la rentrée dans l'atmosphère, les matériaux exposés (dotés de bonnes caractéristiques et de bonnes performances aéro–thermo–dynamique) des véhicules spatiaux font face à de sévères charges de chaleur sous l'influence de vitesses hypersoniques, ce qui provoque des augmentations de températures qui peuvent affecter le fonctionnement et, par conséquent le besoin d'une rétroaction en temps réel de la surveillance de l'état étant donné que la température et la déformation sont critiques. Ceci est le contexte où le projet prend la route avec une approche optique fiable connue, le capteur FRB. Le but est, cependant, d'aborder le problème critique de la stabilité du FRB dopé de germanium à haute température (au–delà de 850 °C). Ce projet est entièrement basé sur l'utilisation de recuit thermique de longue durée dans le but d'optimiser un traitement thermique visant à améliorer l'efficacité du capteur de fibre et pour comprendre le mécanisme de régénération du FRB. Le choix du matériau de la fibre optique n'est pas seulement à cause du caractère inerte de la fibre, mais aussi parce que c'est le choix idéal pour la surveillance à long-terme avec capacité de s'imbriquer dans les structures. De ce fait, toute variation de température ou de déformation localement sur la fibre attachée à sa surface peut être immédiatement détectée. La thèse, par contre, entreprend des recherches sur les capteurs de température de FRB pour des applications en aérospatiale étant donné que le procédé d'optimisation pour les applications à hautes températures est critique. Par conséquent, le cœur de la thèse concerne les instabilités de températures associées à a) la réflectivité des FRB et à b) la dépendance en température des matériaux de fibres de verre et des défis reliés à la prise de mesures. Les paragraphes qui suivent détailleront les étapes-clés concernées.

(i) Photosensibilité

L'utilisation de fibres de télécommunication ne requiert non seulement de faibles pertes intrinsèques sur une certaine fenêtre optique mais dans la plupart des cas, elle requiert aussi une certaine photosensibilité de la fibre notamment pour le marquage par UV des FRBs. À cause de la photosensibilité, les propriétés des fibres (notamment l'indice de réfraction du cœur de la fibre) peuvent changer suite à une exposition à la lumière (UV pour la plupart des cas, mais à cause de l'absorption multiphoton, les longueurs d'ondes plus élevées sont aussi admissibles). Dans les fibres de télécommunication courantes, la photosensibilité est atteinte en dopant

le cœur au germanium, même si l'effet de la photosensibilité a déjà été démontré avec d'autres éléments (terres rares). Par l'ajout de germanium pendant le procédé de fabrication (fibrage), des liens $Ge - Si$, $Ge - Ge$ et $Si - Si$, couramment appelés «faux liens» ou «centre déficient germanium–oxygène» (GOCD), sont formés (se référer à la section 1.4). Ces faux liens semblent jouer un rôle important pour l'accroissement de la photosensibilité dans la gamme spectrale des UV à cause du bris des liaisons pendant l'exposition aux UV, ce qui génère des bandes d'absorption réduites. Pour la fabrication des FRB, le pic d'absorption aux alentours de $240\,nm$ (assigné au GeO) est aussi utilisé tout comme le pic d'absorption à $185\,nm$ (assigné au GeO_2) tel que représenté sur la figure 1.4.2. Cependant, pendant l'exposition aux UV, les faux liens se rompent en libérant un électron et en laissant un dénommé ainsi GeE' (atome de Ge ayant un électron lié à trois atomes d'oxygène, voir la figure 1.4.1). Les défauts GeE' semblent constituer le facteur le plus important dans l'augmentation de l'indice de réfraction durant le marquage par UV de la FRB et peuvent être directement corrélés au changement d'indice de réfraction du FRB, tel que représenté à la figure 1.4.3.

Les électrons libérés par le rayonnement UV se déplacent dans la bande de conduction du verre et peuvent être piégés dans les centres F. De plus, les électrons peuvent sauter sur l'atome d'oxygène de la liaison $Ge - O$ et causer la rupture de cette liaison en laissant un atome d'oxygène chargé négativement (centre de trous d'oxygène non liant ou NBOHC, voir la figure 1.4.1) avec un autre défaut GeE' ($\equiv$ Ge˙). Outre cela, durant le processus du fibrage, les faux liens peuvent être rompus par une déformation de traction et il en résulte des radicaux Ge˙Si et Ge˙Ge, qui sont aussi connus sous le nom de défauts induits par fibrage (DID, voir la figure 1.4.1). La quantité de DID croît avec l'augmentation de la vitesse de fibrage durant le processus, ce qui crée des tensions supplémentaires. De plus, la hausse de la vitesse de fibrage diminue la photosensibilité effective de la fibre à cause de la quantité réduite de faux liens.

(ii) Charge en hydrogène

Un autre moyen d'accroître la photosensibilité de la fibre est de charger la fibre avec de l'hydrogène sous haute pression avant l'exposition UV. Durant l'exposition UV, les différents groupes d'hydroxyle (OH), à savoir le $Si - OH$ et le $Ge - OH$, sont formés dans le cœur de la fibre (voir l'équation 1.11), le cœur étant connu pour être de température plus stable (jusqu'à $1200\,°C$), voir la référence 1.4. Ces groupes OH augmentent l'indice de réfraction. Durant l'exposition UV, le Ge est promu à un niveau d'énergie plus élevé. Sans la présence d'hydrogène, le germanium excité

pourrait revenir à son état fondamental après une courte période de temps. Mais, en présence de l'hydrogène, l'état excité réagit avec l'hydrogène pour former un défaut GeE′, un groupe OH et un atome d'hydrogène. Cet atome d'hydrogène peut soit briser les liaisons GeO, qui sont connus pour être plus faibles que les liaisons SiO, pour former plus de défauts GeE′ ou pour réagir avec les défaut GeE′ pour former des hydrates (porteurs d'hydrogène) tel que le GeH, qui lui aussi peut augmenter l'indice de réfraction. Par ailleurs, l'hydrogène peut aussi briser les liaisons Si − O − Si pour former des hydroxyl et des hybrids tel que propose par Shelby, voir la référence 1.4.

Pour améliorer la structuration du réseau, les fibres sont laissées pour être chargées en hydrogène à la température de la pièce dans une chambre à pression élevée qui convienne ($\sim 200\,psi$) pour $120\,heures$. Cette étape de fabrication réduit l'énergie des rayonnements UV requise pour la structuration des FRB, le procédé est appelé passivation étant donné que les liaisons brisées sont passivées par des atomes d'hydrogène dans de la silice amorphe par la réduction de liaisons pendantes qui peuvent modifier la diffusivité et améliorer la modulation de l'indice de réfraction. Après avoir retiré les fibres de la chambre à pression, elles sont entreposées dans un congélateur à $-20\,°C$ pour éviter que l'hydrogène ne diffuse à l'extérieur de la fibre avant le marquage du réseau. Ces travaux collaboratifs sont menés au laboratoire MPB de Montréal et à l'Université de Munich en sciences appliquées en Allemagne. Pour les paramètres des fibres et des paramètres de chargement d'hydrogène, se référer au tableau 3.1.1.

(iii) La photoexposition UV à motifs de franges

Ce projet industriel dépend de a) la structuration à l'échelle submicronique de fibre de verre de silice avec un masque de phase en utilisant des outils d'optique de très haute précision et b) son analyse thermique. Le procédé de fabrication industriel pour graver un réseau d'indice de réfraction qui varie périodiquement dans le cœur d'une fibre utilise un système de gravure latéral en se servant d'un masque de phase très près de la fibre. Le changement permanent en fonction de la modulation de périodicité spatiale de l'indice de réfraction du cœur est créé en exposant le cœur de la fibre à un rayonnement UV à travers un masque de phase afin de générer un patron d'interférence du champ optique UV. Un tel patron d'exposition, qui a une période de $0.5\,\mu s$ produit une réflectivité de $1500\,nm$ dans la bande de fréquences télécom.

Au travers de la collaboration avec les laboratoires MPB à Montréal et à l'Université de Munich en sciences appliquées en Allemagne, le pas du réseau initial (avant atténuation) est gravé soit avec un laser UV à 248 nm ou un laser à 193 nm et typiquement sur une longueur de $\sim$ 10 à 12 mm avec environ 20000 structures périodiques sur une fibre standard en germanosilicate. Pour le marquage, les fibres de 50 cm de long chargées en hydrogène (voir le tableau 3.1.1 pour les propriétés des fibres optiques) sont dénudés mécaniquement au milieu de la fibre sur une longueur approximative de 4 cm. La fibre dénudée est placée parallèlement à une masque de phase avec une distance efficace d'environ 100 um. La lentille de focalisation est installée à 3 mm de son point focal afin de ne pas détruire la fibre par une fluence de radiation élevée. En bougeant le miroir continuellement et avec une exposition laser continue, la longueur du réseau de 12 mm est fabriquée par un seul balayage. Le balayage est nécessaire à cause du profil rectangulaire du faisceau du laser exciplex (environ 3 mm $\times$ 5 mm). Le pic de réflectivité d'un réseau Bragg est maintenu sous surveillance durant le marquage avec un système d'interrogation (micron SM125), typiquement, une bande ayant une réflectivité de 99 % aux alentours d'une longueur d'onde centrale de 1500 nm est atteinte grâce à la longue exposition UV pendant chaque balayage.

(iv) Détection de la température par le réseau de Bragg

La détection par FRB se sert de fibres optiques pour capter les changements physiques via une interaction avec une microstructure résonante (typiquement longue de quelques millimètres dans le cœur de la matrice de silice) d'une fibre monomode. Le principe de fonctionnement est basé sur la détection du décalage en longueur d'onde des signaux rétro–réfléchis dans une étendue spectrale étroite, aussi connu sous le nom de longueur d'onde de Bragg. La sensibilité en température (T) de la longueur d'onde de Bragg (λ_B) dépend de la périodicité du réseau (Λ) et de l'indice de réfraction effective (n_{eff}) du cœur de la fibre ($\lambda_{\mathrm{B}}(T) = 2n_{\mathrm{eff}}(T) \cdot \Lambda(T)$. Le facteur dominant qui contribue à cela est la dépendance en température de l'indice de réfraction induite par effet thermo-optique sur l'expansion thermique de la silice. Le procédé de recuit sur les propriétés du matériau des fibres optiques tend à appliquer cette technique pour la détection de températures très élevées (au–delà de 1000 °C), ce qui définit un nouveau type de FRBs appelés fibres de réseaux de Bragg régénérées (FRBRs). Typiquement, la fabrication de FRBR implique la production d'un pas de réseau initial (avant atténuation) d'un FRB de type–I (se référer à la section2.2.1). Cependant, la fibre optique de base n'est pas un choix approprié pour des applications de température élevées sans compter que les réseaux de type I ne sont pas assez stables pour être opérationnels à de hautes températures et commencent à

atténuer lorsqu'ils sont exposés à des températures au–delà de 300 °C. Mais ces réseaux peuvent être optimisés par un procédé appelé régénération de sorte que les FRBR ont démontré un grand potentiel pour des mesures à hautes températures et en exploitant davantage de propriétés, en particulier en continuant le post-recuit à des températures plus hautes. Le processus de régénération est effectué la plupart du temps par recharge d'hydrogène ou de deutérium de la fibre avant le marquage par UV où les effets de tels facteurs de changement des réseaux qui créent un environnement propice à la régénération sont moins bien compris et le développement de modèles (e.g., modèle de composition chimique, relaxation de stress, densification, etc.) responsables pour des mécanismes sous-jacents et des propriétés dépendantes de la températures associées à ces pièces micro–usinées de verre et de FRBR est au stade de développement. Ainsi, dans cette thèse, le projet traite des techniques optiques qui sont définis sur la base de méthodologies utilisant des techniques macroscopiques phénoménologiques et par la mise en place d'une spectroscopie Raman *in–situ* dépendante de la température pour étudier les fibres optiques et les FRB et la façon dont les paramètres des fibres (e.g., recharge en hydrogène, relaxation du verre, les dopants et les contraintes de la fibre) atténuent ou influencent le processus de régénération.

(v) Phénoménologie macroscopique

L'atténuation thermique dans la capacité de détection des FRB standard (type–I) limite l'utilisation des capteurs à des applications moins critiques à des températures de manœuvre sous 200 °C. Les efforts de la dernière décennie dont mené au développement de nouveaux types de réseaux où les résultats les plus prometteurs sont obtenus pour des capteurs FRBR qui peuvent résister à des températures au-delà de 1000 °C. La fabrication des capteurs de FRBR implique un traitement de recuit post-marquage durant laquelle le signal réfléchi initial subit une atténuation en-dessous du niveau de bruit et par la suite se rattrape à des valeurs inférieures initiales du réseau (typiquement <40 %). Cependant, le mécanisme principal pour le procédé de régénération thermique n'est pas totalement compris, d'où le besoin de développer de nouvelles approches pour augmenter les taux de rattrapage et la stabilité à long terme (qui s'avère cruciale pour des applications en aérospatiale).

Dans les études macroscopiques, la dynamique du processus de régénération thermique est analysée en régénérant isothermiquement à une étendue de température de 700 -1000 °C. Une source laser à bande large en erbium (Er) entre 1530 –1565 nm est couplée à un analyseur de spectres optiques (OSA) ou un ondemètre Burleigh à travers différentes fibres qui contiennent des FRBs et leur capacité de détection

de température est étudiée en surveillant les décalages en longueur d'ondes avec la variation de température en utilisant un montage consacré pour ces mesures. La quasi-linéarité de la réponse de la température est influencée par le chauffage à 900 °C et par le refroidissement subséquent des FRBs à des températures ambiantes et la sensibilité de température observée est approximativement $13\,pm/K$. La réflectivité ne semble pas changer avant que le réseau ne commence à s'atténuer jusqu'à une température maximale durant le cycle de chauffage tandis que la largeur du pic diminue notablement à des températures plus élevées que 300 °C, ce qui n'est pas facile à analyser puisque la méthode qu'on utilise pour extraire la largeur dépend de la forme du pic (étant donné que nous utilisons l'aire autour du maximum d'un pic pour le reconnaître et non sa base). Le délai temporel pour observer le changement dans l'intensité du pic est causé par la dépendance au carré de la tangente hyperbolique (i.e., $tan\,h^2$) en fonction du changement de l'indice de réfraction de la réflectivité. Après un recuit isotherme à 900 °C, la réflectivité et la largeur du pic continuent de diminuer jusqu'à sa complète disparition dans le bruit, ce qui indique que les FRBs s'effacent par un processus activé thermiquement. Après un temps de décroissance de quelques minutes, la réflectivité et la largeur de pic réapparaissent et recommencent à croître jusqu'à ce qu'elles soient suffisamment stabilisées à la valeur maximale, puis se remettent à décroître plus lentement.

À 900 °C, il y a un décalage vers le bleu constant qui affecte la longueur d'onde centrale durant la régénération, ce qui indique qu'en moyenne, la structure de verre a des propriétés altérées qui voient une diminution de l'indice de réfraction du cœur. Les courbes de calibration sont obtenues pour tester les caractéristiques de FRBRs. Ceci a été effectué par un code Matlab qui extrait automatiquement tout paramètre expérimental pertinent par une séquence dépendante en temps et en température des spectres et qui mène à une nouvelle méthodologie pour améliorer la réflectivité des FRBs. Une relation inverse entre la température et l'efficacité de la régénération a été établie (basée sur le fait qu'en ralentissant le processus de régénération, on augmente l'efficacité de restauration du signal). Ceci atteint une efficacité de restauration au-dessus de 85 % du pas de réseau orignal avant atténuation. Surtout, l'avantage d'un cycle de régénération lent est aussi préservé sur des mesures de stabilité à long terme à 1000 °C sur 500 heures, permettant ainsi une application potentielle pour le développement de fibres résistantes à de hautes températures. De plus, une nouvelle approche qui a nous a permis de déterminer l'énergie d'activation du mécanisme de régénération (qui suit une tendance d'Arrhenius) nous a permis de prédire le déclenchement de la régénération du signal réfléchi avec grande précision. Nous discutons des trouvailles expérimentales basées uniquement sur le transport diffusionnel ou sur la densification induite par contrainte étant donné que ces deux effets ont leur

rôle à jouer dans le processus de régénération thermique. Finalement, en prenant la réflectivité et la largeur du pic comme des observables, nous dérivons un modèle simple, phénoménologique et quantitative pourtant capable d'expliquer avec précision le processus de régénération concernant à la fois la disparition et le restauration de la réflectivité de la FRB ce qui nous éclaire sur l'impact de la température sur la structure interne de la fibre de verre dépendante du temps (par exemple, l'indice de réfraction). Plus de détails sont donnés dans le chapitre 4 ci–dessous.

(vi) Mesures Raman *in–situ* et mesures de photoluminescence

Le défi de la spectroscopie optique sur le verre est en rapport avec sa figure de mérite, de faibles pertes en transmission optique, tandis qu'une interaction inélastique est particulièrement utile dans les études en hautes températures et à la base de la plupart des approches spectroscopiques. Les exemples incluent les mesures spectroscopiques en Raman et en photoluminescence des fibres optiques en verre qui sont détectables même à hautes températures cependant, nous choisissions ces approches comme des techniques d'analyses préliminaires dans ces études. a) L'intensité de la diffusion Raman dépend non seulement sur la densité d'états de vibration, mais aussi sur le couplage entre les photons et les vibrations où une diffusion est intrinsèque aux propriétés de la fibre et peut être fonction de la température et de la déformation. La quantité d'énergie perdue par un photon issu d'un laser est vue comme une variation en énergie (fréquence) du photon qui irradie de sorte que cette perte d'énergie est caractéristique pour une liaison particulière dans la structure du verre, appelée signature spectrale. Le décalage en fréquence qui résulte du changement de longueur d'onde peut être repéré par le capteur, où la dépendance en température du signal Raman peut alors être mesurée précisément en fonction de la fréquence d'excitation. b) Dans un autre ordre d'idées, la technique d'émission de photoluminescence est capable de mesurer les caractéristiques du recuit ou encore la dépendance de température des défauts sur une gamme étendue de températures. La bande large de photoluminescence dans le silicate et le verre de germanosilicate qui correspond aux centres de déficiences en oxygène (ODCs), aux centre de trous d'oxygène non liant (NBOHCs), et aux défauts Ge–H induits par l'hydrogène sont bien connus. Ces bandes de photoluminescence qui sont détectés dans la gamme du visible sont produites par des transitions permises de niveaux d'énergie localisées. L'originalité de l'approche dans cette thèse est le fait de faire les mesures à l'*in–situ* et longitudinalement au cœur de la fibre en bénéficiant d'un volume plus grand et d'une longueur d'interaction plus grande des mesures ex–situ des FRBR entreprises précédemment dans notre groupe de recherche, où des cartographies Raman transversales ont été exécutées pour contrôler les centres de défauts dans le cœur

et la gaine extérieure des FRBs, voir la référence [1]. Ces spectres de photoluminescence fournissent des détails des émetteurs de défauts générés dans le cœur de la fibre durant le marquage des FRB de sorte que nos études se concentrent sur les centres de photoluminescence situés dans le cœur et à l'interface cœur-gaine, ainsi l'ensemble des modes qui occupent un volume plus grand interagissent avec l'onde électromagnétique.

Dans ce projet, la première étape de la préparation d'échantillon à une jointure s'accordant bien est obtenue durant le processus de la création d'un clivage net et plat sur les fibres. Cela nécessite l'enlèvement du revêtement et le nettoyage de la surface de la fibre de verre pour s'assurer qu'aucun résidu ne reste sur la fibre dénudée. Ensuite, le sondage implique d'approcher le laser de l'espace (loin de la fibre) à la fibre qui a été placée sur l'unité de lanceur de la fibre (fiber launcher unit), qui contrôle grâce à un micropositionneur dans les trois directions de l'espace dans le but de centrer la fibre pour avoir une efficacité de couplage optimale. Ensuite, cela requiert de garder la portion de la fibre à l'intérieur de la zone de chauffée du four et finalement de focaliser les lentilles du scanner du microscope dans le spectromètre Raman. Les mesures macroscopiques et les mesures Raman *in–situ* ont été effectuées dans une géométrie de transmission sur a) des fibres optiques de verre pur et b) des FRB de type–I dans des fibres chargées en hydrogène du même type. Les détails des paramètres importants des différentes types de fibres qui sont utilisées dans l'étude sont présentés dans le tableau 3.1.1. Un cheminement prometteur vers une compréhension microscopique est la corrélation quantitative des observations macroscopiques telle que la régénération et le contraste d'indice de réfraction avec des traits microscopiques parmi les défauts ponctuels, les défauts étendus et les déformations. La plupart des procédés reliés sont activés thermiquement de sorte que les propriétés dépendantes en température de la luminescence des défauts ponctuels et de la détection Raman des défauts étendus et des déformations donnent une indication du rôle des dopants dans la fibre de verre. Sachant que ces propriétés phénoménales peuvent en définitive aider à comprendre les processus macroscopiques et microscopiques.

Pour des mesures Raman et des mesures de photoluminescence, un laser de $473\,\text{nm}$ avec un mode TEM^{00} est couplé à un spectromètre optique par différentes fibres où le volume occupé par l'ensemble des modes qui est sondé s'étend en dehors du cœur et donc interagit aussi avec la gaine. Les fibres sont alors soumises cycliquement à la température de la pièce et $950\,°C$. La longueur d'onde $473\,\text{nm}$ est loin de toute absorption fondamentale et les intensités utilisées dans ce travail sont environ de deux ordres de grandeur en-dessous de ceux rapportés par des études sur les changements

d'absorption photo–induits. Par une première observation, nous pouvons clairement remarquons une émission de rouge par les fibres dénudées à l'endroit des réseaux de fibres de Bragg. Cette découverte donne un point de départ pour l'assignation des pics de luminescence. En modélisant ce spectre de luminescence avec une Gaussienne et en surveillant l'intensité en fonction de la température, il a été révélé une dégradation activée thermiquement et irréversible de la luminescence associée aux FRBs. Une inspection de plus près de fibres de verre pures sans FRBs a révélé une luminescence légère mais thermiquement stable avec des caractéristiques spectrales similaires. En suivant un comportement d'Arrhenius, les deux types de luminescences permettent un moyen simple pour déterminer les énergies d'activation, ce qui indique soit des défauts différents qui serait à la base de cette émission ou encore des environnements structuraux ou chimiques différents pour le même défaut. Le défi clé de cette série d'expériences est de s'assurer qu'il n'y avait pas de dérive de la température du couplage de la fibre dans le cas contraire, avant chaque mesure, le cœur de la fibre aurait besoin d'être de nouveau aligné. Ceci limite la résolution dans le temps des différents taux de chauffage, permettant uniquement la comparaison qualitative des énergies d'activation entre le premier et le second cycle de chauffage sous u profil de chauffage identique même si leur ratio exact dépendrait toujours des conditions de chauffage. Les activations dépendantes en température dans les fibres ont de grandes chances de dépendre sur un cœur de germanium hautement dopé sur l'influence du co–dopant (e.g., fluor) tandis qu'un dopant quelconque (e.g., phosphore dans la fibre GF1B) ne montre pas d'effet sur la forme des pics de luminescence et du nombre d'onde des pics. Plus de détails sont donnés dans le chapitre 5 ci–dessous.

Les résultats–clés de cette approche potentielle a déjà montré la capacité de pousser plus loin cette technique pour une compréhension plus en profondeur de cette belle pièce de science des matériaux pour le verre, par exemple une perspective d'intégrer l'interférométrie dans notre spectromètre optique existante peut offrir la réflectivité simultanée et des mesures de spectres Raman de la structure du verre sur la régénération des FRBs par réflectivité. Ce projet est déjà en développement à travers des collaborations et un nouvel étudiant qui vient de commencer à travailler dessus pour produire un mémoire de maîtrise sur ce projet.

Acknowledgements

As I am transitioning on the next phase of my career goal – I wanted to take a moment to say "thank you."

My experience has been amazing to work in a passionate team, with the inspiring professors, and my colleagues in INRS-EMT over the past four years. It has been fascinating and educational years for me, and I am proud of being part of such a talented and motivated Nanophotonics team led by my supervisor and mentor, Prof. Andreas Ruediger who's terrifically brainy, generous person with his time, advice and encouragement, because without it I don't believe I'd have gotten this far. I would like to acknowledge for his coaching, phenomenal support and extend my deepest gratitude for the highly competitive NSERC strategic partnership project opportunity, which was also being spearheaded by an industrial sector principal, Emile Haddad from MPB Photonics Inc. I would also like to thank Dr. David Barba from INRS-EMT, Dr. Mert Celikin from University College Dublin, Prof. Johaness Roths and Bennet Fischer from Munich University of Applied Sciences for their potential collaborations, and many, many others for their contributions and support throughout the duration of this thesis. Thank you for all the incredible learnings, memories, and fun. I would like to thank jury committee for a constructive feedback, the contributions were invaluable.

Thanks to all the mentors who guided and taught me, all are remembered. And thank you to my parents, relatives, and friends, who are nearby and miles away yet always made feel as though I make them proud and give me constant inspiration to make them prouder. To my dear wife, Sudha Sharma, my angel – I can't thank you enough for your constant love, and support. I am incredibly excited for what lies ahead!

Contents

Contents

iv

Abbreviations

CCD	-	Charge-Coupled Device
CCG	-	Chemical Composition Grating
CTE	-	Coefficient of Thermal Expansion
DID	-	Drawing-Induced Defect
EMI	-	Electro-Magnetic Interference
FBG	-	Fiber Bragg Grating
fs-Grating	-	Femtosecond Grating
FTIR	-	Fourier-Transform-Infrared
GODC	-	Germanium-Oxygen-Deficient Center
GRIN	-	Gradient Index
IR	-	Infrared
KrF	-	Krypton Fluoride
MM	-	Multimode
NBOHC	-	Non Bridging Oxygen Hole Center
PL	-	Photoluminescence
PM	-	Phasemask
RFBG	-	Regenerated Fiber Bragg Grating
RI	-	Refractive Index
SM	-	Singlemode
TIR	-	Total Internal Reflection
UV	-	Ultra Violet

1 Introduction

Ever since the first demonstration of in-fiber Bragg gratings (FBGs) by Ken Hill in Canada in the year 1978 [2], scientists and materials engineers are pushing the limits potentially well beyond a laboratory and telecommunications interest towards emerging applications. Optical fiber sensors and more specifically FBGs, key telecom-enabling technology, have optical filtering or reflecting ability to eliminate a given narrow frequency band. Their temperature and strain-dependence play a central role in a multitude of applications for temperature and strain monitoring (in aerospace, oil, nuclear, civil engineering, for example) [3–7]. Fiber optic sensing technologies are particularly suitable under the influence of harsh environments, high temperatures for example, but even glass fibers also are subjected to material properties changes and thermal degradation above a few hundred degrees Celsius, thereby limiting applications. In particular, the gratings necessitate thermal stability and enhanced lifetime that can be realized through "regenerated fiber Bragg gratings (RFBG)" [8,9]. RFBG are the elevated temperature induced index-modulation having much of the spectral features of a seed grating [10] that exhibit robust thermal stability like the femtosecond (fs) grating. For restoration of such stable FBGs in optical fiber, H_2-loading and appropriate annealing techniques are required. Therefore, the aim is mainly two-fold focussing on development of FBG for use in the identification of operational safety above 1000°C in collaboration with MPB Technologies Inc. and investigations of the glass structure and their thermal properties.

Recent years have seen tremendous progress in in situ Raman diagnosis of glass to obtain a comprehensive microstructural picture and temperature-dependent properties [11–16]. Understanding of the glass relaxation behavior as well as assessing the stress evolution have substantially progressed by a number of authors [17–23] and in particular, the Raman spectroscopy studies of such amorphous structures already have shown very positive outlook [24–27]. Until recently, most efforts were focused on bulk samples (e.g., silicate glass, germanate glass and melt) but data on optical fiber glass that contain GeO_2 and SiO_2 as the basic materials are sparse so our work defines a status quo on the application of structural probe using *in situ* Raman and photoluminescence (PL) spectroscopy to account for the high temperature instabil-

ities in germanosilicate optical fibers [16].

This thesis is organized in a first part comprising chapters 1–2, and a second part, comprising chapters 3–5. The chapters 1–2 and section 3.6 cover a brief overview and a background on the specialized literature dealing with fiber optic sensors and fiber Bragg gratings. In this, the approach is mainly focused on a selection of relevant works that this thesis aims to clarify. This chapter 1 begins with the glass science basics, the temperature dependence, photosensitivity and the scope of thesis. Chapter 2 includes fiber Bragg grating types and briefly highlight the grating regeneration thereof. Chapter 3 includes a detail background on the materials and the experimental methodologies used in this thesis. Chapters 4 and 5 present the experiments and the results. Chapter 6 draws the conclusions and briefly outlines perspectives for further work.

1.1 Relevance and motivation of project

There is a need for materials in aerospace vehicles with high aero-thermo-dynamic performances and characteristics. During atmospheric re-entry, the exposed materials encounter severe heat load under the influence of hypersonic velocity, which lead to ultra-high temperature field ($>1000°C$). This affects operational safety and monitoring the real time temperature of such critical structures is important. Despite there are issues associated with glass material under such elevated temperature, an innovative optical approach based on fiber optic sensing has the potential to address the concerns for such applications and environments. The main benefits of this approach comprise reliability and low cost and in many industries, now the technique is considered safe. It is immune to EMI, having small size, high resolution, harsh environment capabilities and distributed configurations. One example would be single mode fiber with multiplexed FBGs configuration or distributed temperature sensing (DTS) which could replace between a hundred to thousands of thermocouples.

Regarding the demerits, it comprises the behavior of optical fibers at high temperatures that raises important and unsolved questions regarding the recovery and stabilization of FBGs. When holding a fiber long time continuously above $300°C$ (threshold-like temperature necessary for the onset of regeneration [28]), the FBG reflectivity signal decreases continuously, then disappears on a time scale of a few minutes and is restored at a constant fraction of its nominal value. The dynamics of this phenomenon increase with temperature and remain so far unexplained. These regenerated gratings are robust and sustain repeated cycling at temperatures in excess of $1000°C$ [15]. This PhD project centers on (a) structure-property investi-

gations of the degradation and regeneration processes associated with FBGs above 700°C, and (b) leveraging regeneration process to enable strong gratings suitable for operation above 1000°C. In a, there is still ambiguity about the different mechanisms (e.g., complex atomic diffusion and stress induced densification effects [9, 28], chemical composition gratings - CCG [8, 29], modulation of molecular water in the fiber's core [30]) responsible for grating regeneration and understanding this phenomenon on a microscopic scale is important for many practical reasons I will explain in the following paragraph.

The FBG recovery process consists of a complex processing involving numerous parameters such as gas loading (H_2 or He), UV-inscription power and laser wavelength, the strength of initial (seed) grating and annealing cycle, but also the material properties associated with multitude of fibers available and their composition. This thesis directs the attention to the study focused on RFBGs within hydrogen loaded standard photosensitive optical fibers since this gives the most pronounced stabilization to date and is explored through academic and industrial collaborations. Another field of work in our group is the microscopic investigation by confocal Raman and PL imaging systems, equipped with a laser line ($473 nm$) lower than the Bragg grating periodicity. Some interesting but preliminary results of the very first probing of FBG refractive index modulation [1] by photoluminescence which provided information on the chemical composition of the materials, is motivating. The system is further upgraded with an additional fiber coupling unit to align optical fibers with micrometer resolution, then optical glass scattering between room temperature (RT) and 1000°C is monitored continuously. This non-destructive characterization technique correlates the spectral signature of the Ge-doped core fibers (at various stages of thermal processing) to the regeneration of reflectivity signal determined from phenomenological in-line measurements. By using this technique, we are not only able to see the role of dopants in photosensitive fibers (eventually regeneration behavior), we are able to extract strain, densification and chemical changes as a function of annealing temperature. Therefore, the result discussed, give an unique *in situ* approach to dealing structural or chemical process upon high temperature treatment through (a) observation of extended defects and strain by Raman and (b) temperature dependent reversible and irreversible changes associated to point defects in FBGs and optical fibers by luminescence spectroscopy. For this, the test set-up combines the pre-existing portfolio of spectroscopic technique requiring less than $10K worth of additional equipment.

1.2 Fiber optic sensing basics

Optical fiber based sensing technologies utilizing light-based technology receive a surge of interest thanks to enhanced monitoring, reliability and safety across turbines, reactors, aerospace, medical and power and pipelines, and downhole applications in oil and gas industries, to name but a few. Fiber-based sensors are adopted for an ever increasing number of applications related to temperature and strain sensing constantly replacing electronic sensors (e.g., thermocouple, piezoresistive gauges). Electronic sensors is associated with low signal-to-noise ratio (SNR) due to the transmission of electrical signal along the wires. Thus, when it is exposed to electromagnetic (EM) fields, the electrical cable could behave as an antenna prone to environmental noise into the signal thereby compromising a high level of signal certainty. Multiplexing is another issue with electronic sensors due to band widths. On the other hand, fiber Bragg gratings (FBG) and scattering based fiber optic sensors possess the most prominent features such as small size, immunity to EM-fields and capability for multiplexing. The other advantage is that fiber optic sensing is intrinsically safe due to the lack of electrical parts, however relies on electricity buffered interrogator unit (laser and detector system), which is why an instantaneous collection and analysis of material and structural data has become possible to understand the external environment—temperature, strain, vibration, etc. from miles away. In particular, there is no need for a power supply at the location of measurement.

The phenomenon used to measure temperature, strain or vibration relies on the interaction between light and glass in a optical fiber. The most commonly used mechanism for light guiding in telecommunication and sensing applications is index guiding by total internal reflection (TIR) due to difference in refractive indices (RI) of core and cladding (figure 1.2.1). Other mechanisms are band gap guiding like in microstructured fibers [31].
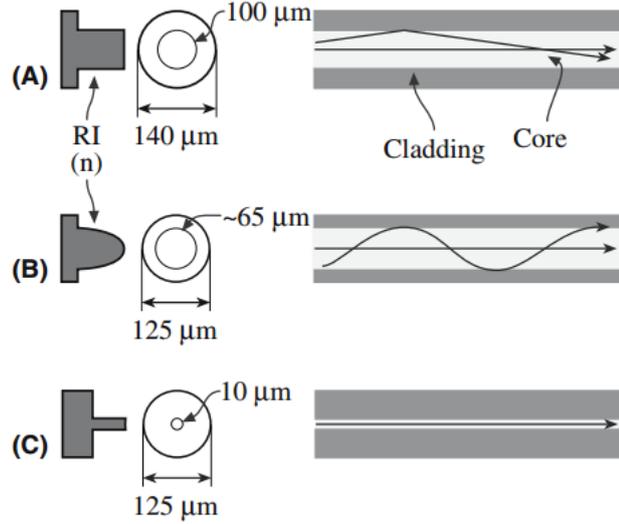
Figure 1.2.1: Different types of TIR in glass fibers, their typical RI distribution and dimensions. **(A)**: Multi mode (MM) step index fiber, **(B)**: Gradient index (GRIN) fiber, **(C)**: Single mode (SM) fiber [32].

Index guided fibers need a higher refractive index in the fiber core, achieved by doping the core with elements like germanium and phosphorus to increase the refractive index or doping the cladding with elements like fluorine and boron which decrease the refractive index [33, 34]. Light guiding in fibers with large core diameters may be explained by TIR with common ray optics. However, in the used SM fibers the core diameter is in the range of the guided mode wavelength thus ray optics by TIR are not a sufficient solution anymore and the light guiding has to be described by wave optics. The propagation of EM waves in waveguides and fibers can be derived from the Maxwell equations leading to the Helmholtz-equation

$$\vec{\nabla}^2 \cdot \vec{E} = \frac{n^2}{c_0{}^2}\frac{\partial^2}{\partial t^2}\vec{E} \tag{1.1}$$

with $\vec{\nabla}^2 = \frac{\partial^2}{\partial x^2} + \frac{\partial^2}{\partial y^2} + \frac{\partial^2}{\partial z^2}$, $\vec{E}$ as the electric field vector, n as the materials refractive index and c_0 as the speed of light in vacuum. While considering glass fibers, it is advantageous to use cylindrical coordinates instead of cartesian coordinates:

$$\Delta U(\rho, \varphi, z) = \vec{\nabla}^2 \cdot U(\rho, \varphi, z) = \frac{1}{\rho}\frac{\partial}{\partial \rho}\left(\rho\frac{\partial U}{\partial \rho}\right) + \frac{1}{\rho^2}\frac{\partial^2 U}{\partial \varphi^2} + \frac{\partial^2 U}{\partial z^2}, \tag{1.2}$$

with U as a placeholder for the electric field vector (same equations can be applied to the magnetic field vector). One of the possible solutions for the electrical field vector is [35]

$$\vec{E}(\rho, \varphi) = (E_t + E_z \cdot \vec{e}_z)e^{-j\beta z}. \tag{1.3}$$

Here, E_t describes the transversal part of the electric field amplitude, E_z describes

the longitudinal part of the electric field amplitude[1], j denotes imaginary number and β is the propagation constant which is defined as

$$\beta = k_0 n_{\text{eff}}, \tag{1.4}$$

with n_{eff} as the effective mode index of the guided wave. This effective mode index is defined as

$$n_{\text{cladding}} < n_{\text{eff}} < n_{\text{core}}. \tag{1.5}$$

It can further be shown [35], that the solution of the wave equation leads to the 'mode constraint' for weak guiding (only refractive index variation, $\Delta n \approx 10^{-3}$):

$$\kappa^2 + \gamma^2 = V^2 \tag{1.6}$$

Here, V^2 is the so called normalized frequency which describes the number of guided modes within the fiber and is given by

$$V = \frac{2\pi r_{\text{core}}}{\lambda_0} \sqrt{n_{\text{core}}^2 - n_{\text{cladding}}^2} = k_0 r_{\text{core}} \text{NA}, \tag{1.7}$$

with λ_0 as the vacuum wavelength, k_0 as the wavenumber, NA as the numerical aperture, n_{core} and n_{cladding} as the refractive index of the core and the cladding, respectively. Single mode guiding is only attainable if the V-parameter is less than 2.405. However, the V-parameter should not be smaller than approx. 1.5. Otherwise high losses may occur if the fiber is disturbed [35]. From equation 1.6 the values of κ and γ can be further expressed as [35]

$$\kappa = r_{\text{core}} \sqrt{k_0^2 n_{\text{core}}^2 - \beta^2} \tag{1.8a}$$

$$\gamma = r_{\text{core}} \sqrt{\beta^2 - k_0^2 n_{\text{cladding}}^2}. \tag{1.8b}$$

1.3 Glass science basics

1.3.1 Structure of glass

Amorphous glasses, like silica (SiO_2) and germania (GeO_2), are one of the most studied binary (MX_2) materials [36, 37]. Amorphous glasses are distinguished from crystalline materials (figure 1.3.1,A) by a nonperiodic atomic structure of randomly distributed tetrahedra (SiO_4) which are arranged as so called rings (figure 1.3.1,B). Additionally, the 3- and 4-membered rings in silica glass are called D2 and D1 defects, respectively.

---

[1]Splitting of the electric field into transversal and longitudinal components is a useful assumption because of the cylindric coordinate system.
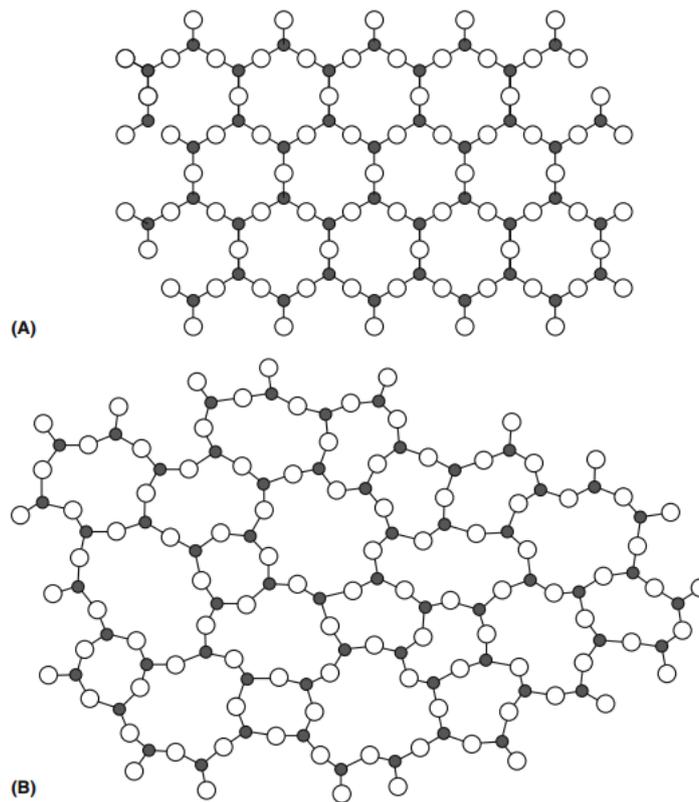
Figure 1.3.1: 2-dimensional structure of crystalline silica **(A)** and amorphous silica **(B)**. White circles represent silicon 4+ ions whereas black dots represent oxygen 2− ions [32].

For the crystalline silica, the molecular bonding angles of the Si-O-Si structure have specific values for each polymorph (e.g. α-quartz = 143.61°) whereas the binding angles for amorphous silica vary between 120° and 180° [36].

1.3.2 Temperature dependence of fiber optic glass properties

Different structures for crystalline glasses (e.g. silica) exist, also known as polymorphs, depending on the athmospheric conditions as temperature and pressure. These polymorphs range from the most common thermodynamically stable α-quartz (rhombohedral crystal symmetry) over α-tridymite (orthorhombic symmetry) to α-cristobalite (tetragonal symmetry) and many other (see figure 1.3.2). Under standard cooling conditions (very slow cooling, low and constant pressure), the glass would crystallize into an α-quartz. If such a sample would be heated, the initial α-quartz would undergo phase changes as depicted in figure 1.3.2 resulting in new forms. Swamy et al. showed that the phase diagram for crystalline and amorphous silica is identical [38]. If a non standard cooling process is used (e.g. rapid cooling of fibers), the glass does not have time to crystallize and hence the melt becomes an amorphous glass (structure depends on the temperature where the melt begins to solidify) [23].
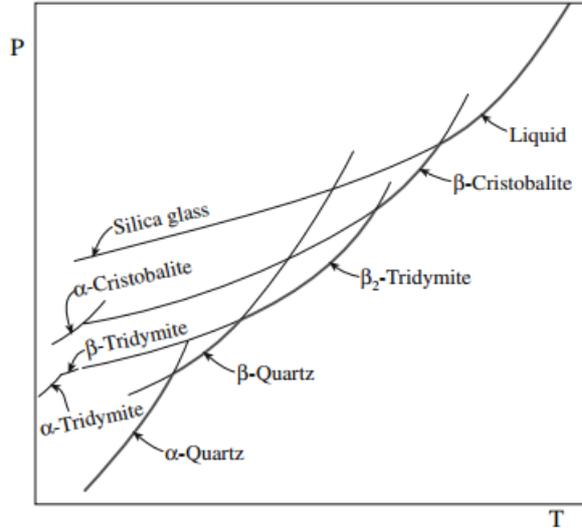
Figure 1.3.2: Phasediagram of SiO_2. At atmospheric pressure, different polymorphs are possible depending on the temperature [32].

These polymorphs have the same chemical composition, but differ in their structure from the tetrahedral arrangement of the SiO_2 to their neighbors resulting in structural changes as density, bonding distance, ring sizes, bonding and rotational angles. During heating, the thermodynamically stable α-quartz is transformed to β-quartz around 573°C which has the same structure as α-quartz but with less distortion. If the glass is heated to higher temperatures (867°C) the β-quartz is transformed to β-tridymite [36].

In case of network modifiers (dopants) added to the glass, the phase diagram changes and polymorphs are formed at different temperatures (decrease of melting point and glass transition temperature due to a disruption of the glass network) and pressures [36]. By adding dopants to the glass, Si-O bonds are ruptured depending on the modifier used [36]. This breakage results in so called bridging oxygens (Si-O-Si) and nonbridging oxygens Si-O$^-$. If the dopant is similiar to silicon, e.g. germanium which forms also GeO_4 tetrahedra and a ring structure, less bonds are broken and silicon in the tetrahedra are randomly substituted with germanium [37]. In addition, by adding germania into the silica network, the small SiO_4 tetrahedral rings form larger mixed rings of GeO_4 and SiO_4 [27], see figure 1.3.3. Amorphous germania consists mainly of 6-membered rings connected to a random network and different bonding angles due to the higher mass of germania [39].
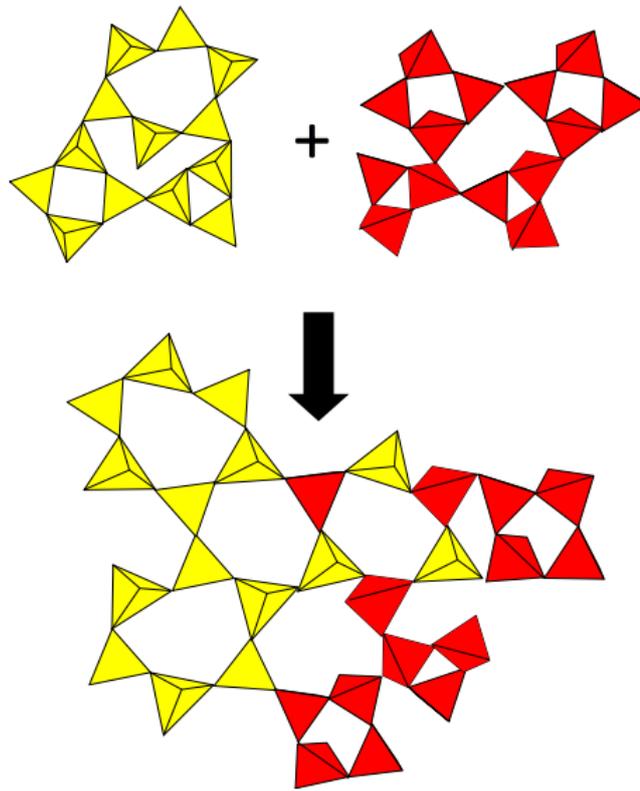
Figure 1.3.3: Formation of mixed rings out of silica (yellow) and germania (red). As the bottom picture illustrates, 6-membered mixed rings are formed, while loosing 3- and 4-membered rings from silica and germania, respectively [27]. Note that this is for illustration and 4-membered rings are very unstable hence they are not very present in the glass network [39].

At higher temperatures, Henderson measured the breakage of mixed rings resulting in 3-membered GeO_4 rings and 6-membered SiO_4 rings [27]. However, by adding different dopants, e.g. fluorine, the glass network becomes less distorted and more stable as the fluorine forms Si-F bonds which are stronger than Si-O bonds. Additionally, fluorine substitutes OH-groups within the glass. Furthermore, the fluorine in the glass encourages structural relaxation during temperature processes [34, 40].

(i) Refractive index (n)

The refractive index is the central optical property and probably the single most important parameter of a fiber material system. The refractive index dictated by the core portion of the irradiated fiber materials with and with out hydrogen loading is different and the FBG regeneration is effected thereof.

(ii) Thermo-optic coefficient ($\frac{dn}{dT}$)

1 Introduction

In a linear regime, the refractive index (n) as a function of temperature, considering T_0 and T as the starting and final temperature respectively, can be expressed as

$$n(T) = n_0 + \frac{dn}{dT}(T - T_0)$$

$$\therefore \frac{dn}{dT} = \frac{n(T) - n_0}{T - T_0}$$

(iii) Coefficient of thermal expansion (CTE)

The coefficient of thermal expansion is a measure of the amount of volume change as a response to temperature or stress applied to a glass. For example, during fiber drawing process the differences in CTE could lead to net tensile stresses across core–cladding interface.

(iv) Fictive and glass transition temperature

For characterization of glasses, the so-called fictive temperature (T_f) is an important parameter. It was introduced by Tool et al. [41] and is mostly used for theoretical calculations and comparison of samples. This temperature depends on the thermal history (e.g. the cooling rate during the fiber drawing process) of a glass and is therefore different for almost each geometry (e.g. fiber or bulk).

The fictive temperature T_f is defined as the temperature at which the extrapolated glass line (which describes the state in which the glass behaves as a solid) intersects the extrapolated liquid line (which describes the state in which the glass behaves as a liquid), see figure 1.3.4. By altering the fictive temperature, the material properties (e.g. density, RI, Young's modulus [23]) of the final glass can be influenced.

Contrary to the fictive temperature, the glass transition temperature T_g is defined as the temperature at which the extrapolated glass line and extrapolated liquid line cross for the minimal cooling rate which is the lowest cooling rate which still results in amorphous glass and not crystalline glasses. At this temperature (T_f, T_g), material properties e.g. the CTE changes dramatically.

For slow cooling rates (fast enough to prevent crystallization) the glass melt starts to solidify in the α-quartz phase at T_g. For faster cooling, the glass melts starts to solidify in a phase different from α-quartz at the fictive temperature. With increasing cooling rates, the solid state curve moves upwards resulting in a higher density as well as another intersection point of the extrapolated lines (T_f).

10
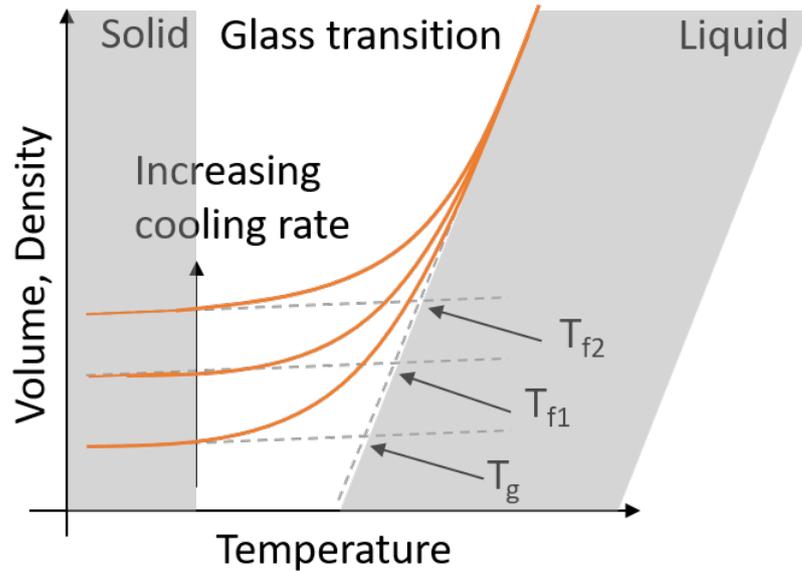
Figure 1.3.4: Dependency of the glass parameters on the temperature during the cooling process. As the temperature decreases the glass goes from its liquid state to the glassy state. The extrapolated lines of both states indicate the glass transition temperature for the minimal cooling rate and the fictive temperature for higher cooling rates [23].

Hence, in order to compare data from literature to measurements the sample needs to have the same thermal history (e.g. commercial products as fibers of the same type). Otherwise, the glasses might have different properties and are not comparable.

1.4 Enhancing photosensitivity

Using a telecommunication fiber for sensing applications does not only require low intrinsic losses at a certain optical window but in most cases also a certain photosensitivity of the fiber e.g. for UV inscription of FBGs. Because of the photosensitivity, fiber properties (e.g. the fiber's core RI) can be altered by exposure to light[2]. In common telecommunication fibers, the photosensitivity is achieved by doping the core with germanium, even though the effect of photosensitivity was already shown with other (rare-earth) elements [43, 44]. By adding of germanium during the fiber manufacturing process (fiber drawing), $Ge - Si$, $Ge - Ge$ and $Si - Si$ bonds are formed which are so-called "wrong bonds" or germanium-oxygen deficient-center (GODC), respectively (see figure 1.4.1).

---

[2]In most cases UV light but also possible at higher wavelengths due to multiphoton absorption (e.g. $480\,\mathrm{nm}$ [42])

11
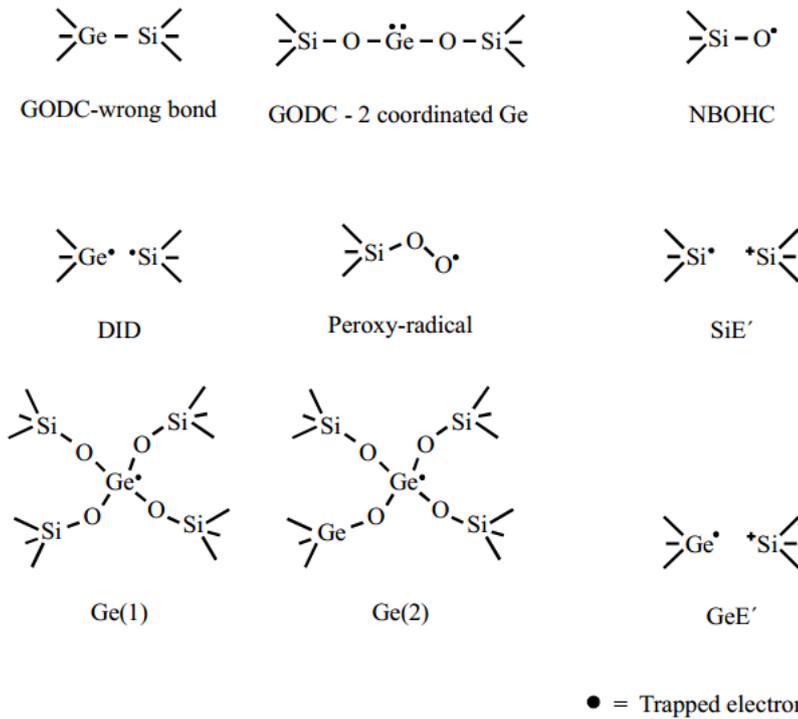
Figure 1.4.1: Different types of defects which are related to the photosensitivity in optical glass fibers [29].

Those wrong bonds seem to be the most important bonds for the increase of the photosensitivity in the UV range due to breakage of the bonds during UV exposure resulting in reduced absorption bands (also known as *bleaching*) [45]. For FBG inscription, the absorption peak of about 240 nm (assigned to GeO, [46]) is commonly used although there are more efficient absorption peaks as for example at 185 nm (assigned to GeO_2, [46]) as depicted in figure 1.4.2.
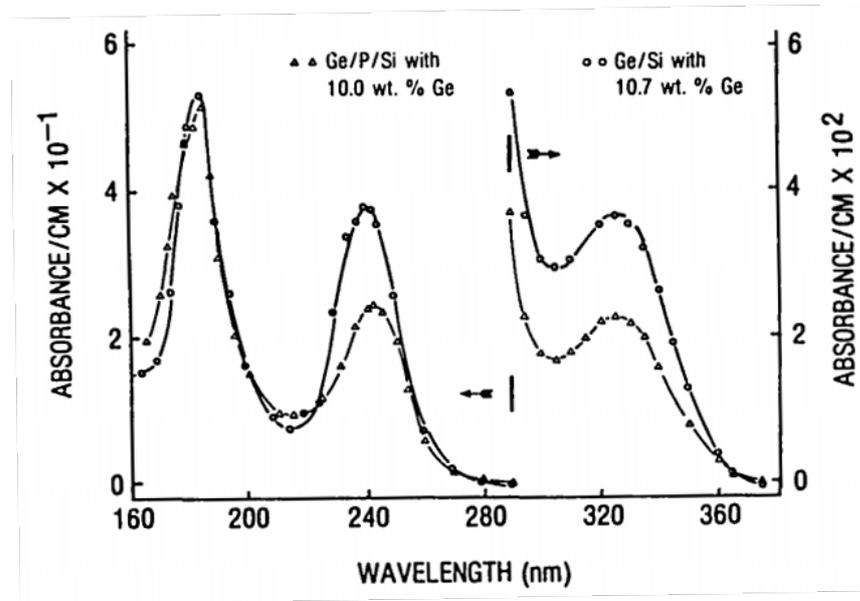
Figure 1.4.2: Different UV absorption bands in germania doped silica ($10.7\,wt.\%$ Ge, circles) and germanium phosphosilicate ($10\,wt.\%$ Ge, triangles) [46].

However, during UV exposure, the "wrong bonds" break while releasing an electron and leaving a so called GeE′ defect[3] (Ge atom with one unpaired electron bonded to three oxygen atoms, see figure 1.4.1). As previous experiments have shown, GeE′ defects seem to be the biggest factor in the increase of the refractive index during the UV inscription of fiber Bragg gratings [48] as they correlate directly to the refractive index change, as depicted in figure 1.4.3.
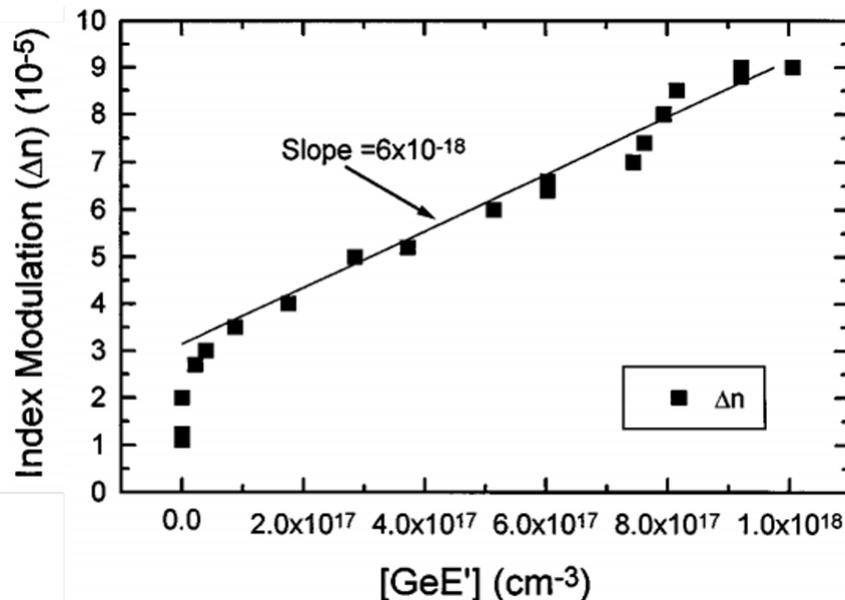
Figure 1.4.3: Correlation between the amount of GeE′ centers and the change of the RI during UV inscription (Laser fluence of $300\,\mathrm{J/cm^2}$) [48].

---

[3]See Bridges et al. [47] for defect nomenclature in silica

The UV induced reaction of the wrong bonds during the UV exposure is given by equation 1.9:

$$Ge - Ge \xrightarrow{h\nu} GeE' + GeO_3^+ + e \qquad (1.9a)$$

$$Ge - Si \xrightarrow{h\nu} GeE' + SiO_3^+ + e \qquad (1.9b)$$
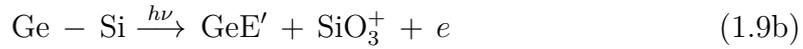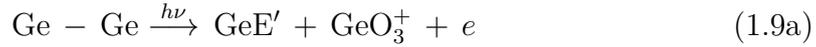
The UV released electron moves within the conduction band of the glass where it might be trapped in color centres. Furthermore, the electron could move to an oxygen atom where the $Ge - O$ bond is destroyed by capturing the free electron leaving a negative oxygen ion (non bridging oxygen hole center, NBOHC, see figure 1.4.1) together with another GeE' ($\equiv Ge^{\bullet}$) defect:

$$\equiv Ge^- - O - Si \longrightarrow \equiv Ge^{\bullet} + {}^-O - Si \equiv \qquad (1.10)$$
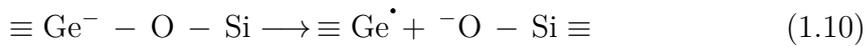
In addition, during the fiber drawing process the "wrong bonds" can be ruptured by tensile strain resulting in $Ge^{\bullet\bullet}Si$ and $Ge^{\bullet\bullet}Ge$ radicals, which are also known as "drawing-induced defects" (DID, see figure 1.4.1) [49]. The amount of DID increases with increasing drawing speed during the fiber drawing process which creates additional tension [50].

Hydrogen loading

Another way of increasing a fiber's photosensitivity is by loading the fiber with hydrogen under high pressure before UV exposure. During the UV exposure, different hydroxyl (OH) groups, namely $Si - OH$ and $Ge - OH$, are formed within the fiber core (see equation 1.11) which are known to be temperature stable up to 1200°C [51, 52]. These OH groups increase the refractive index [11]. For the reaction of the glass network with the hydrogen molecules, different reactions were proposed [53, 54]. During the UV exposure of hydrogen loaded fibers, the following two step reaction of the glass network with the hydrogen was proposed [53]:

$$\equiv GeOT \equiv \xrightarrow{h\nu} \equiv Ge \cdots OT \equiv \qquad (1.11a)$$

$$\equiv Ge \cdots OT \equiv + H_2 \longrightarrow \equiv Ge^{\bullet} + HOT \equiv + H^{\bullet} \qquad (1.11b)$$
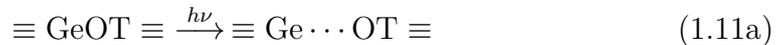
Here, the T stands for either a Ge or Si atom. During the UV exposure, Ge is excited into a higher energy state which is presented as "$\cdots$". Without the presence of hydrogen, the excited germanium would go back in its ground state after a short period of time [52]. But in the presence of hydrogen, the excited state can now react with the hydrogen to form a GeE' (Tsai et al. stated that GeE' generation is more efficient with hydrogen [48]) defect, an OH group and atomic hydrogen. This atomic hydrogen can now either break GeO bonds, which are known to be weaker

than SiO bonds [45], to form more GeE′ defects or react with GeE′ defects to form hydrates (H-bearings) as GeH which can increase the RI, too [48]. Additionally, the hydrogen can also break the Si-O-Si bond forming hydroxyl and hydrides as proposed by Shelby [55]:

$$Si - O - Si + H_2 \longrightarrow SiOH + SiH \tag{1.12}$$
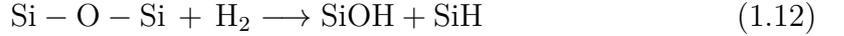
In 1994, Greene et al. performed measurements on hydrogen loaded fibers in order to investigate the effect of low intensity UV exposure ($\approx 1\text{mW/cm}^2$) [56]. In conclusion, they proposed two new hydrogen related reactions as follows

$$\equiv Ge - O - Si \equiv + H_2 \longrightarrow \equiv GeH + HOSi \equiv \tag{1.13}$$

and

$$= Ge{\cdot}{\cdot}^{(2+)} + H_2 \longrightarrow = GeH_2 \tag{1.14}$$
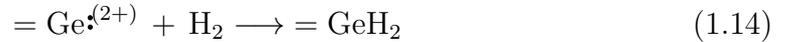
where $= Ge{\cdot}{\cdot}^{(2+)}$ describes a plus two oxidization state of dioxygen germanium (including a non-bonding lone pair of electrons).

Loading glass with hydrogen and subsequent exposure to UV does not only lead to photochemical reactions but also to mechanical changes like densification [9,52,57], volume expansion [58] and relaxation of stress along the fiber [59].

1.5 Scope of thesis

The annealing behavior of the refractive index structure of type-I FBGs and RFBGs raise questions regarding their properties; and subsequent performance of RFBG-based sensors. This project focuses on understanding the FBG regeneration process and improving gratings for temperature measurements in harsh environments beyond 1000 °C for various grounds. This involves testing of fiber sensors and their characterization as outlined below.

(i) Macroscopic study

The parametric studies are performed to characterize the FBGs from different patterns after different post-patterning treatments. This study involves optical reflectivity measurements and testing in the dedicated optical set-up that allows us to cycle temperatures beyond 1000 °C. This is conducted through collaboration with our industrial partner at their laboratories. Based on this study, a phenomenological model was derived that illustrates the dominating process responsible for both the FBGs disappearance and regeneration.

The operation of FBG sensors also required the optimization of the regeneration process for high temperature application. The investigation of the degradation process associated to glass fiber-class helped identify the threshold-like temperature ($\approx 300\,°C$) after the heat treatment of the glass between room temperature and $1000\,°C$. As a result, RFBG produced at $700\,°C$ following the long-term stability test at $1000\,°C$ yielded high Bragg reflectivity, exceeding the state of the art by approx. $400\,\%$. This enabled the development of high temperature fiber optic sensor and met our industrial counterpart's need.

(ii) Microscopic study using Raman and luminescence spectroscopy

To gain a microscopic understanding and enhancement of the general techniques, Raman/PL instrumentation is implemented to investigate the Raman scattered signal of fiber cores monitored between room temperature and $1000\,°C$. This non-destructive analysis technique is used for several fiber types:

- Hydrogen loaded as well as unloaded fibers both,

- UV exposed fibers with and without hydrogen loading for UV exposed in similar FBG writing conditions,

- Fibers containing different germanium concentration and

- Grating written fibers with hydrogen loading.

This part of the project studied with the installation of a complementary setup from an existing optical spectrometer to monitor Raman signatures of single- and multi-mode glass fibres as a function of temperature. This included the complete optical design of a micromanipulator-based free space to fibre-coupling unit, the choice of the appropriate furnace and the focussing unit of a microscopy scanner into the Raman spectrometer. This setup utilised the entire length of the glass fibre, a larger portion of which stays in the furnace that substantially enhances the signal to noise ratio as compared to side-view experiments. This approach relies on spectroscopy ALONG the fiber core and takes advantage of long interaction lengths compared to conventional microscopy approaches that instantaneously rewarded with an unexpected visually perceivable red luminescence at the location of a Fiber Bragg grating, as well as allowing the chemical and structural analysis of fibers at various stages of thermal processing.

2 Fiber Bragg Grating

2.1 Fiber Bragg grating parameters

The operation of FBGs for temperature sensing is based on the detection of the Bragg wavelength shift induced by temperature changes. The reflected optical signal in FBGs determines its strength at a certain wavelength relative to the local noise floor that primarily depends on the sensitivity of the detector.
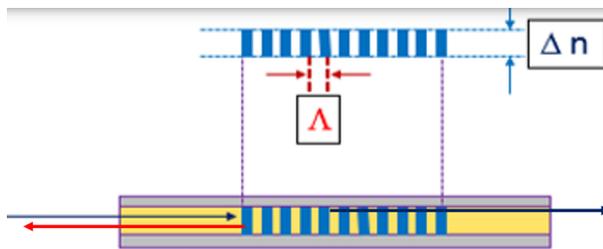
Figure 2.1.1: Illustration of a fiber Bragg grating. An incoming lightsource (e.g. the interrogator laser) will be reflected around the Bragg wavelength while every other wavelength is transmitted.

The periodic perturbations of refractive index are produced by exposing the fiber core to the UV-light through a special transmission diffraction grating referred as a phase mask. The phase mask generated interference and diffraction (± 1 orders) properties of UV-optical field results in a modulated structure that are photo-imprinted along the optical fiber length.
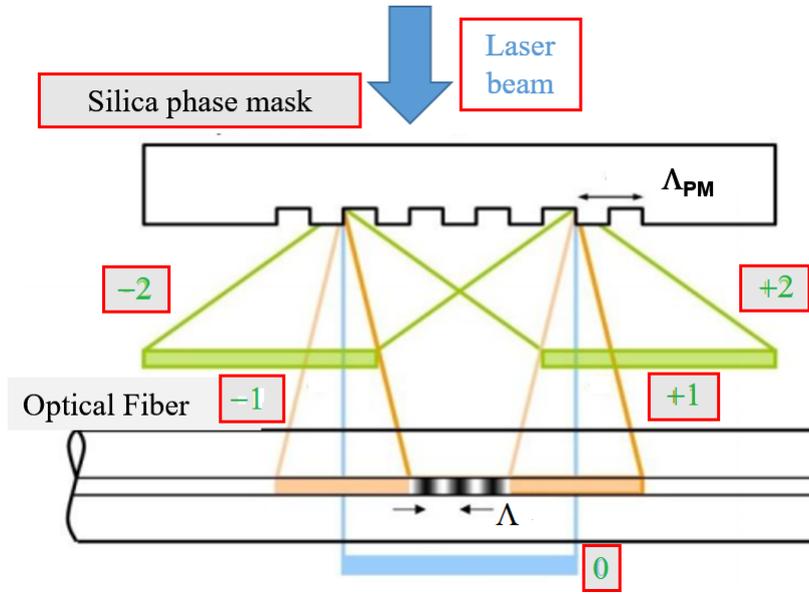
Figure 2.1.2: Schematic of a phase mask approach. The numbers within the red box in the figure represent the diffraction orders. The symbols Λ and Λ_{PM} are the period of the grating and that of the silica phase mask, respectively. Figure is adapted from the reference [60].

The detection of the reflected signal in FBGs can be described by the following parameters:

(i) Center wavelength (λ_B)

The center wavelength is calculated from the maximum reflection region of the spectrum by taking the weighted average of the wavelength weighted by the signal intensity or power over the points exceeding the threshold. This is known as the Bragg wavelength (λ_B).

The temperature dependence of λ_B, for a given periodicity of the grating (Λ) and the effective refractive index (n_{eff}) of the fiber core, is expressed by:

$$\lambda_{\text{B}}(T) = 2n_{\text{eff}}(T) \cdot \Lambda(T) \qquad . \tag{2.1}$$

The period (Λ) of the grating is given by

$$\Lambda = \frac{\Lambda_{\text{PM}}}{2} \tag{2.2}$$

where Λ_{PM} is the period of the phase mask which is used during inscription.

The effective refractive index and the grating period change with temperature (T) and with strain (ε), thus the change of the wavelength can be derived from equation

2.1 and described as follows:

$$\Delta\lambda_{\mathrm{B}} = 2\left(\Lambda\frac{\partial n_{\mathrm{eff}}}{\partial\varepsilon} + n_{\mathrm{eff}}\frac{\partial\Lambda}{\partial\varepsilon}\right)\cdot\Delta\varepsilon + 2\left(\Lambda\frac{\partial n_{\mathrm{eff}}}{\partial T} + n_{\mathrm{eff}}\frac{\partial\Lambda}{\partial T}\right)\cdot\Delta T \qquad . \tag{2.3}$$

If the FBG is only used for temperature sensing (thus $\varepsilon = 0$), equation 2.3 simplifies to

$$\Delta\lambda_{\mathrm{B}} = 2\left(\Lambda\frac{\partial n_{\mathrm{eff}}}{\partial T} + n_{\mathrm{eff}}\frac{\partial\Lambda}{\partial T}\right)\cdot\Delta T \qquad , \tag{2.4}$$

therefore, the shift in λ_B upon temperature change obeys:

$$\Delta\lambda_{\mathrm{B}} = \lambda_{\mathrm{B}}\left(\xi + \alpha\right)\Delta T \qquad . \tag{2.5}$$

Here, "ξ" is the core's thermo-optical coefficient[1] [61] and "α" is the core's coefficient of thermal expansion (CTE)[2] [62] terms that are temperature-dependent. The wavelength shift observed for FBG is dominated by the thermo-optic coefficient over thermal expansion, so that typically 90% of the shift is attributed to changes of the refractive index of the fiber core. Thus, the total Bragg wavelength shift being measured using the equation 2.5 simplifies to

$$\Delta T = \frac{\Delta\lambda_{\mathrm{B}}}{\lambda_{\mathrm{B}}\left(\xi + \alpha\right)} \tag{2.6}$$

that can be used to obtain the total temperature change of the FBG senor.

(ii) Peak intensity or reflectivity(R):
The change in peak height (or intensity) of the reflected signal called the reflectivity (R) has a strongly non-linear dependence on the grating parameters expressed by:

$$R = \tanh^2\cdot\left(\frac{N\eta\Delta n_{\mathrm{mod}}}{n_{\mathrm{eff}}}\right) \tag{2.7}$$

where N is the number of grating planes ($\sim$ twenty thousand in our case), η is the fraction of power guided in the fiber core, and Δn_{mod} is the amplitude of the refractive index modulation.

(iii) Peak width (**γ**):
The peak width is calculated using the wavelengths difference of left and right of the maximum reflection region of the spectrum and is defined as:

$$\gamma = \frac{2\eta\Delta n_{\mathrm{mod}}}{\pi}\cdot\lambda_B \tag{2.8}$$

---

[1] $\xi = \frac{1}{n_{\mathrm{eff}}}\frac{\partial n_{\mathrm{eff}}}{\partial T} \approx 8.6\cdot10^{-6}\,\frac{1}{\mathrm{K}}$
[2] $\alpha = \frac{1}{\Lambda}\frac{\partial\Lambda}{\partial T} \approx 0.6\cdot10^{-6}\,\frac{1}{\mathrm{K}}$

2.2 Grating types

2.2.1 Type-I grating

Type I FBG, as illustrated in figure 2.1.1, is characterized by a periodic modulation of a fibers core smooth refractive index change upon exposure to laser intensity below ionization threshold of the glass, which was first observed in 1978 by Hill et al. [63]. They can be used as dielectric mirrors in fiber lasers, selective wavelength filters and in sensor applications. The modulation of the refractive index might be realized by UV exposure with an exciplex laser (e.g. KrF $\approx$ 248 nm, see 3.2) and a phase mask (Period $\Lambda_{PM} \approx$ 1060nm) [3]. Using an excitation wavelength of around 240 nm breaks the "wrong bonds". Additionally, it has been shown that grating inscription in pure silica core fibers is possible with an excitation wavelength of 193 nm [64].

Temperature Behavior of Type I Fiber Bragg Gratings

Type I gratings are not stable at high temperatures and start to decay when exposed to temperatures above approx. 300 °C. Tsai et al. [48] showed that the thermal stability of the GeE$'$ defects centers, which are mainly responsible for the index modulation, are temperature stable up to 300 °C, figure 2.2.1.
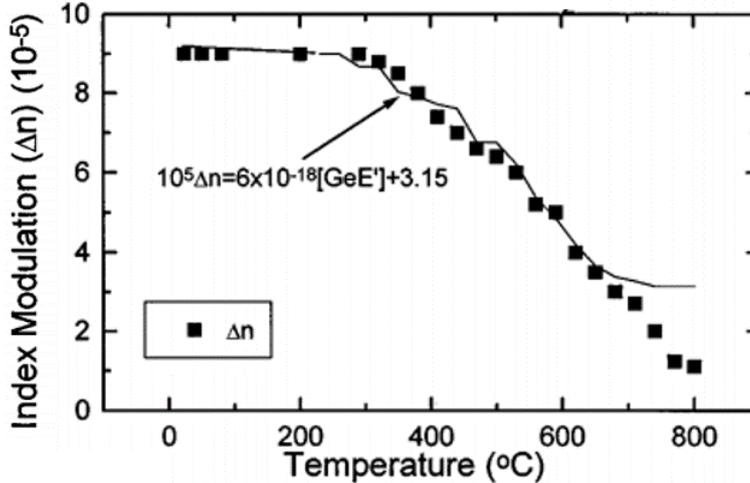
Figure 2.2.1: Thermal decay of the GeE$'$ defect (solid line) and index modulation (dots), respectively [48]. With increasing temperature, the GeE$'$ defects as well as the index modulation decreases.

When the temperature is higher than 300 °C, the amount of GeE$'$ defects and the index modulation decrease. The grating's meta stable behavior can be described with a decay theory, established in 1994 by Erdogan et al. [10] and evidenced by many researchers [65–68]. In the proposed model, Erdogan described that the elec-

trons released during UV excitation (see section 1.4) would be trapped in potential wells as depicted in figure 2.2.2. Those traps can be depopulated by a minimum energy called demarcation energy E_d.
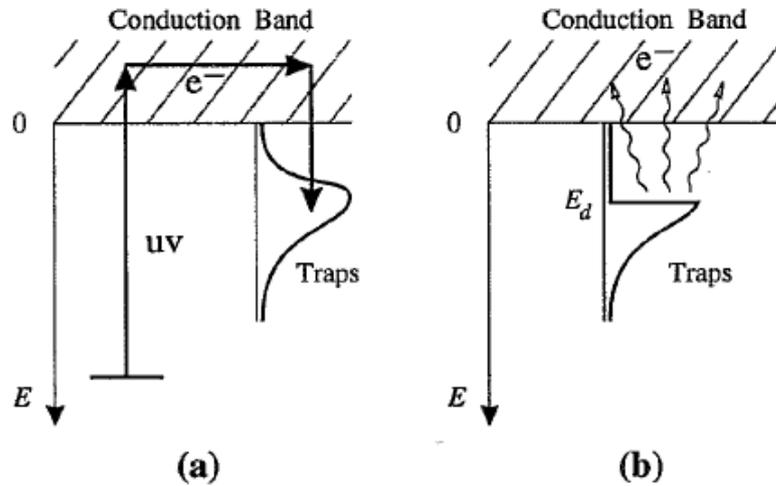
Figure 2.2.2: Illustration of the trapping (a) and depopulation (b) process of electrons. The traps can be emptied due to the demarcation energy E_d. Thermal depopulation is proposed for shallow traps ($E < E_D$) while deeper traps ($E > E_D$) remain populated [10].

After depopulation, the electrons of the traps do no longer contribute to the refractive index modulation of the grating, hence the reflectivity of the grating decreases. Figure 2.2.3 shows the experimental results of Erdogan [10] as well as the fitting line of the used power law model.
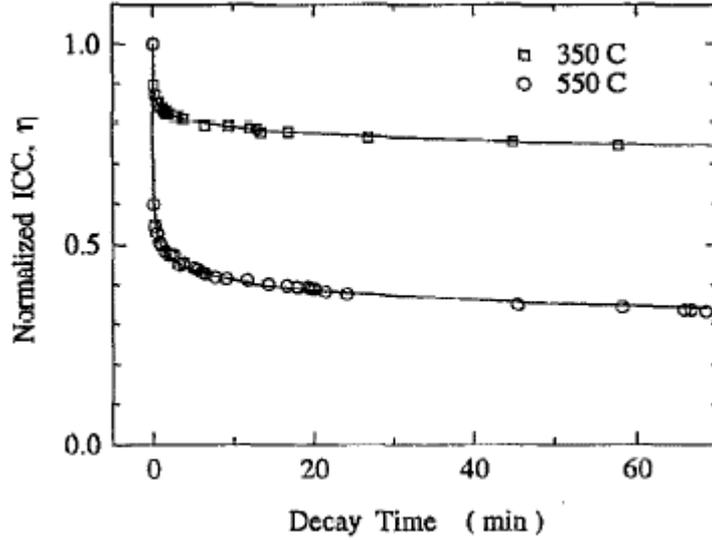
Figure 2.2.3: Experimental (circles and squares) decay experiment from Erdogan et al. at constant temperatures with applied power law model (solid line). Because of the power law model, the gratings show a stronger decay at the beginning and less decay after longer dwell time [10].

In his mathematical model, Erdogan used a power law model in which he described the thermal decay as a function of the trap depth. The thermal decay is defined as

$$\eta = \frac{1}{1 + A\left(\frac{t}{t_1}\right)^\alpha} \quad , \tag{2.9}$$

with A and α as dimensionless temperature dependent factors and $t_1 \equiv 1\,\text{min}$ is for the consistency of units. In a equation 2.9, η describes the normalized integrated coupling constant (ICC) η (however, different than the one previously used with same symbol, η in 2.7) which is a measurand for the strength of a grating and defined as

$$\eta = \tanh^{-1}\left(\sqrt{R_{\text{max}}}\right) \quad , \tag{2.10}$$

with R_{max} as the maximum reflected power of the grating.

2.2.2 Type-II grating

Type II damage gratings are formed by high fluence single-pulse UV exposure above-threshold ionization potential of the glass [69, 70]. The resulting gratings have good thermal stability, however reduced mechanical integrity at high-temperature and are of poor spectral quality. There is another different grating variant inscribed with ultrafast IR laser (fs and ps pulse durations) where very high peak power locally modifies the glass structure due to extremely short interaction times and produces refractive index changes resulting in more stable defect properties, different from

thermal decay of type II damage gratings.

2.2.3 Regenerated grating

Regenerated fiber Bragg gratings (RFBG) are typically produced from a type I grating in hydrogen loaded fiber after a subsequent exposure to high temperatures (above $\approx 300\,°C$ [28]). During a heat treatment at regeneration temperature, the type I seed grating decays as a usual type I grating till it is fully erased (below the noise level). Afterwards, a 'new' grating occurs but with moderate reflectivity. The process of regeneration is commonly achieved by hydrogen or deuterium loading of the fiber prior UV inscription [8, 28, 29]. Nevertheless, some reasearches have shown that the regeneration process might be achieved by loading the fiber with helium [71] or even with hydrogen loading after the inscription process [72]. The regeneration process of hydrogen loading standard SM fibers was observed in 2004 for the first time by Fokine [8], the results are depicted in figure 2.2.4.
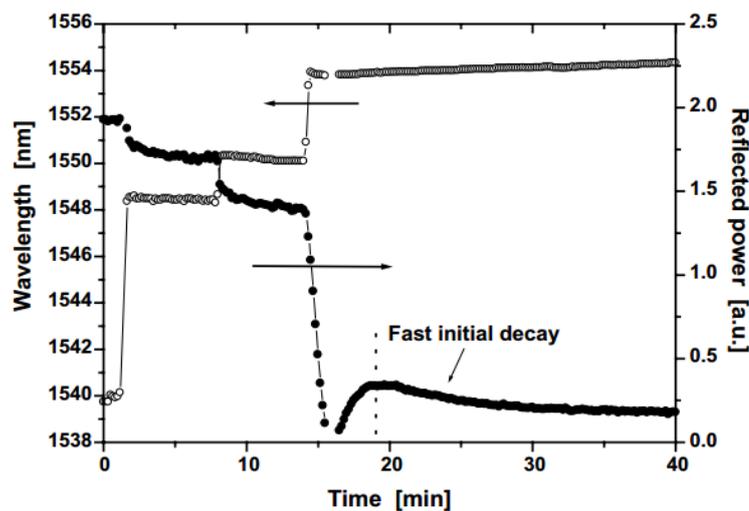
Figure 2.2.4: Regeneration behavior of a H_2-loaded SMF28 fiber observed by Fokine after heating from room temperature ($\lambda_B \approx 1540\,nm$) to 600°C ($\lambda_B \approx 1548\,nm$), 700°C ($\lambda_B \approx 1550\,nm$), and 1000°C ($\lambda_B \approx 1554\,nm$). The regeneration occurs after approx. 15 minutes where the reflected power is below the noise level and afterwards arises again to its maximum after 18 minutes [8].

Until now, there have been several attempts to explain the regeneration process (e.g., glass densification, chemical changes etc. [8, 9]), however the underlying microscopic mechanisms (chemical and/ or structural changes) of the regeneration process are not well understood yet. The regenerated gratings in glass do not show the optical losses yet can outperform type II damage gratings at ultra high temperature (e.g, engine, spacecraft, furnace, reactor and so on). Regeneration technology is

rapidly being commercialized by several start-ups and businesses across the world. Our company partner which is specialized in high performance glass fibers and smart materials successfully built and demonstrated such fiber optic sensing system for the transient re-entry temperature monitoring up to 1100 °C in aerospace vehicles [73]. However, the mechanical integrity and packaging of these sensors remain the key challenge as strength is often compromised under the influence of such high heating. Nonetheless, the latter can be addressed by appropriate packaging consideration as one of the approaches has showed compatibility with high temperature ceramic (eg., C-SiC) and metallic alloys producing an optimized level of sensor mechanical protection with good thermal conductivity [73, 74].

Theories for the Regeneration Process

Different models have been proposed regarding the grating regeneration mechanisms in hydrogen loaded fibers.

Chemical composition gratings (CCGs)/Seeded crystallization

The chemical composition gratings model, proposed by Fokine et al. [75, 76], describes the thermal stability of new grating structure formed through annealing of hydrogen loaded type I grating under the influence of intermediate temperature (600 to 700 °C) which leads to the out-diffusion of hydroxyl groups resulting in water molecules within the glass. On the other hand, the seeded crystallization model, proposed by Canning et al. [9, 77, 78], emphasizes the FBG regeneration mechanism to a region within the inner-cladding portion of the fiber. It was suggested upon thermodynamic assessment that exposing the seed grating to 900 °C facilitates nucleation along the core-cladding interface and crystallizes to crystobalite (stable phase of silica), thus the name seeded crystallization. However, such mechanism has been contradicted by Fokine [79] referring to the study of two gratings simultaneous regeneration by Canning et al. [77] with the argument that the temperature gradient along the grating and degradation dynamics following the annealing effect – the hot portion of the grating is most likely to decay faster and decrease in reflectivity before the cold region of the grating sees such effect during the regeneration process.

Trapped water molecules

This model suggests that the inscription in hydrogen loaded fibers generates periodic modulation of molecular water. Studies of Zhang et al. [30] and Dalle et al. [51] have attributed the thermally regenerated grating to trapped water molecules inside glass interstitials. However, it contradicts a water diffusion model in silica glass given by

Doremus [80].

$$Si - O - Si + H_2 \longrightarrow 2Si - OH \tag{2.11}$$

Poumellec et al. [81] showed a significant migration of hydroxyl groups, thus the migration of molecular water (equation 2.11) is also indicative of rather low stability of the UV-inscribed grating in H_2-loaded fibers at low to intermediate temperature in comparison to pristine fibers. This theory also relates to the effect of strain corrosion in glass fiber [32, 82, 83]

3 Materials and Methods

3.1 Fiber properties and types

Silica fibers consist of silica (SiO_2), pure silicon oxide, a refined type of sand or quartz that can be doped with a range of materials, for example the core region of most single-mode fibers incorporate germanium (Ge) resulting in a homogenous mixture referred to as germanosilicate glass. This changes its refractive index and also the absorption or emission properties. Glass exhibits a low attenuation across a wide wavelength region when the light wave is guided down a fiber, particularly in the C–Band of telecommunications window around 1530 nm to 1565 nm. Some important parameters of different types of fibers that were used in this study are presented in table 3.1.1.

Table 3.1.1: Parameters of the used fibers [15]

Fibertype	GF1B	SMF28	PS1250/1500	iXBlue
Manufacturer	Nufern	Siecor	Fibercore Ltd.	IXFiber
Coating Material	Acrylate	Acrylate	Acrylate	Acrylate
Cladding diameter (µm)	125	125	124.7	125.1
Core diameter (µm)	9	8.2	7 - 9	8.2
NA ($at\,1550\,nm$)	0.13	0.14	0.13	0.12
Effective RI ($at\,1550\,nm$)	1.448	1.468	-	-
Core dopant	Ge, P, F	Ge, B	Ge, B	Ge
Inner cladding	Yes	No	No	No
Inner cladding diameter (µm)	38	-	-	-
Mode field diameter ($at\,1550\,nm$)	10.4 ± 0.8	10.4 ± 0.8	9.6	-
Cutoff wavelength (nm)	1260 ± 100	≤ 1260	1209	1350
Hydrogen loading	2 days	26 days	No	120 hours
	80°C	23°C	No	RT
	110 bar	150 bar	No	140 bar

The symbol "-" inside the table denotes that the information is unavailable.

3.2 Seed gratings manufacturing

The fiber inscription is performed with a 248 nm KrF exciplex laser from Tui Laser (ExciStar S-200) and the phase mask technique as shown in figure 2.1.2. The grating length can be adjusted by the width of the aperture which is placed between the cylindrical lens and the phase mask. In this thesis, the width of the aperture is 12 mm. For inscription, the 50 cm long hydrogen-loaded fibers (see table 3.1.1 for the fiber properties) are mechanically uncoated in the midst of the fiber over a length of approx. 4 cm. The uncoated fiber is positioned in parallel to a phase mask at an effective spacing of about 100 µm. The focus lens is fixed 3 mm away from its focus position in order not to destroy the fiber by a high radiant fluency. By continuously moving the mirror, and with continuous laser exposure, the grating length of 12 mm is manufactured after one scan. The scan is necessary due to the small rectangular beam profile of the used exciplex laser (approx. 3 mm × 5 mm). The reflectivity peak of a Bragg grating is monitored during the inscription with an interrogation system (micron SM125), typically a band of saturated reflectivity at 1550 nm is achieved due to the long UV-exposure during each scan.

The used laser settings are shown in table 3.2.1.

Table 3.2.1: Grating inscription parameters.

Output power (mW)	525
Repetition rate (Hz)	100
Voltage (V)	1300
Phase mask Period (nm)	1070.73 ± 0.02
Fiber distance to phase mask (µm)	approx. 100
Cylindric lens position (mm)	8
Cylindric lens focus position (mm)	5

The diffraction patterns that arise from the corrugated structures or 1D binary surface-relief patterns of the phase mask are substantially replicated into submicron-scale periodic index variation in the core of a fiber, which result in an FBG. Alternatively, frequency components of the diffraction pattern are inversely proportional to dimensions on the mask. Information about the pitch is contained in the position of the diffracted orders, and the amplitude of the orders determines the duty cycle (i.e. $\frac{width}{pitch}$). The cylindrical lens produces patterns, at the focal plane, that are equal to the Fourier transform of the portion of the diffraction orders, generated by mask, initially passing through the aperture. The rectangular aperture expands the laser beam, defines the range of the diffracted angles and thus the maximum spatial fre-

quency (the ratio of *NA* and wavelength, λ). The zeroth transmitted order, which ordinarily goes straight through in a diffraction configuration of the mask (that is precision etched) such that each of the plus first and minus first orders of diffracted plane waves interfering to each other modulates in a sinusoidal envelope with period ($\approx 0.5\,\mu m$) equal to half the phase mask's period (equation 2.2). Considering a fiber core index of refraction of about 1.5, typically the reflectivity peak occurs at Bragg condition (see equation 2.1) for a wavelength equal to $2 \times 1.5 \times 0.5\,\mu m$ i.e. around $1.5\,\mu m$ which is in the telecom band. The higher diffraction orders typically do not make it to Bragg index modulation as they get eliminated by additional optics.

3.3 Launching light into a single mode fiber

Free-space fiber coupling

Coupling of a strong signal into fiber is the first step and rightly the most important task to fiber material diagnostic. The small core size of fiber results in increased sensitivity to free space coupling and as a result the alignment of the single-mode fiber is more complicated compared to multimode fibers. By using a stable optomechanical setup containing a focusing lens, one can achieve a long-term, stable, efficient launch of a free-space laser beam into a single-mode fiber with sufficient signal efficiency for coupling into the spectrometer to perform temperature dependent Raman scattering.

This requires the certain procedures to follow in order to couple a free space beam into a fiber precisely, and stably fixed without excessive thermally induced drifts:

- Adjustment knobs on the mirror: Adjustment knobs on the mirror are used to focus free-space beam at a point through lens striking the endface of the fiber.

- Focusing lens: This is used to focus the incident laser beam from the source to a spot matching the core size of the fiber.

- x, y and z components of the fiber alignment: Fiber is precisely positioned at the focal plane of the lens using the three-axes adjustment knobs of the translational stage which is a fixed mount.

Controlling the beam focus and the tilt angle of the optical lens is critical to light coupling into a fiber from a laser source. To achieve maximum coupling efficiency, the focused laser beam and the fiber parameters should be matched.

(i) The focused laser spot diameter (ϕ) should be less than or equal to fiber mode field diameter (ω). Considering the laser beam full divergence angle (θ) and the focal length (f) of the lens, one obtains the following basic properties.

$$\Phi(\mu m) = f(mm) \times \theta(mrad) \leq \omega$$

(ii) The focused laser beam numerical aperture (NA_L) should not exceed the fiber numerical aperture (NA_F).

$$NA_L = \frac{\phi(mm)}{2f(mm)} \leq NA_F$$

For a collimated laser beam of wavelength (λ), laser beam diameter (Φ) and fiber mode field diameter (ω), one can determine the lens focal length (f) in order to efficiently couple light onto the core of fiber.

$$f = \Phi(\frac{\pi\omega}{4\lambda})$$

$$\phi = 1.22(\frac{\lambda}{NA})$$

For Raman scattering measurement, for example, we determined the focal length of lens (f) to couple $473\,\mathrm{nm}$ light ($\Phi = 700 \pm 50\,\mu m$) into a SM fiber ($\omega = 2.8\,\mu m$) as $3.25\,\mathrm{mm}$ and for an objective PLN $4\times$ OLYMPUS, $18.5\,\mathrm{mm}$ working distance, $0.1NA$, the spot diameter as $5.7\,\mu m$. Finally, our launch condition to couple light into an iHR320 spectrometer at the other fiber end is choosing an objective, of higher NA (0.25), which is vertically attached in a HORIBA microscope.

3.4 Raman spectroscopy

The interactions between material and photons do not only lead to absorption but also to scattering of light. The latter is distinguished between elastic (Rayleigh) and inelastic (Raman) scattering. The energy difference of photon between the excitation and scattering is characteristic of material and or structure in the sample (e.g. type of the bond). As such the composition and behavior of the structure as a function of environmental changes are possible to monitor. Figure 3.4.1 shows the Jablonski diagram for the different scattering processes.
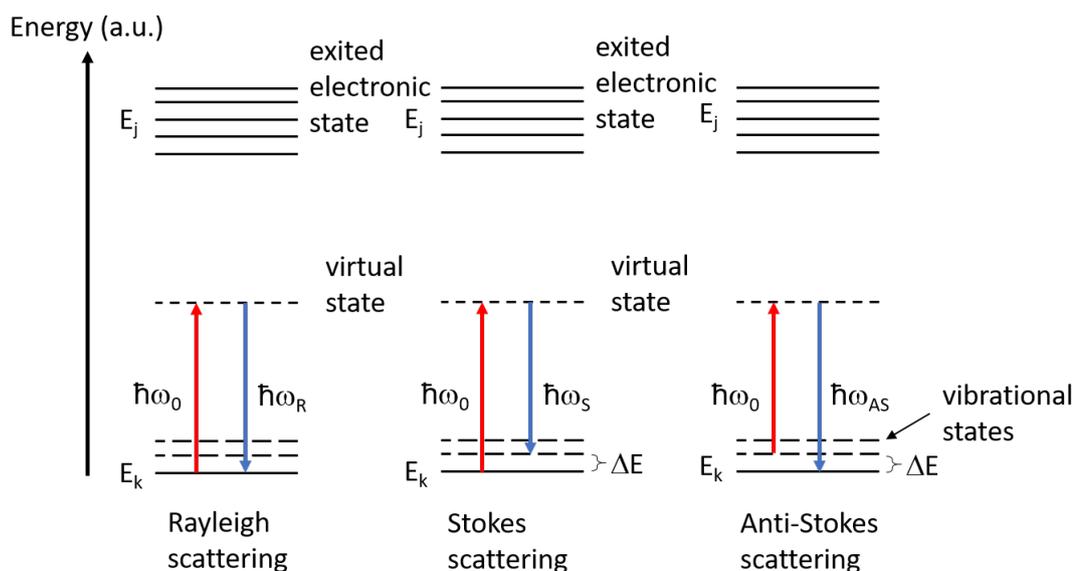
Figure 3.4.1: Different types of scattering. Elastic scattering ($\Delta E = 0$) is the most common process. The inelastic scattering is less likely than Rayleigh due to the dependence on vibrational states (factor $\approx 10^8$ [84]).

The physical basis for the Raman scattering is the vibrational modulation of the electronic polarizability in a molecule, e.g, if the EM wave interacts with a molecule, the molecule is excited to a higher vibrational or rotational virtual energy state by inducing an oscillating polarization. If the induced polarization is not coupled to the existing one (e.g. vibrational or rotational), the vibrational state of the molecule will stay unchanged resulting in Rayleigh scattering. Contrary, if the induced polarization couples with the existing polarizations the resulting energy will be higher than before resulting in an energy difference after reemittance [85]. The difference in energy is required for the vibrational excitation and thus characteristic for each molecule or bond. However, the energy difference ΔE of a material depends on the molecular vibration (molecule's mass), the structure (bonding angles, geometry) and surrounding (e.g. temperature or neighbouring atoms). By considering a molecule with N atoms there are different possibilities for spatial movement: $3N$ degrees of motional freedom (spatial), 3 rotational (spatial) and $3N$-6 of vibrational movements [86]. Figure 3.4.2 shows different modes for a triatomic molecule (e.g. silica). Here, the motion A (symmetric bending), D (symmetric stretching) and F (symmetric bending) are Raman active.

symmetric stretch   asymmetric stretch   bend
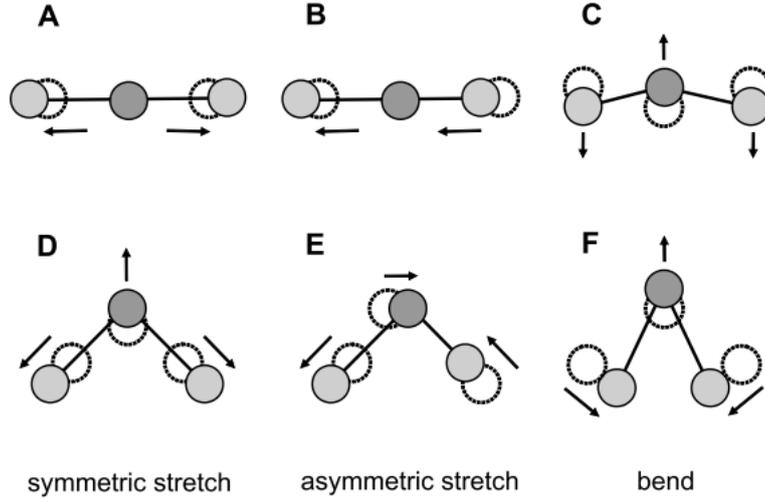
Figure 3.4.2: Different bending modes of linear (**A-C**) and nonlinear (**D-F**) molecules. The arrows represent the direction of movement and the dashed circles the initial positions. In addition, the linear molecules have one more vibrational mode in the perpendicular plane [86]. Raman active bending modes: A, D , F; IR vice versa.

By considering the wave behavior of light, the scattering of light depends on the polarizability of the molecules which is given by equation 3.1

$$\mathbf{P} = \alpha \cdot \mathbf{E} \qquad , \tag{3.1}$$

with **P** as the polarization of the molecule, α as the polarizability tensor[1] and **E** as the electric field vector of the incident wave. However, the polarizability consists of an initial polarizability α_0 and optical phonon induced change α_{ind} [87]. Hence, equation 3.1 changes to

$$P = (\alpha_0 + \alpha_{ind} \cdot \cos(\omega_{vib} \cdot t)) \cdot E_0 \cdot \cos(\omega_0 \cdot t) \qquad . \tag{3.2}$$

Here, ω_{vib} is the vibrational frequency of the excited molecule, E_0 the field amplitude of the electric field and ω_0 the frequency of the incident light wave. By using the following trigonometric function

$$\cos(A)\cos(B) = \frac{1}{2}\left[\cos(A+B) + \cos(A-B)\right] \tag{3.3}$$

equation 3.2 follows to

$$P = \alpha_0 E_0 \cos(\omega_0 \cdot t) + \frac{1}{2}\alpha_{ind} E_0 \left[\cos((\omega_0 + \omega_{vib})t) + \cos((\omega_0 - \omega_{vib})t)\right] \qquad . \tag{3.4}$$

Here, the first term describes the Rayleigh scattering while the difference and sum

---

[1]Only linear materials will be considered

terms describe the Raman effect. The effiency of the Raman effect depends strongly on the used excitation wavelength as follows [84]

$$I \sim \sigma_R \sim \omega^4 \qquad , \tag{3.5}$$

with I as the scattered intensity, σ_R as the Raman scattering cross-section and ω as the frequency of the excitation light.

In Raman spectroscopy, only the relative shift of the peaks compared to the excitaion wavelenght is considered. The calculation of the peakshift follows

$$\Delta\nu = \frac{1}{\lambda_{\text{excitation}}} - \frac{1}{\lambda_{\text{scattered}}} \qquad , \tag{3.6}$$

where $\Delta\nu$ describes the Raman shift, $\lambda_{\text{excitation}}$ the excitation wavelength and $\lambda_{\text{scattered}}$ the scattered wavelength.
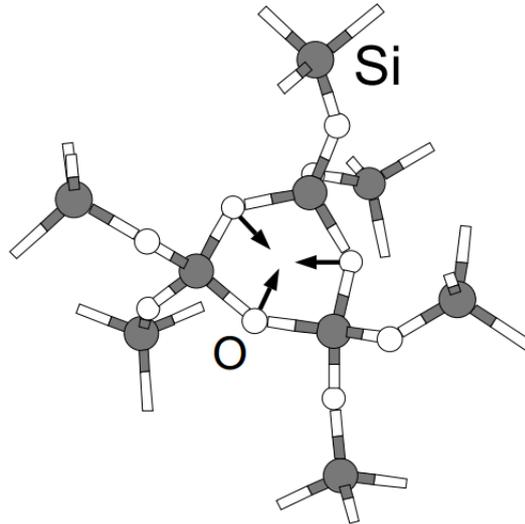
Figure 3.4.3: 3-fold ring in vitreous silica network. The black arrows illustrate the breathing motion of the 3-fold silica ring [88].

An edge filter is used which suppresses the anti-Stokes peak as well as the Rayleigh peak (which would exceed all other peaks). In the case of more complex materials, different vibrational modes like breathing modes are possible, too. Figure 3.4.3 shows the behavior of a breathing mode in amorphous silica (3-fold ring, D2 defect). Exploiting the Raman effect for spectroscopy allows to characterize a sample not only in terms of chemical but also for microscopic structural changes.
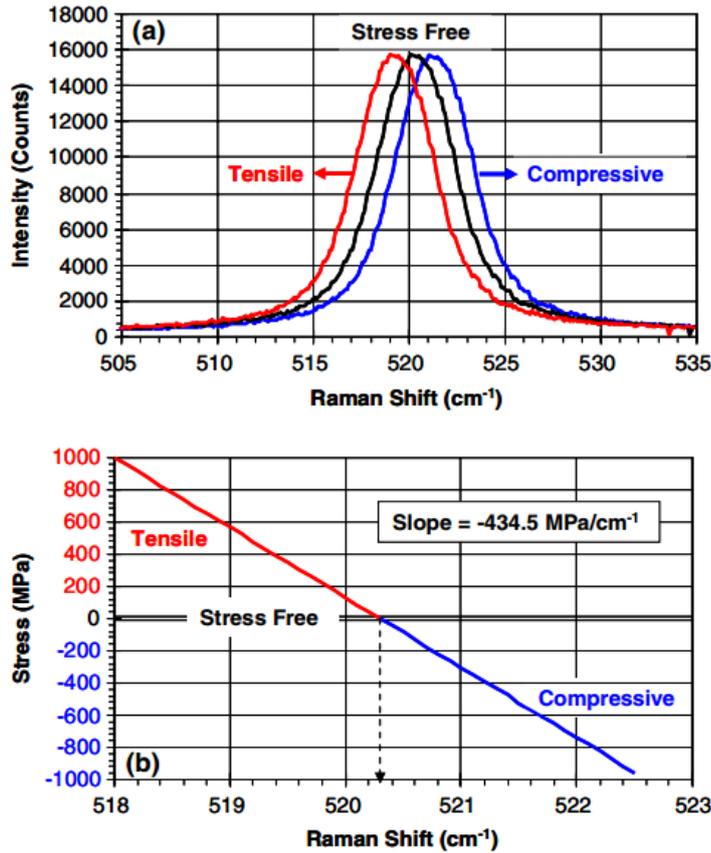
Figure 3.4.4: Stress measurements in a silicon sample. A shift in the Si-Si Raman peak position represents tensile (negative shift) or compressive (positive shift) stress [89].

The intensity of the Raman peaks is proportional to the amount of a specific compound. Thus, the Raman spectrum provides unique vibrational signatures of the underlying structure, for example the extended defect and strain. The full width at half maximum (FWHM) of a peak determines the state of crystallinity and plastic deformation of the material, respectively. A peak shift or exact wavenumber shift can be assigned to tensile and compressive stresses within the material, as shown in figure 3.4.4. This technique has also the potential to detect the crystal orientation of the sample by changing the polarization state of the excitation laser.

3.5 Photoluminescence spectroscopy

Shorter wavelengths do not only increase the Raman signal as described in section 3.4 but also increase luminescence in the sample [90]. Photoluminescence is generated when an electron is promoted to the upper state of a glass defect and subsequently recombines to a lower level, depending on the occupation density of the lower states, while emitting a photon.
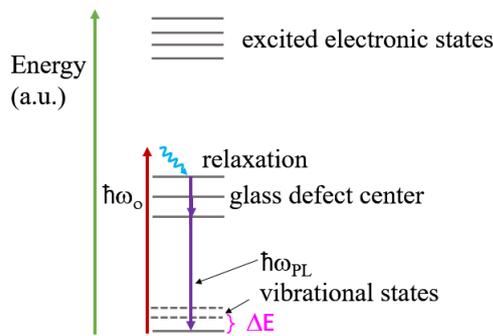
Figure 3.5.1: Jablonski diagram for photoluminescence in glasses. Since the energy of the exciation can be higher than the absorption of the glass defect, relaxation processes (Stokes shift) can occur.

Figure 3.5.1 shows the Jablonski diagramm for the photoluminescence. Here, a electron is promoted to the upper state of a glass defect if the excitation energy matches the bandgap (red arrow). After thermal relaxation, the electron recombines (blue arrows) to the lower energy levels of the glass defect. As such, being able to detect a decay of defect-related luminescence allows to monitor thermal activation energies, a reliable fingerprint of defects, encountered in the sample, for example in glass fibers and Bragg gratings.

3.6 Role of fiber dopants and hydrogen loading

Impact of dopants, UV and fiber drawing process

Investigating the influence of dopants on the characteristics of glasses is very important to tailor the properties of glasses to the needs of the applications. Hereby, germania (GeO_2) plays one of the most important roles since it is widely used for glass fibers in the telecommunication sector (e.g. standard telecommunication fiber SMF-28). The similar structure and properties of germania and silica make germania a perfect dopant [37]. In order to compare the differences between germania and silica (and mixed glasses), Raman spectroscopy is a very handy technique. Figure 3.6.1 shows typical Raman spectra for germania, silica and their binary glasses.
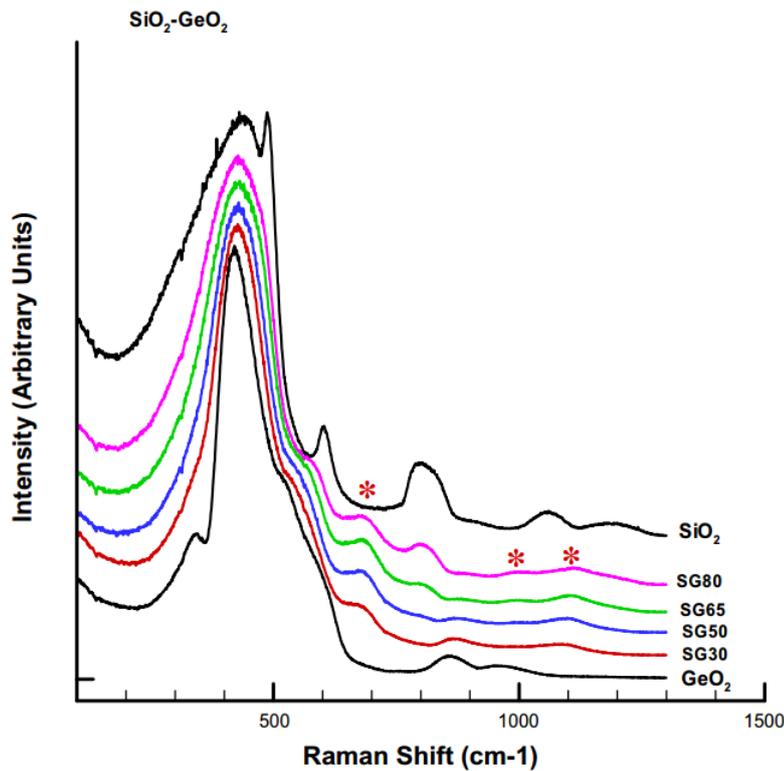
Figure 3.6.1: Raman spectra for silica, germania and mixed glasses. The numbers stand for the content of silica in percent and the red stars indicate the Ge-O-Si bonds which are not present in pure silica and germania, respectively [27].

The difference in the mass of germania compared to silica leads to a shift of the main peak (T-O-T symmetric stretching mode, T is either Ge or Si) to shorter wavenumbers due to the higher mass of the germania. Additionally, the D1 defect (4-membered rings) is not present in germania due to their instability [39] but a Ge 'deformation' motion related defect occurs around $350\,\mathrm{cm}^{-1}$ (Note that the graph starts at $100\,\mathrm{cm}^{-1}$) [37]. In a binary glass, additional mixed stretching modes (e.g. Ge-O-Si) are possible which are not present in the pure glasses (red stars in figure 3.6.1.

However, by doping the glass with dopants different than germania, the changes in the glasses are more complex. By adding fluorine to the glass, a new peak in the Raman spectrum appears around $945\,\mathrm{cm}^{-1}$ which belongs to the Si-F bond. This is shown in figure 3.6.3 for glasses with different fluorine concentrations.
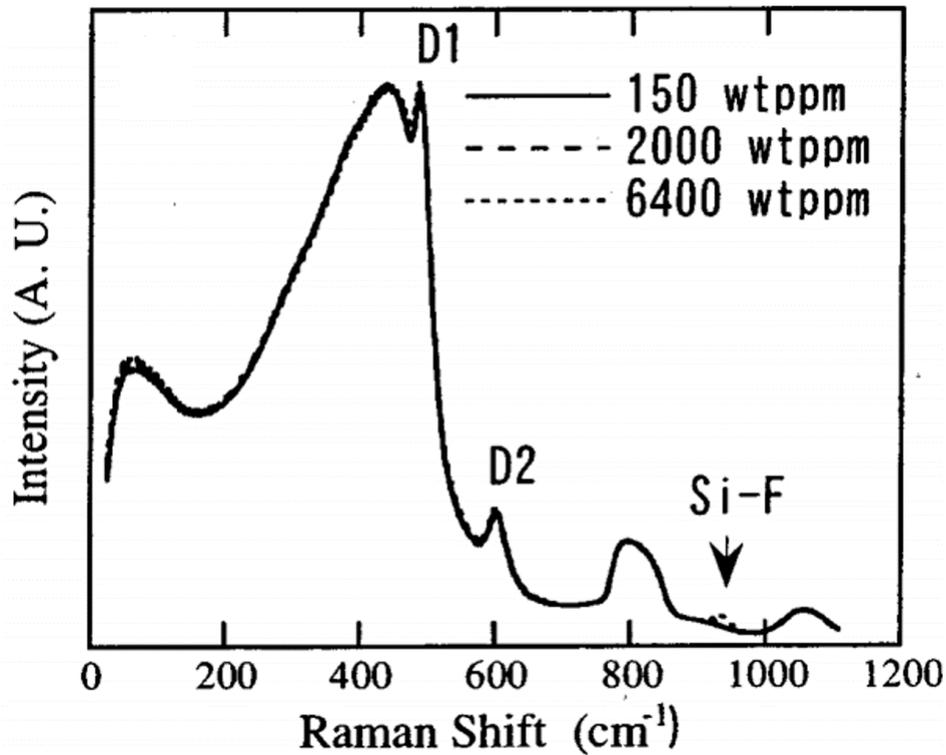
Figure 3.6.2: Raman spectra for fluorine doped glasses with different fluorine concentrations. The peak around $945 \, \text{cm}^{-1}$ is related to the Si-F bond [40].

The effect of fluorine doping has been investigated by Awazu et al. [91], Shimodaira et al. [40] and Saito et al. [34] leading to following results:

- Fluorine as a dopant increases the structural relaxation and thus glasses with lower fictive temperature can be made. The structural relaxation is mainly caused by Si-F bonds in the glass making the glass network less distorted. Due to the lower fictive temperature, the glass achieves better performance as low UV losses [34] or a bigger decrease of the RI [23].

- Fluorine substitutes OH groups resulting in less IR absorption and thus less attenuation [34]. Adding fluorine in fibers results in a higher mechanical strength since the Si-F bonds (instead of Si-OH) are more stable than Si-O bonds.

In addition, Awazu et al. correlated the intensity ratio of the $800 \, \text{cm}^{-1}$ peak (assigned to Si-O-Si symmetric bond stretching) which is insensitive to temperature/doping and the $945 \, \text{cm}^{-1}$ Si-F peak to the doping concentration, see figure 3.6.3 [91].
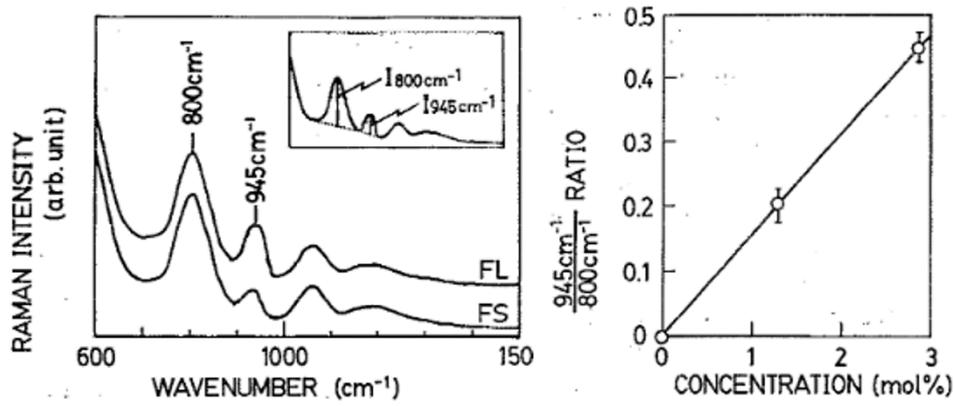
Figure 3.6.3: Left: Section of a Raman spectra for fluorine doped glasses with different fluorine concentrations (FL= $2.8 \, mole\%$ and FS= $1.3 \, mole\%$). The peak around $945 \, cm^{-1}$ is related to the Si-F bond. Right: Correlation of the intensity ratio to the doping concentration [91].

The dopant concentration of fluorine doped glasses can be easily evaluated by using the graph in figure 3.6.3, right. Additionally, dopants like boron or phosphorus can remove the D1 and D2 defects in glasses as it was shown by El Hamzaoui et al. [92]. Hereby, the dopant ruptures the structure of the 3- and 4-membered rings.

Nevertheless, not only doping of glasses leads to a different structure but also the exposure to UV light can alter the glass conditions. This behavior was investigated by several researchers who observed a densification process during UV exposure of glass [22, 52, 93, 94]. Vasil'ev et al. investigated the behavior of highly germania doped (18 mol%) optical fibers before and after UV (244 nm, second harmonic Ar ion laser, radiation dose approx. 7.5 kJ) irradiation using Raman spectroscopy [93]. Hereby, he observed densification of the fiber resulting in an increase of the D1 and D2 defects (4- and 3-membered rings) which are the densest ring structure in glass, see figure 3.6.4.
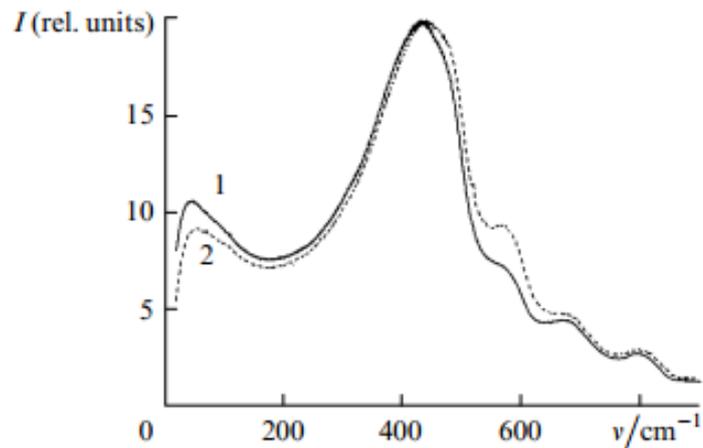
Figure 3.6.4: Densification of highly doped optical fibers after irradiation (2) with the second harmonic of an Ar ion laser. With increasing lasershots, the intensity of the D1 and D2 defects in the Raman spectrum increases [93].

Takahashi et al. investigated the densification of doped ($10\,mole\%$) and undoped silica disks after irradiation with a KrF laser ($248\,nm$, laser fluency of $600\,mJ/cm^2$) by Raman spectroscopy, see figure 3.6.5.
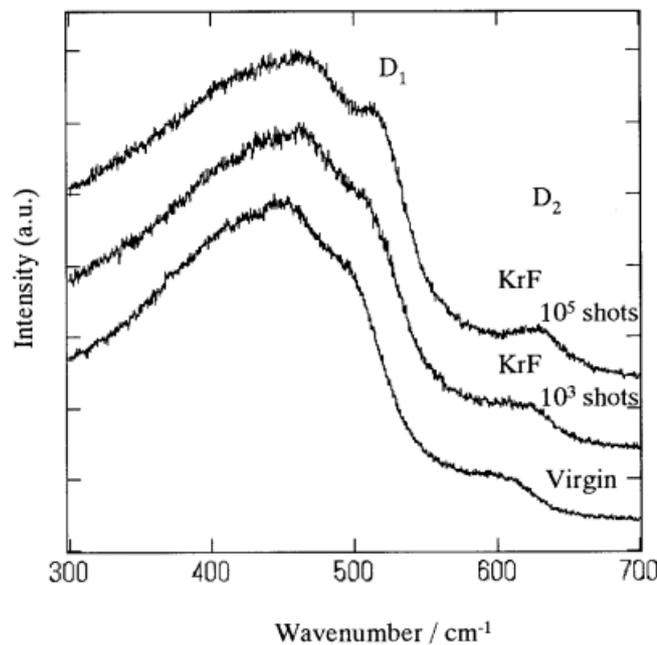
Figure 3.6.5: Densification of glass disks after irradiation with a KrF laser. With increasing lasershots, the intensity of the D1 and D2 defects in the Raman spectrum increases [94].

The results of Takahashi proved the densification in doped glasses but not in undoped glasses. Therefore, he concluded that the densification is related to the GeE′ defects in the glass, which are generated by UV exposure and thus not present in

pure silica. Hong et al. investigated the effect of UV induced densification in hydrogen loaded germania doped fibers (approx. $3\,wt\%$) using IR spectroscopy [52]. He used a frequency doubled Ar ion CW laser ($244\,nm$, $350\,mW$, irradiation times in figure 3.6.6, $30\,mm$ length of UV exposure) to inscribe long period gratings. The results of his work are shown in figure 3.6.6.
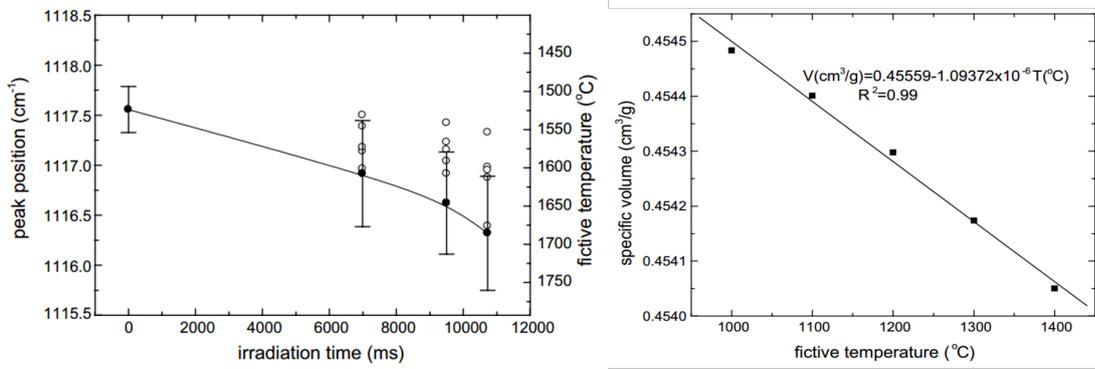
Figure 3.6.6: Left: Increase of the fictive temperature and shift of the IR peak with increasing laser pulses, respectively. Right: Correlation between the specific volume with fictive temperature [52].

Since the IR technique allows the correlation of wavenumber shift to the fictive temperature, the information about densification can be extracted as it increases upon increasing fictive temperature (i.e., decreasing specific volume). However, it is not clear if the densification was caused only by the UV exposure or by the inscription of the long period grating. Densifications caused by the inscription of FBGs have recently been shown [48].

Not only the dopants and UV exposure can lead to a densification of the glass but also the fiber drawing process. Hence, bulk material and fiber preforms may not have the same properties as a glass fiber due to different fictive temperatures. The influence of the fiber drawing process was investigated by Alessi et al. [22]. For this, he compared samples drawn under different conditions (mainly the fictive temperature) with Raman spectroscopy. Figure 3.6.7 shows the spectra taken before and after the fiber drawing process. The fiber spectrum differs from the fiber preform spectrum by an increase of the D2 and D1 peak and a decrease of the width of the $430\,cm^{-1}$ peak.
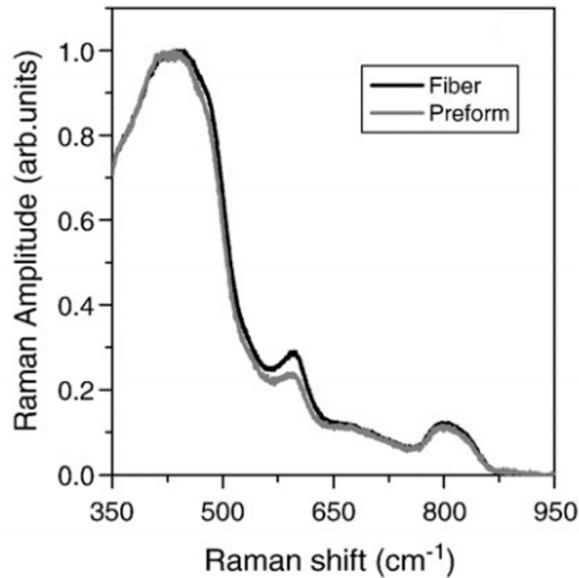
Figure 3.6.7: Raman spectra for a fiber preform (grey line) and the final fiber (black line). Densification can be seen by the increase of the D1 and D2 defect as well by a smaller main peak [22].

The influence of the fictive temperature was also shown by Shimodeira et al. who observed an increase of the D2 defects and a smaller main peak with increasing fictive temperature [40], see figure 3.6.8. To achieve different fictive temperatures, they annealed the glass to the desired fictive temperature in air with subsequent quenching in water. The fictive temperature was monitored by observing the IR peak at $2260 \, \mathrm{cm}^{-1}$ (similar to Hong et al, figure 3.6.6).
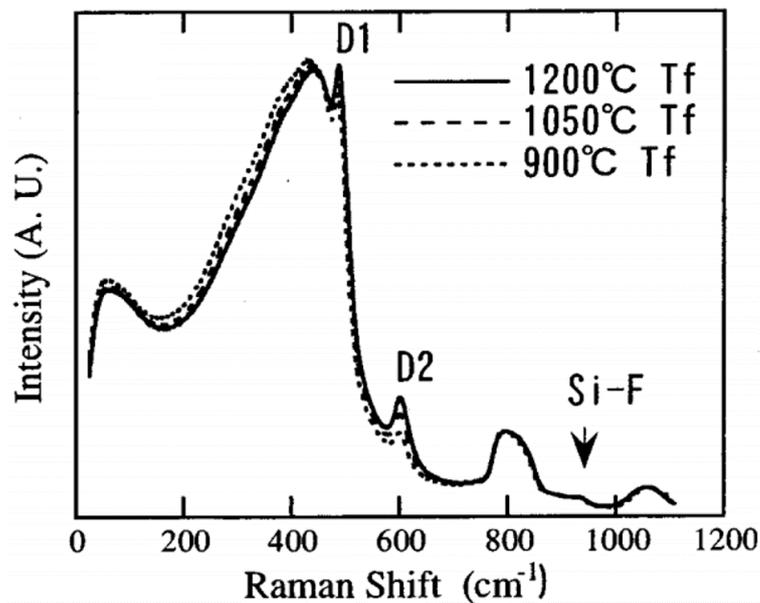
Figure 3.6.8: Raman spectra of fluorine doped glasses with increasing fictive temperature. Densification can be seen by the increase of the D1 and D2 defect as well by a smaller main peak [40].

Hydrogen influence on glasses

The glass properties can be influenced by hydrogen loading of the fibers. As already described in section 1.4, the presence of hydrogen in a fiber leads to a higher photosensitivity caused by the generation of hydrogen related components (also called H-bearings) and a higher generation efficiency of GeE$'$ defects.

Similar to Hong et al. [52], Greene et al. investigated the UV irradiation of hydrogen loaded fibers but with Raman spectroscopy instead of IR spectroscopy [56]. For this, they used hydrogen loaded fibers (40 cm long) with approx. 10 mol% germania which were exposed to UV light (approx. 3 cm length). For UV exposure a Hg calibration lamp (intensity approx. $1 \, \mathrm{mW/cm^2}$) was used. The results are shown in figure 3.6.9.
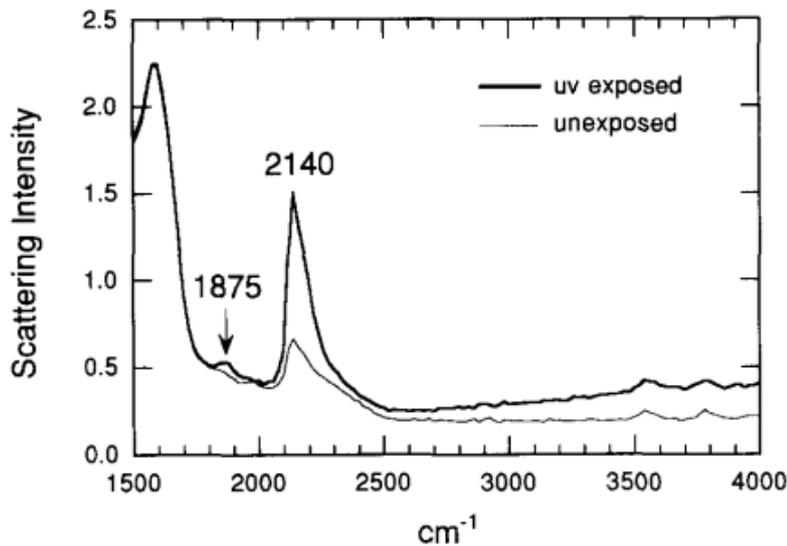
Figure 3.6.9: Raman spectra of a hydrogen loaded fiber before and after UV exposure (x-axis displays the Raman shift). After UV exposure, two new peaks are observable. The peak at $2140 \, \mathrm{cm^{-1}}$ is assigned to GeH$_2$ whereas the peak at $1875 \, \mathrm{cm^{-1}}$ is not yet assigned to any vibrational mode [56].

The peak at $2140 \, \mathrm{cm^{-1}}$ is assigned to the generation of GeH$_2$ which was barely present prior to UV exposure. However, the peak at $1875 \, \mathrm{cm^{-1}}$ was not assigned to any vibrational mode. In addition, Greene et al. noted that the UV exposure led to an increase of the fluorescence but did not discuss it (incrasing offset with higher wavenumbers in the graph).

Additionally, temperature effects on hydrogen loading were observed. Here, Greene et al. observed that hydrogen reactions in the fiber occur even if the sample was only annealing but not exposed to UV. The results of this annealing process (approx. 1000°C by igniting the fiber jacket) are shown in figure 3.6.10.
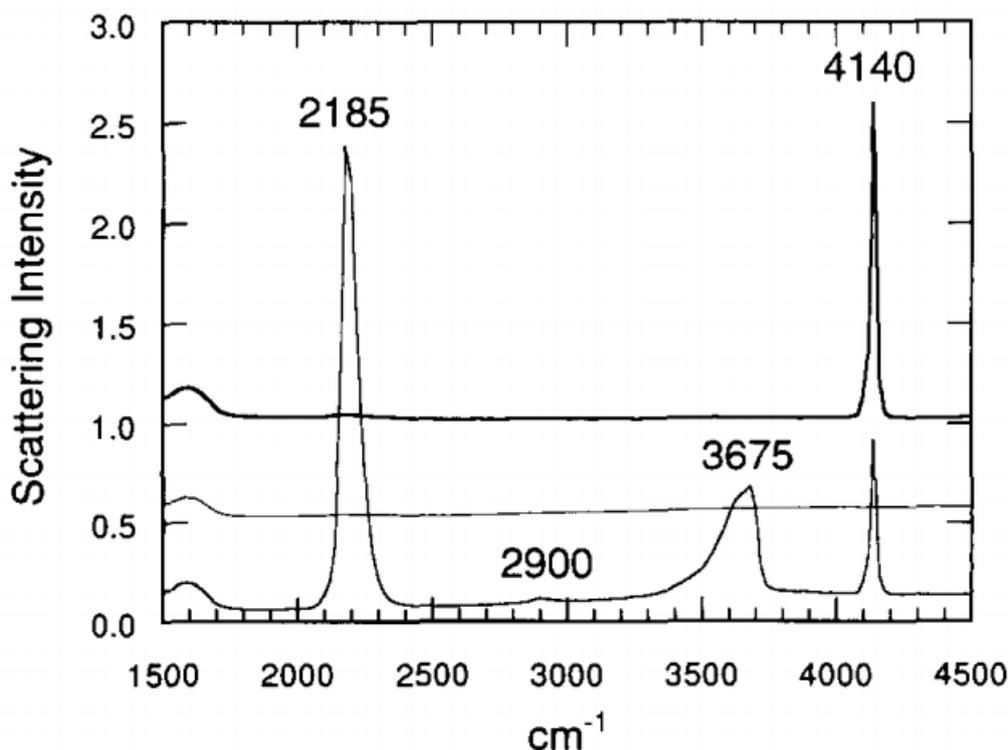
Figure 3.6.10: Influence of thermal threatment on hydrogen loaded fibers prior to UV
inscription. The upper spectrum shows the initial hydrogen loaded
fiber with a peak at $4140\,\mathrm{cm}^{-1}$ due to molecular hydrogen. The
middle spectrum is a reference curve without hydrogen and shows
no changes due to the annealing process. The bottom spectrum is
the hydrogen loaded fiber after annealing. Here, three new peaks
can be observed (with a decrease of the molecular hydrogen) which
are assigned to GeH ($2185\,\mathrm{cm}^{-1}$), unknown ($2900\,\mathrm{cm}^{-1}$) and Si-OH
($3675\,\mathrm{cm}^{-1}$) [56].

Due to the annealing process, new H-bearings are generated (two new peaks). The
peak at $2185\,\mathrm{cm}^{-1}$ is assigned to be the GeH vibrational mode while the peak at
$3675\,\mathrm{cm}^{-1}$ is assigent to the Si-OH mode ($4140\,\mathrm{cm}^{-1}$ is due to molecular hydrogen).
The $2900\,\mathrm{cm}^{-1}$ was not assigned to a specific compound and may be related to a
combination of two modes.

The effect of the fluorescence (as observed by Greene et al.) was discussed by Gouta-
land et al. [54]. In their experiments they used hydrogen loaded SMF-28 fibers from
Corning [95]. They heated their fibers (without prior UV exposure, similar to Greene
et al.) from room temperature (RT) to 200°C and 500°C. Hereby, they observed
that at RT only the hydrogen peak was apparent. With subsequent heating, a flu-
orescence at 650°C and 750°C, respectively, was observable. In their work, they
further suggested different chemical reactions that may occur and being responsible
for the fluorescence. Here, the most favored reason was fluorescence caused by GeH.
Dalle et al. investigated the influence of hydrogen loading in germanosilicate fiber

preforms (100μm−200μm thickness, 400 μm−5 mm core diameter, germania concentration 6.5−28 mol%) after UV exposure by FTIR spectroscopy [51]. Subsequent to the generation of H-bearings, they investigated the contribution of the H-bearings to the RI modulation and temperature behavior. For the UV exposure they used a dye laser ($\lambda = 244$nm, repitition rate $= 1$ - 50 Hz) which was pumped by a frequency doubled XeCl laser with a mean laser fluence of $30 \, \text{mJ/cm}^2$ and $140 \, \text{mJ/cm}^2$, respectively. The result of the UV exposure, depending on the quantity of pulses, is depicted in figure 3.6.11. For evaluation, they measured the intensity ratio and calculated the concentration ($\text{mol}^{-1}\text{cm}^{-1}$), and thus the induced absorption coefficient ($\text{ppm}^{-1}\text{cm}^{-1}$), from the molar extinction coefficient in the Beer-Lambert's law. However, especially the generation of molecular water, as depicted in figure 3.6.11, seems to be a very bold statement. Cordier et al. [96] investigated the differences between hydrogen and deuterium loading in germanosilicate fiber preforms.
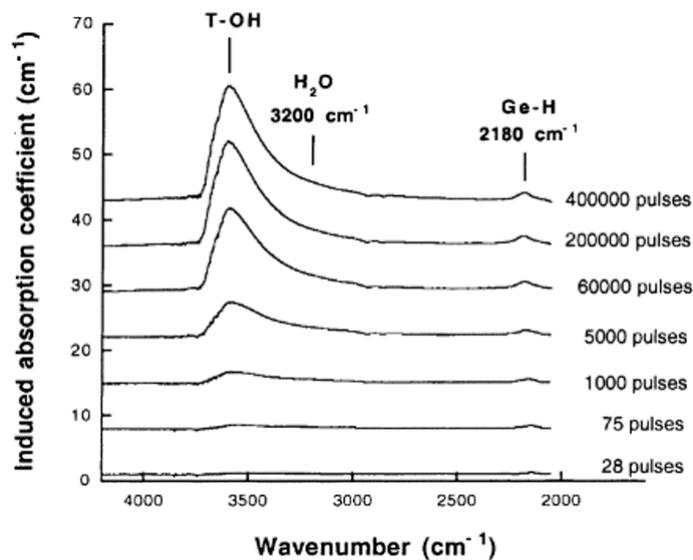
Figure 3.6.11: IR spectra of defect concentrations depending on the pulse rate. The UV exposure leads to the generation of different H-bearings, namely Ge-H ($2180 \, \text{cm}^{-1}$), H_2O ($3200 \, \text{cm}^{-1}$?) and T-OH (approx. $3600 \, \text{cm}^{-1}$, T = Si or Ge) [51].

As shown in figure 3.6.11, H-bearings are generated within the fiber with increasing number of pulses. Additionaly, he inscribed FBGs with the phase mask method and evaluated each peak intensity which are plotted in figure 3.6.12. Hereby, a linear correlation between the induced absorption coefficient and the refractive index modulation was found. These results were in accordance with the findings of Tsai et al. which also related GeH for the refractive index modulation in fiber Bragg gratings [48].
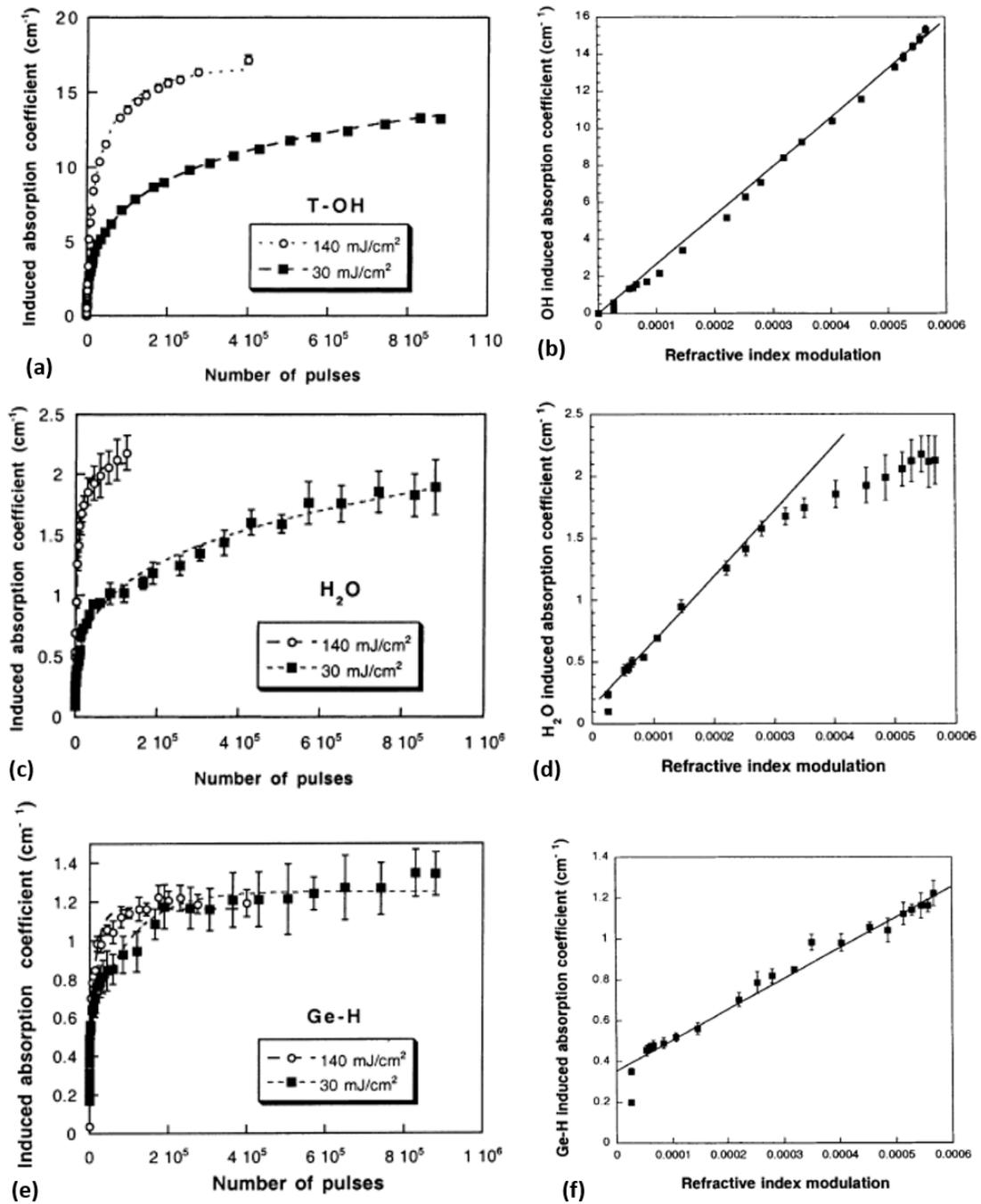
Figure 3.6.12: Left: IR peak intensity of H-bearing concentration depending on the number of laser pulses. Right: Increase of the refractive index modulation with increasing H-bearing concentration. Here, the data from the $140\,\mathrm{mJ/cm^2}$ was used [51].

Unfortunately, it was not discussed why the modulation caused by the molecular water is not linear for higher absorption coefficients. The effect of (periodic) molecular water as a reason for RFBGs was already suggested by Zhang et al. [30]. Furthermore, it was not discussed why the GeH concentration saturates and does not depend on the laser fluency during UV inscription.

However, Dalle et al. did not only investigate the occurance of H-bearings after UV

exposure but also their temperature stability. For this, they heated the samples up to 1200°C (heating rate not given) while measuring the induced absorption coefficient by FTIR. Hereby, they found that the amount of H_2O decreased rapidly until approx. 400°C while the hydride compounds (GeH) stayed constant up to approx. 400°C. Above 400°C the amount GeH started do decrease as shown in figure 3.6.13, b. While the hydride (GeH) and molecular water decreases completely until 400°C and 800°C, respectively, hydroxyl groups are stable and detectable until 1200°C, see figure 3.6.13 a.
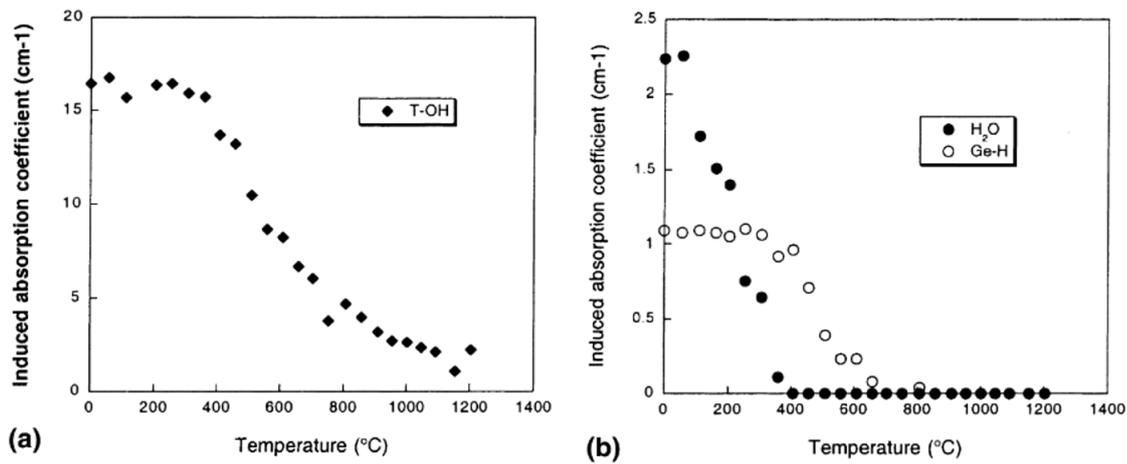
Figure 3.6.13: Temperature stability of UV-induced H-bearings in hydrogen loaded fibers. (a): Temperature stability of hydroxyl compounds (Si-OH and Ge-OH, respectively). Hydroxyl related compounds are stable until 400°C and subsequently decrease with increasing temperature. (b): Temperature stability of molecular water (H_2O) and germanium hydride (GeH). Molecular water shows a rapid initial decay with increasing temperature while GeH is stable up to approx 400°C [51].

The generation of H-bearings during FBG fabrication was further investigated by Lancry et al. [23]. In their work, they spatially investigated the effect (modulation) or H-bearings in a hydrogen loaded fiber preform (4.9 wt% Ge, 5 mm core diameter, 200 μm thickness). For this, they used a microscope coupled with a FITR spectrometer. This setup allows to investigate the spatial distribution along the fiber preform thickness with a resolution of 6.25 μm [23]. For the Bragg grating inscription, they used a frequency-doubled Ar ion laser (244 nm) together with a Lloyd interferometer to manufacture gratings with a period of $\Lambda = 20$ μm. The following inscription settings were used for the gratings:

Table 3.6.1: Inscription parameters used by Lancry et al. [11].

	Period (µm)	UV power density (W/cm^{-2})	Writing time (min)	Δn_{mod}
R1	20	18	30	$\approx 2 \cdot 10^{-3}$
R2	20	6	30	$\approx 10^{-3}$
R3	20	6	12	$\approx 5 \cdot 10^{-4}$
R4	20	6	3	$\approx 2 \cdot 10^{-4}$
R5	20	6	30	$\approx 10^{-3}$

The results of the measurements are shown in figure 3.6.14.
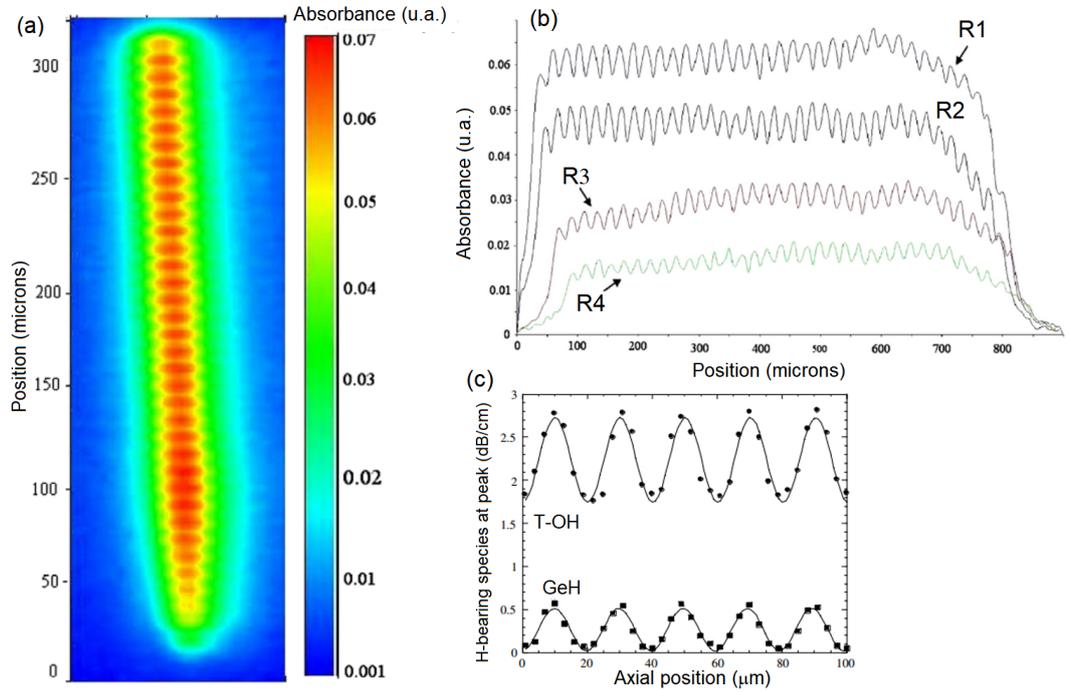
Figure 3.6.14: Spatially resolved FTIR measurements of H-bearing generation in hydrogen loaded fiber preforms. Plot (a) shows the 2D distribution of all H-bearings combined. Plot (b) shows the intensity cross-section of plot (a) for different inscription parameters. Plot (c) shows the spatially and compounend resolved intensity of the H-bearings [11].

Here, graph (a) is a 2D distribution of all H-bearings together (GeH, OH and H$_2$O) for the R1 grating in graph (b). Graph (b) shows the modulation of OH along the Bragg axis (pprofile of graph (a) along the fiber axis) with the labels according to table 3.6.1. Graph (c) shows the profile achieved with the setup for grating R5. Here, the modulation of the GeH species shows almost a perfect contrast (minima reaching zero) for the modulation (measured to be ≈ 0.7) whereas the modulation of the hydroxyl species (OH) shows a) a worse contrast (measured ≈ 0.2).

4 Phenomenological Macroscopic Characterization

In this section, we provide the macroscopic investigation on temperature characteristics of Bragg gratings that are linked through the following items: a) Why is the Bragg wavelength (center wavelength of the Bragg reflection) after the heating-cooling cycle always lesser to the one before? b) What causes the reduction of the line width and the recovery of the line width during regeneration? c) What causes the reduction of reflectivity and its recovery during regeneration? Some of these important questions are poorly understood and remain so far unanswered, albeit some progress has been made in order to understand the physics of the underlying mechanisms [8, 9, 28, 29].

4.1 Temperature dependent phenomenological study

A phenomenological measurement of temperature dependence of grating reflectivity is implemented using an erbium (Er) broadband 1530–1565 nm laser source. For high temperature regeneration experiments, shown in figure 4.1.1, a few meters long fiber having FBG is placed within the central heating zone of the furnace and temperature is ramped up between room temperature (RT) to $900\,^\circ\mathrm{C}$ ($\pm 1\,^\circ\mathrm{C}$) and stabilized before cooling back to RT. The reflectivity measurements are recorded in-situ with a constant heating rate of $25\,^\circ\mathrm{C}$ per minute and acquisition time of 10 seconds via a Burleigh WA–7000 Multi-Line wavemeter ($0.5\,\mathrm{pm}$ accuracy) and an optical spectrum analyzer (OSA).
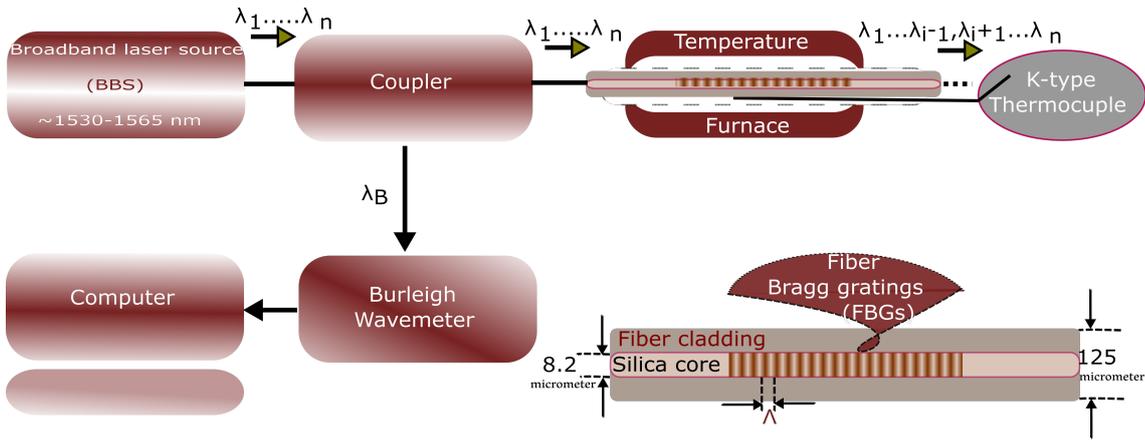
Figure 4.1.1: Setup used to measure fiber Bragg grating reflectivity.

Grating regeneration is a two-step process, an erasing phase and a subsequent regeneration phase, for example. To date, most of the grating regeneration is performed by ramping up to high temperature and isothermally holding when annealing until the seed grating is completely erased and regenerated. A subsequent thermal stabilization is applied to stabilize the "regenerated grating".

4.2 Peak-wavelength-detection algorithm

For a stable extraction of FBG results, a dedicated Matlab code is implemented and the data are imported into the program that runs the file of approximately 2305 spectral wavelengths and up to 15660 individual measurements. The software extracts the variable quantities, for example the reflectivity, the center wavelength and peak width that are the most critical parameters for an FBG. To detect the Bragg peak of the grating-reflected wavelength with minimum error, we take the wavelength where the spectrum exceeds the noise floor and the wavelength where the spectrum falls under the noise floor again and look for the middle knowing that the peak is symmetric. This algorithm also optimizes the general wavelength detection technique when the wavelength shifts to be monitored depend on: (*a*) peak shape and (*b*) data written by the spectrometer software which exhibits a spectral signal occasionally drops without signal to noise reduction. The Matlab code for center (Bragg) wavelength detection and the peak width extraction are tested with the following two algorithms:

(i) Weighted average algorithm

$$\lambda_B = \frac{\sum(P_i \cdot \lambda_i)}{\sum P_i} \tag{4.1}$$

where P_i and λ_i are respectively the power or intensity and the wavelength of the ith pixel number of CCD in the spectrometer.

(ii) Algorithm based on threshold relative to noise level

This algorithm is based on the determination of middle pixel position by taking the averaged value in the spectral interval between left (λ_{left}) and right wavelength (λ_{right}) about the peak above the local noise floor of the detector.

$$\lambda_B = \frac{(\lambda_{right} + \lambda_{left})}{2} \tag{4.2}$$

Or,

$$\lambda_B = \frac{1}{\lambda_{right} - \lambda_{left}} \int_{\lambda_{left}}^{\lambda_{right}} \lambda \, d\lambda \tag{4.3}$$

A dedicated algorithm of this type provided an efficient technique for the extraction of Bragg wavelength that defines our center wavelength in characterizing FBG as a temperature sensor. So, the expressions below are used to determine the peak width (Γ) around the peak maxima and the numerically integrated area (A) under the peak.

$$\Gamma = \lambda_{right} + \lambda_{left} \tag{4.4}$$

$$A = \int_{\lambda_{left}}^{\lambda_{right}} \lambda \, d\lambda - \frac{(\lambda_{right} + \lambda_{left})}{2} \tag{4.5}$$

Figure 4.2.1 shows that the reflectivity does not change until the grating starts decaying during the heating cycle up to the maximum temperature while the peak width (see figure 4.2.2), decreases noticeably above $300\,°C$ (see equation 2.7).

It can be further inferred from equation 2.8 that the time delay in change of the peak intensity comes from $\tanh^2$ dependence on the gratings. Upon isothermal annealing at $900\,°C$, both, the reflectivity and the peak width continue to diminish until they completely disappear in the noise floor indicating that the FBGs get erased by a thermally activated process. After a decay time of a couple minutes, both the reflectivity and peak width reappear and continue to grow linearly until they sufficiently stabilize to the maximum value, then decay again but at a much slower rate. This process is known as FBG regeneration. At $900\,°C$, there is a continuous blue shift in center wavelength during the regeneration and the overall change upon cycling to ambient temperature is $\approx 1\,nm$. This indicates that the average glass structure has altered properties that see a decrease in the core refractive index (equation 2.3).
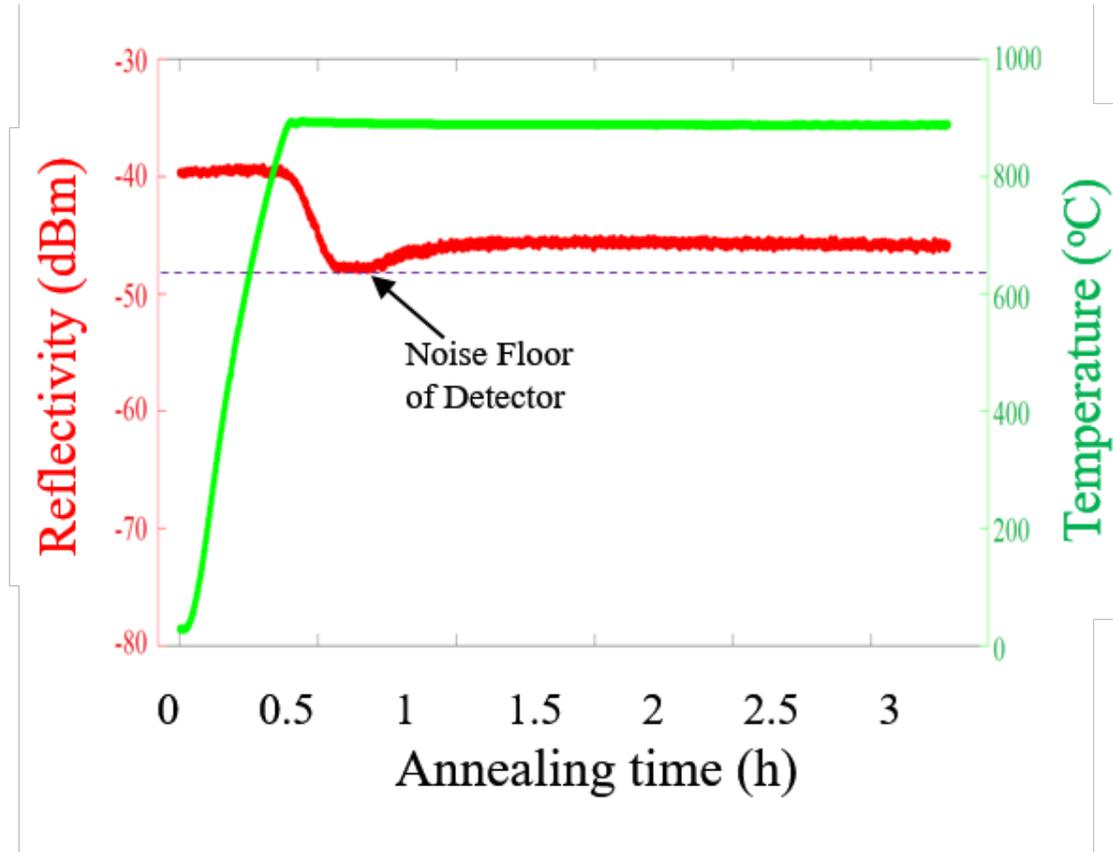
Figure 4.2.1: Reflectivity (red) as function of annealing time and temperature [a semi-log graph]. The time at which the reflectivity reaches to its minimum value corresponds to minimum detectable reflectivity or the detector's noise floor which also means that it is not the the absolute FBG reflectivity that is important but it is rather the signal to noise ratio with which the Brag signal is measured that matters.
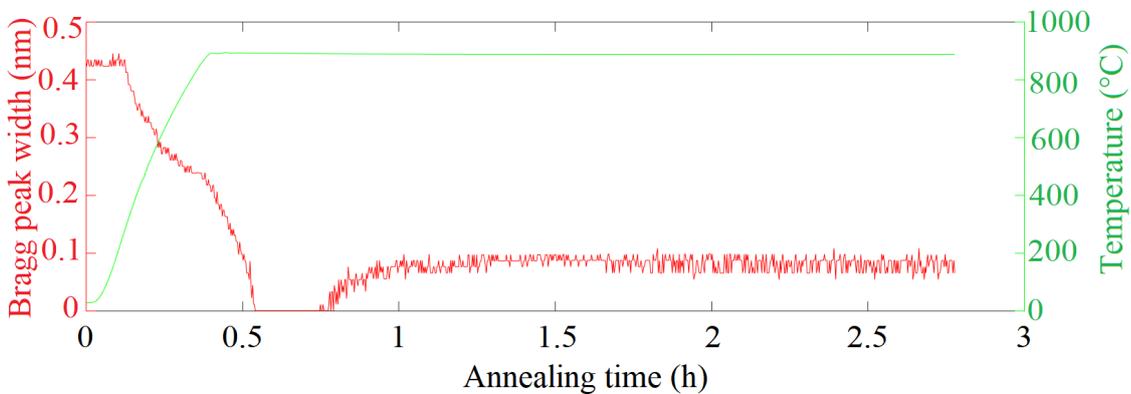
Figure 4.2.2: Peak width (red) as function of annealing time and temperature.
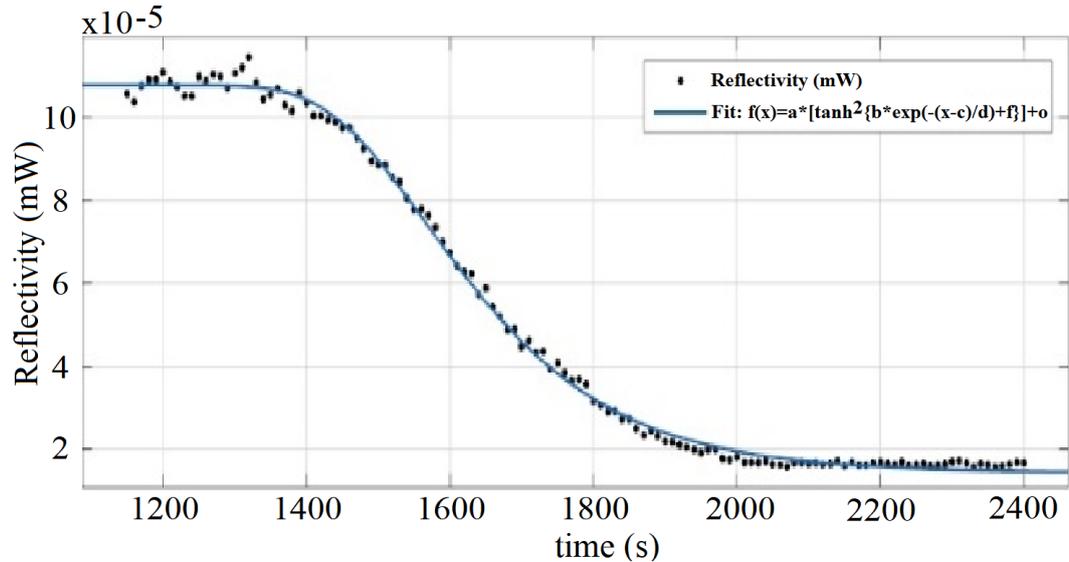
Figure 4.2.3: The $\tanh^2$ behavior of the reflectivity as function of time, showing the initial decay of FBG with the data set cut at $t = 2400\,s$ as it hits the noise floor before the regeneration (Here, the reflectivity in y-axis is transformed into a linear scale from figure 4.2.1).

The fitting result (figure 4.2.3) for the reflectivity is based on the highly non-linear hyperbolic tangent squared i.e., $\tanh^2$ and an exponentially decaying argument, which essentially reflects a thermally activated decay of the refractive index modulation. This provides six fitting parameters (amplitude and y-offset for the $\tanh^2$ as well as amplitude, x-offset, y-offset, and decay time constant for the refractive index modulation of the core).

4.3 Calibration of fiber Bragg grating sensor

A calibration analysis is performed to monitor the center wavelength (λ_B) shifts and to investigate the sensing capacities of FBGs structures subjected to changes in repeated temperature cycles between 25°C and 1000 °C. The calibration curves are obtained to test the characteristics of RFBG sensors, for example, drift, shorter and longer term stability etc.
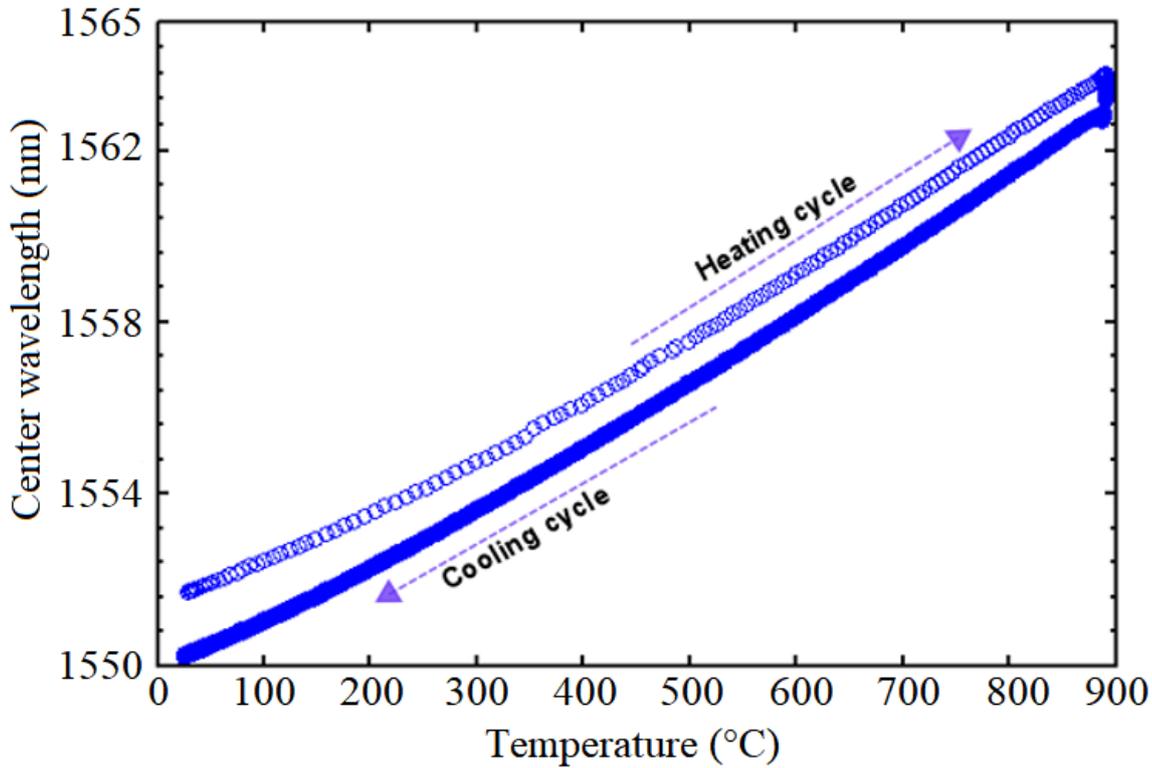
Figure 4.3.1: Central wavelength as function of temperature.

The result presented in figure 4.3.1 shows that FBGs exhibit a thermal response upon heating to 900 °C and subsequent cooling back to ambient temperature. During the FBGs heating between RT to 900 °C, the Bragg wavelength (λ_B) increases almost linearly, reaches a maximum value and upon cooling cycle between 900 °C to RT, the $\Delta\lambda_B$ reverses and passes the original starting point, signaling a net reduction in the fiber core index. For a wavelength of 1550 nm, the observed temperature sensitivity is approximately 13 pm/K. All correlation coefficients are very close to unity and errors much smaller than 1 °C. These errors are a combination of the uncertainty of the interrogation system, (± 1 pm) and of the thermometer used. Using the FBG's average sensitivity of 13 pm/K results 1 pm in error that means a temperature uncertainty of about 0.08 °C, which is much smaller that the error produced by the thermometer. As such the high precision measurement with a repeated thermal cycling at high temperature is obtained in regenerated FBGs that require a long-term heat treatment at various temperature. The calibration studies also show how accurately the FBG–thermometer reads the temperature from wavelength detection as the error produced within the measurement is much smaller and yields a simple thermometer configuration of high resolution, linearity, and measurement repeatability. These features of FBG-thermometers, make them highly desirable for ultra-high temperature sensing. Such property is the consequence of the thermo-optic effect which is an important physical parameter of the glass fiber.

Effects of temperature

The grating regeneration is a two step process (first the erasure phase and subsequent regeneration phase) under a carefully chosen annealing temperature that can significantly affect the end–result and therefore will be further investigated. For example, if we consider a particular fiber type, hydrogen loading and the 'seed–FBG', is it possible to:

(i) initiate regeneration at any desired temperature? And eventually

(ii) optimize that process in terms of either time taken or strength desired?

To provide answers to the above research questions, the annealing characteristics (decay mechanism and stability analysis) of the type–I gratings in hydrogen loaded Ge–doped silica fiber (iXFiber, refer to section 3.1) are investigated. The 'seed–gratings' having similar transmission depth (-33 dB) are isothermally annealed at respective temperatures (between 700–$1000\,^\circ$C) in the oven and the regeneration of gratings are investigated showing that the higher the temperature the grating has seen during the cycle, the less remains of it as seen from the plot of signal recovery (reflectivity obtained after a complete erasure of seed) as a function of annealing temperature for the six gratings (figure 4.3.2). The good regeneration–efficiency of $\sim 85\,\%$ at $700\,^\circ$C (data point labelled "I"), $\sim 50\,\%$ at $775\,^\circ$C (data point labelled "II") and a minimum of $\sim 10\,\%$ at $1000\,^\circ$C have been successfully obtained, plot 4.3.2. The symbols "$\Diamond$" and "$\triangle$" denote the values corresponding to a good remaining reflectivity after a long stabilization at $1000\,^\circ$C.
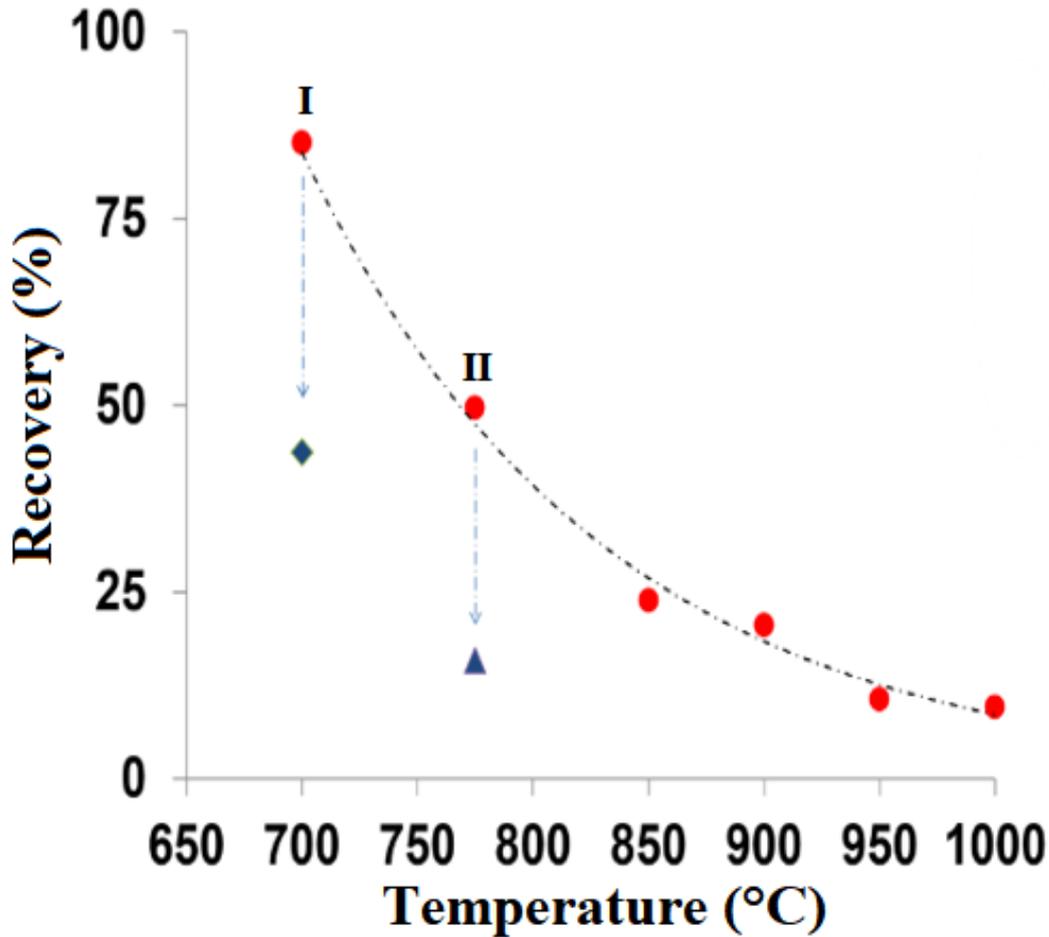
Figure 4.3.2: Recovery as a function of annealing temperature [28]

The time required for regeneration at $700\,°C$ is $450\,h$ and that at $1000\,°C$ is only $1.3\,h$ that are plotted in figure 4.3.2. It shows that the slower relaxation with longer wait times at lower temperature, however, leads to stronger regenerated gratings (through higher index modulation? or refer to the explanation of figure 4.3.6). This also means that there is no limit other than time in terms of obtaining maximum regeneration. Therefore, the enough heating–time would be required in order for a complete grating regeneration to happen. The recovered or regenerated grating strength is listed here.

- Final reflectivity at $700\,°C \sim 85\,\%$

- Final reflectivity at $775\,°C \sim 50\,\%$

- Final reflectivity at $1000\,°C \sim 10\,\%$

Grating stability at $1000\,°C$

The RFBG is exposed to $1000\,°C$ for long–*term* stability test after regeneration at $700\,°C$ and $775\,°C$, shown in figure 4.3.3. It is also interesting to note here that

there exists new regeneration regime that occurs only in grating regenerated above 775 °C, as dictated by first decay and the subsequent slower one (labelled as "II" in the plot 4.3.3). Overall, there remains issue regarding stability associated to the grating regenerated at 775 °C, in fact more than 10 dB loss in 50 h period, to survive at 1000 °C environment. On the contrary, the one (labelled as "I" in the plot 4.3.3) regenerated at 700 °C, retains a good remaining reflectivity (refer figure 4.3.4), staying strong enough to stand high heat load of 1000 °C.
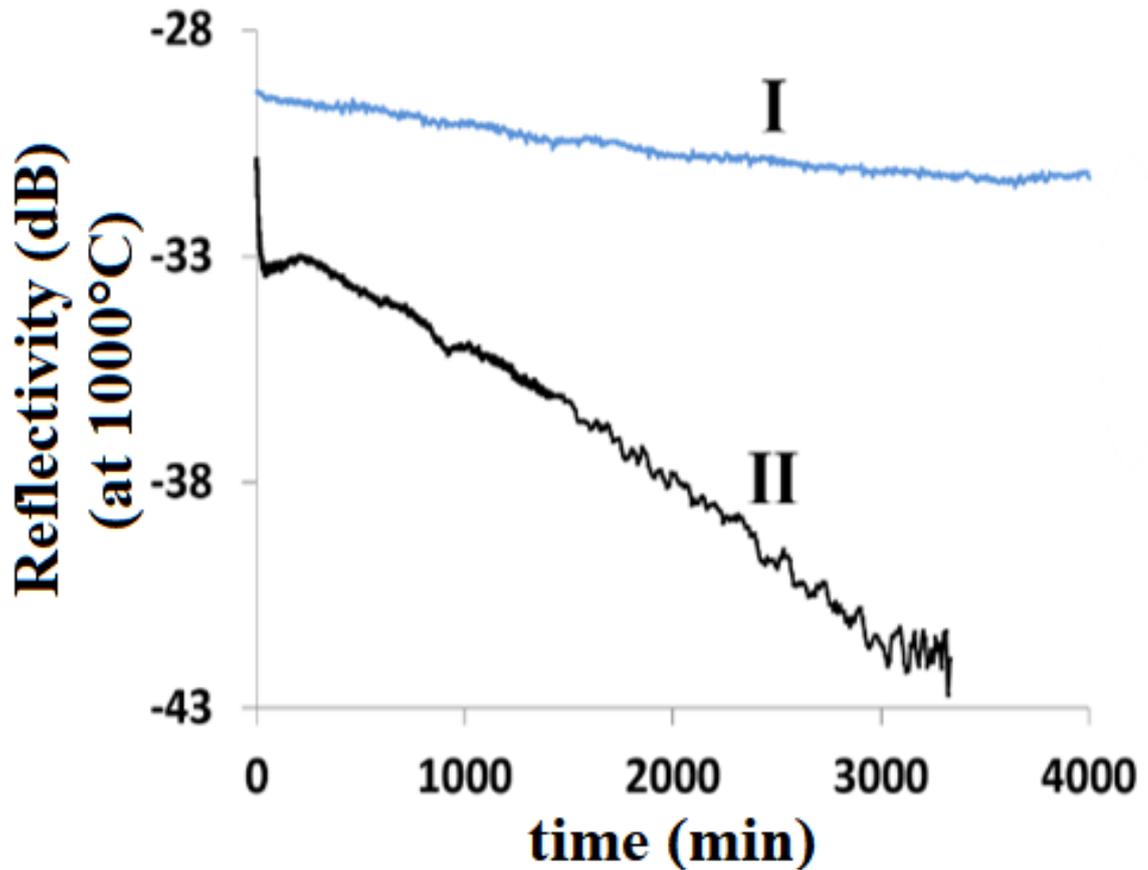
Figure 4.3.3: Recovery stability as a function of annealing time during regeneration, the plots labelled "I" and "II" corresond to the data points in figure 4.3.2 [28].

A high degree of RFBG stability is obtained from the tests conducted at 1000 °C, shown in figure 4.3.4. The good remaining reflectivity secured at the end of long–term annealing is listed here, where the percentage values correspond to 'dB' scales displayed in the figure.

1. Final reflectivity with dwell time of 500 h (regenerated at 700 °C) ∼ 44 %

2. Final reflectivity with dwell time of 140 h (regenerated at 775 °C) ∼ 16 %
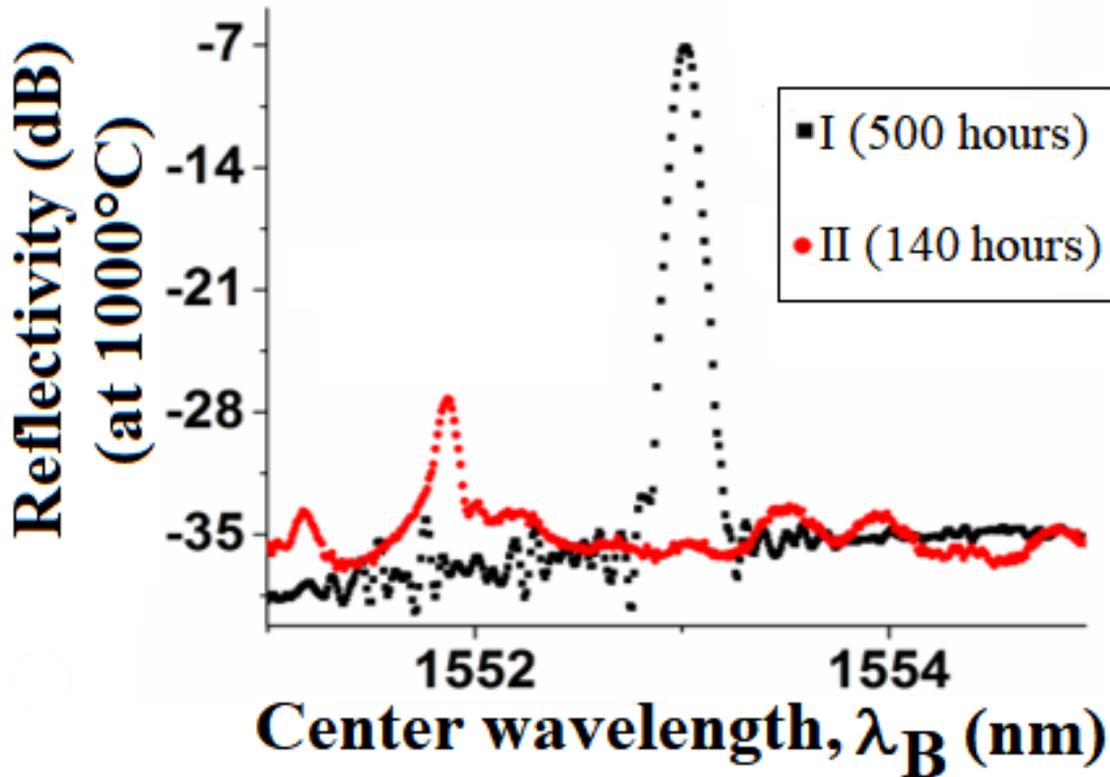
Figure 4.3.4: Long–term stability test of grating reflectivity [28]. A higher signal to noise ratio of RFBG (regeneration performed at 700 °C, black curve compared to regeneration performed at 775 °C, red curve) is obtained from the post-thermal stability tests conducted at 1000 °C.

Arrhenius–type temperature dependence

The Arrhenius–like exponential decay from figure 4.3.5 reveals that the slower relaxation at low temperature leads to produce stronger regenerated gratings. The energy value is due to diffusion reaction dynamics within the grating region (figure 4.3.5) wherein the error bars are calculated from the variation of background levels and recovery time [28]. For this, the efficient diffusion species in silica fiber, such as hydrogen and oxygen, assume a particular importance in the characterization process even in fibers without hydrogen–loading condition as hydrogen being both the most common impurity plus reactive as well as the oxygen species are reactive in silica fibers upon annealing. From figure 4.3.5, one can estimate the regeneration time by extrapolating the curve to any desired temperature and thus this serves as a blueprint. The exact nature of the underlying microscopic mechanism behind the thermally activated process, however, still remains to be determined.
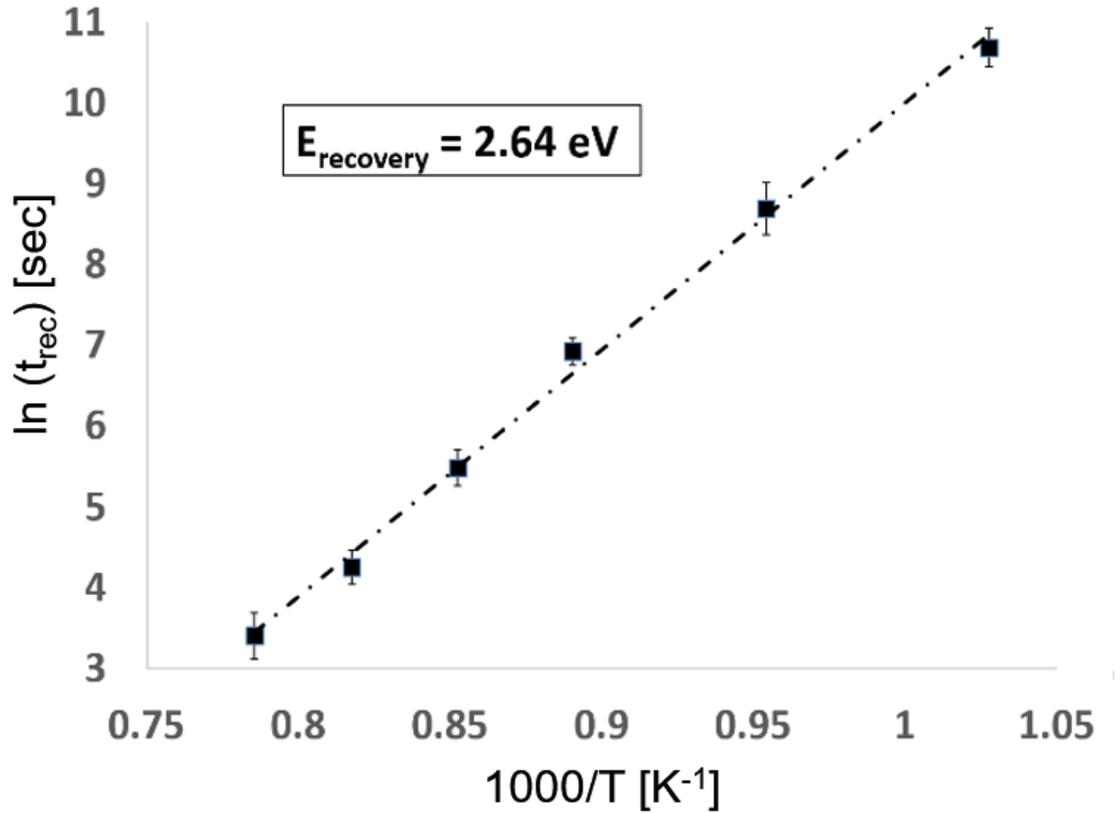
Figure 4.3.5: Thermal activation energy diagram [28]

To sum up, it is imperative that the FBG structure as the thermometer configuration be usable in environments to higher temperature regime beyond 1000 °C and for this, the solution is provided based on thermal regeneration process of fibers containing FBG. In the next section, I will address the challenge regarding memory reflected by the grating regeneration by introducing second grating and cover the qualitative observations through this simple model.

A competing gratings model

The results have shown that the change in grating strength or the rate of regeneration can be determined by a different temperature being isothermally maintained with a nominal wait time, and the subsequent thermal cycle seem like further stabilizing the index change of glass in the grating–mirror–region of the fiber so that a good regeneration can be realized after a stabilized properties of RFBG. Consider an example of a good regeneration obtained at 700 °C with a good–remaining–reflectivity and further test performed at 1000 °C, as discussed above. This section therefore attempts to provide the development of a model for validation of the observed grating regeneration behavior. The proposed model describes the dynamics of the grating
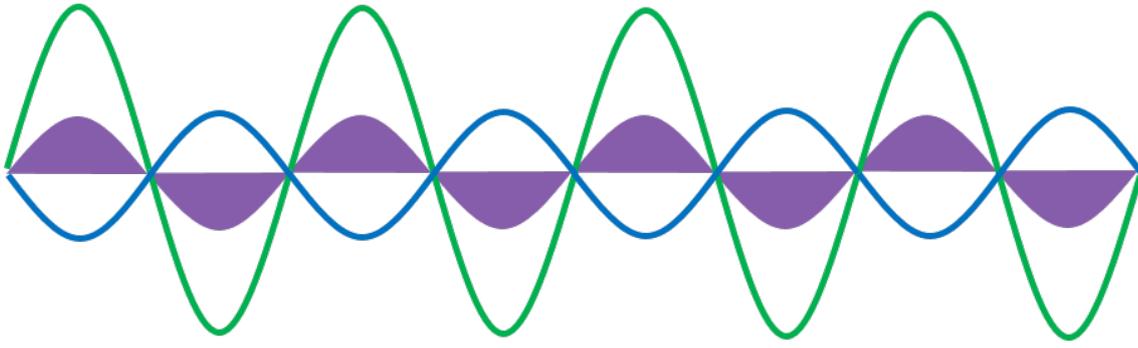
Figure 4.3.6: Schematic illustration of antiphase gratings. This is to note here that in reality the periodic gratings would show only one half of the index modulation because of the UV writing procedure.

erasure and regeneration processes encountered in the experimental behavior and thus the insight into the memory to generate a new grating after the initial one gets erased. By annealing at low temperature with long wait time, we can produce an optimized regeneration strength from a seed FBG, which means that the temperature at which a seed gratings undergo erasure and regeneration and thus a growth phenomenon not necessarily starting at zero — but it is initiated from remaining net index modulation. It can be explained by two complementary gratings where only one survives, based on the following assumptions:

(i) The initial grating essentially consists of two parts, $(\Delta n^+_{mod_1}$, green line in figure 4.3.6) and $(\Delta n^-_{mod_2}$, blue line in figure 4.3.6), having different activation energies that are both built during the inscription so that the positive stronger–index modulation $(\Delta n^+_{mod_1})$ of a dominant component can be realized.

(ii) The two antiphase grating components then add up making them physically indistinguishable at ambient temperature as represented by the smaller, purple colored region in figure 4.3.6.

(iii) The stronger grating with positive index modulation has lower thermal stability; therefore, if subjected to thermal cycling for a sufficient time it yields a weaker–index modulation and finally, the regeneration stage comprises of a negative grating structure $(\Delta n^-_{mod_2})$ having higher thermal stability. The amplitude of total index change $(\sum(n)$, red solid line) corresponding to positive $(n^+$, green solid line) and negative $(n^-$, blue right pointing curly bracket) index modulation is shown in the diagram 4.3.7. It is to note that the trend lines in the diagram 4.3.7, representing time–dependent index change responsible for peak width and reflectivity– decay, are only scaled to 'approximate'.
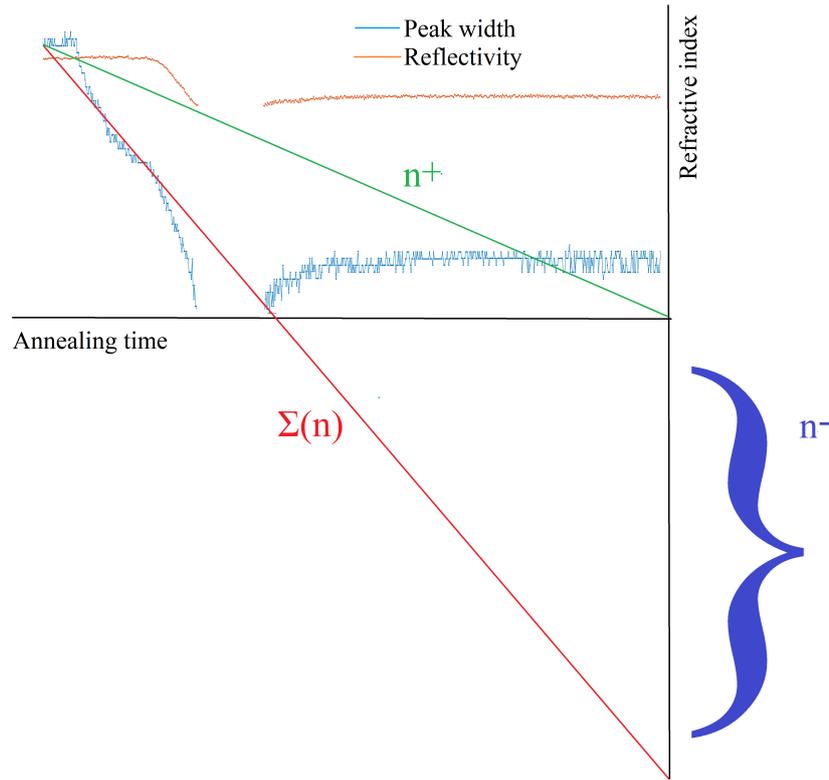
Figure 4.3.7: Schematic representation of the competing–gratings model.

Under these assumptions, the reflectivity measurement at the ambient temperature typically starts with the net index modulations in the fiber core, 4.3.6. The delay time for change detections for reflectivity value during annealing above a threshold temperature, 300 °C where a remarkable index drop (Δn) was observed. This is due to the dependence on the refractive index modulation (follows from equation 2.7) while only the real arguments within the complex hyperbolic function show an immediate substantial temperature response with no time lag. From figure 4.2.2, this observation becomes more evident, when T increases, the signal peak shrinks in width (that follows from linear equation 2.8) far below the regeneration regime, so called 'regeneration temperature' so that no direct effects emerged through grating reflectivity value, but it could imply only the observed time dependent changes with some delay.

The onset of rapid decay of signal peak width around 300 °C is the consequence of net index modulation that drops down faster mainly due to the degradation of less stable (n^+) index modulation. Upon isothermal annealing at 900 °C, the less stable (n^+) index modulation continues to decay which is responsible for the reflectivity signal dropping further down at maximum temperature.

The decay of both the signal peak width and reflectivity persist and eventually disappear into the noise floor for the scenario in which two competing gratings that
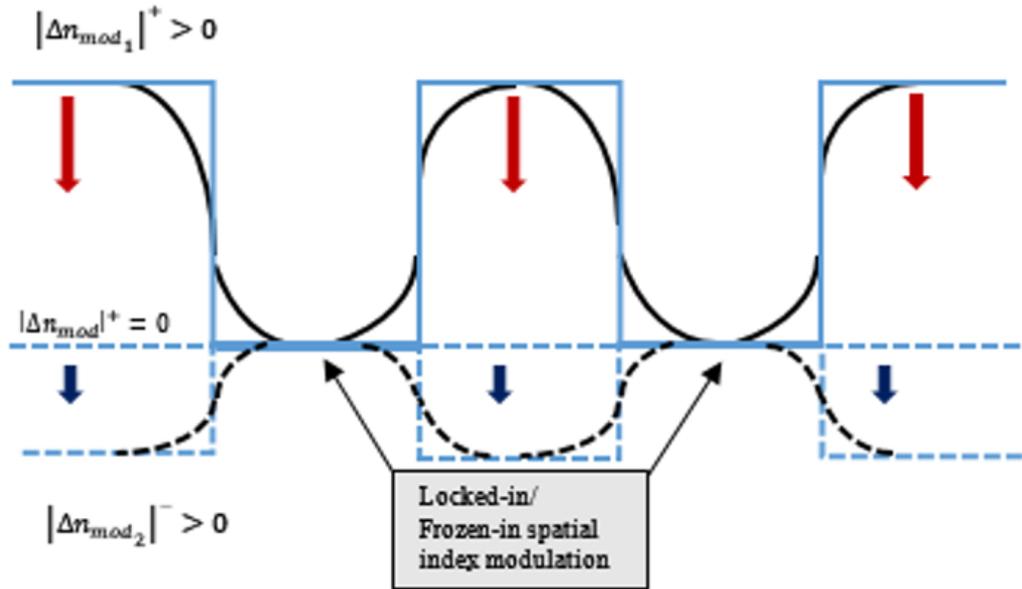
Figure 4.3.8: Schematic illustration of the competing–gratings.

appear with equal strength in antagonistic manner. At this stage, the net index modulation in the fiber core becomes sufficiently weak for the detector to distinguish the intensity in the peak relative to the local noise floor. After continuously holding the fiber upon isothermal annealing, the total index modulation dominates the weaker index modulation for the scenario in which the grating manifests itself as a recovery of the reflected signal. The recovered signal is stable due to the higher thermal stability of the precipitated index modulation.

The other possibility to present this dynamics of grating erasure and rebirth is also shown in figure 4.3.8 where a sinusoidal refractive index modulation (black solid and dotted lines) is primarily due to a possible reduction of anharmonic orders in the spatial modulation of the FBG. The regeneration behavior of competing gratings relies on net refractive index modulation. Since the reflectivity is the consequence of refractive index modulation (Δn_{mod}), the fundamental question regarding the mechanism of regeneration or in other words, the memory to generate a new grating after the initial one gets erased is addressed through the introduction of a second grating that coexists from the very beginning and which is of opposite phase to the first while having a stronger thermal stability.

Discussion

The thermal decay in the sensing capabilities of standard (type–I) FBGs limits the use of sensors to less critical applications with operation temperatures below $200\,^\circ$C.

Efforts in the last decade led to the development of new types of gratings where the most promising results are obtained for RFBG sensors which can withstand temperatures above 1000 °C. The processing of RFBG sensors involves a post inscription annealing treatment during which the reflected signal initially decays below the noise level and then recovers to a value inferior to the original grating (typically <40 %). However, the main mechanism for thermal regeneration process is not completely understood, hence the need to develop approaches to increase the recovery rates and long-term stability.

At 900 °C, there is continuous blue shift in central wavelength during the regeneration indicating that the average glass structure has altered properties that see a decrease in the core refractive index. The temperature calibration curves are obtained to test the characteristics of RFBGs. This was done through a dedicated program in Matlab to automatically extract all relevant experimental parameters from a time– and temperature–dependent sequence of spectra. New methodology was established to enhance the recovered reflectivity of FBGs. An inverse relationship between temperature and regeneration efficiency is determined and identified through slowing down the regeneration performance, which increases the recovery efficiency and achieved over 85 % of the seed–grating. Importantly, the advantage of the slower regeneration cycle is also preserved in long–term stability measurements at 1000 °C over 500 hours, thus enabling potential application for the development of fibers resistant to high temperatures. In addition, a new approach that allowed us to determine the activation energy of regeneration mechanism (following an Arrhenius behaviour) also led us to predict the onset of regeneration of reflected signal with high accuracy. The experimental findings are discussed based solely on either diffusional transport or stress induced densification. Finally, with the reflectivity and the peak width as an observables, we derive a simple, phenomenological and quantitative model yet able to accurately explain the regeneration process regarding both the disappearance and the recovery of FBG reflectivity shedding light regarding temperature impact on time dependent fiber glass inside–structure (for example, refractive index).

5 *In–situ* Spectroscopic Characterization

5.1 Measurement setup

The *in–situ* measurement setup (shown in figure 5.1.1) consists of a 473 nm diode pumped solid state single mode ^{00} laser from Cobolt Blues which is linearly polarized. After the laser, a fiber launching system from Thorlabs is installed which allows a coupling from a free beam path into a cleaved glass fiber. The fiber launching system consists of an objective ($\times 4$ magnification and $0.1 NA$) and a three dimensional micro screw stage which allows to align the fiber with micrometer precision. Choosing a collimation lense with NA close to the fiber's NA allows to match the laser spot to the core size. Given that 473 nm is far below the single-mode cut–off wavelength of each fiber, the fiber exhibits multimode operation where each optical mode can be thought of as a ray of light.
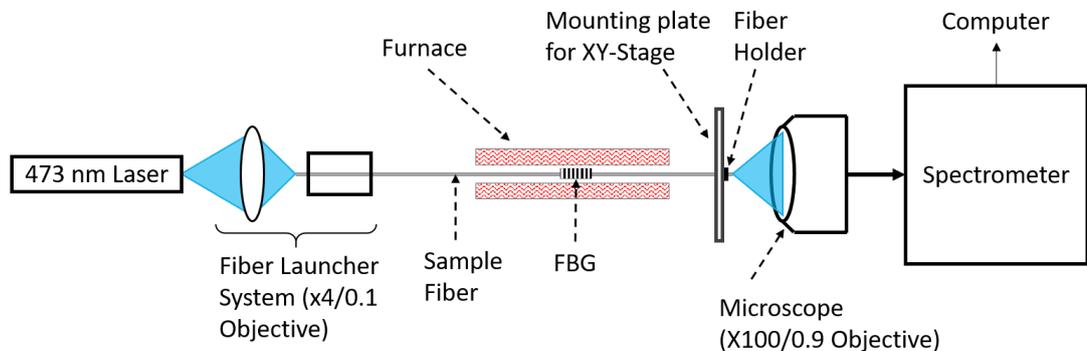
Figure 5.1.1: *In situ* measurement setup consisting a 473 nm diode pumped solid state (DPSS) laser, a Thorlabs fiber launcher, a high temperature furnace, a confocal microscope and the Horiba spectrometer with the CCD camera.

The fiber then transits the high temperature tube furnace (GSL–1100 $\times$) from MTI Corporation, which has a constant heating zone of approx. 10 cm where the fiber is placed so that the FBG remains in the center of the constant heating zone. After the furnace, the cleaved fiber is held with a fiber clamp to ensure all scattered light of the fiber is collected by the microscope. The microscope (Olympus BX–41) has a

high NA objective ($\times 100$ magnification and 0.9 NA). Lastly, with the appropriate notch filter Raman scattered light is collected from the microscope to the spectrometer (Horiba iHR320) and CCD camera (Horiba QExtra Synapse) which employs thermoelectric cooling. Each pixel size of the CCD detector is 26μ so the Raman peak intensity is the measure of the number of photons per CCD pixel, measured in arbitrary unit.

5.2 Raman measurements

For the Raman measurements, the short fiber pieces with the hydrogen inscriped FBGs (approx. $50\,\mathrm{cm}$) are spliced to bare fibers of the same type using arc fusion splicing device from Fujikura (FSM–30s). The final sample consists of approx. $3\,\mathrm{m}$ of glass fiber and is cleaved on both ends to ensure a good in– and out–coupling behavior. Capturing Raman data on the sample generally requires two treatment steps (i.e., silicon calibration and spectral decomposition).

(i) Silicon calibration

Example of our calibrated silicon reference sample is shown in figure 5.2.1.
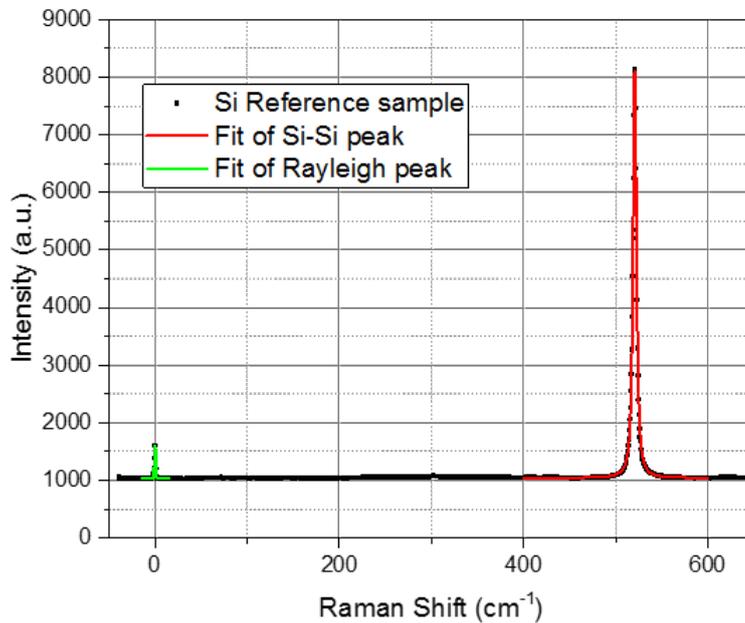
Figure 5.2.1: Calibrated Si–Raman spectrum: $520.7\,\mathrm{cm}^{-1}$ band is assigned to the Si–Si bond and $0\,\mathrm{cm}^{-1}$ to the suppressed Rayleigh scattering.

The calibration measurement is done using silicon reference, before and after conducting Raman scattering experiments on the fiber samples, from which both Rayleigh

and silica line shapes are fitted using a Lorentzian model to extract their positions. Then, the Rayleigh peak of the spectrum is shifted to zero (green peak in figure 5.2.1) and then stretched so that the Si–Si peak is at $520.7\,\mathrm{cm}^{-1}$ (i.e., transverse optical mode). These two obtained factors (Rayleigh shift and stretching) are then applied to calibrate the Raman measurements of the fiber samples.

(ii) Statistical analysis of spectral elementary decomposition

Example of an ambient spectrum acquired in the wavenumber range between $0 - 1500\,\mathrm{cm}^{-1}$ and the deconvolution into Lorentzian peaks is shown (figure 5.2.2).
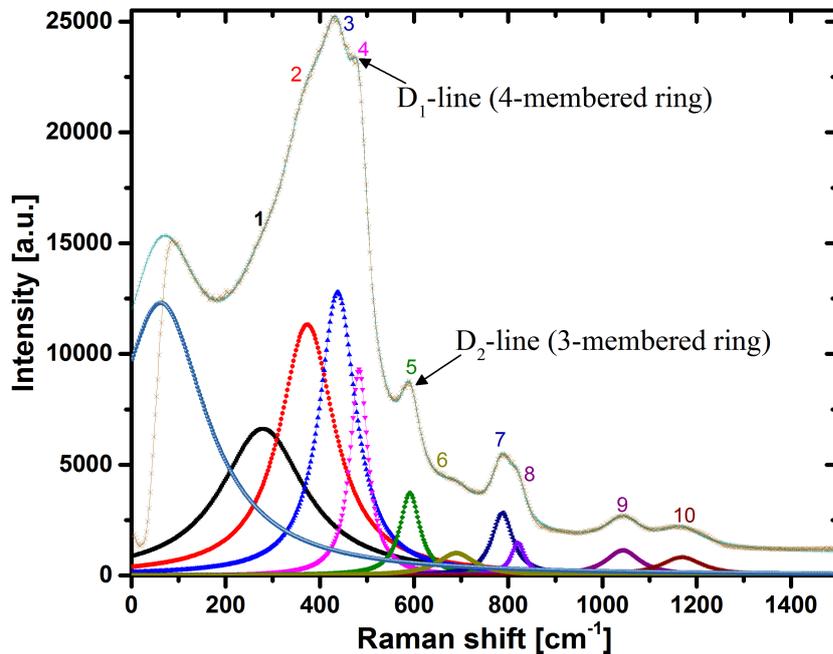
Figure 5.2.2: Raman scattering spectrum at ambient temperature with deconvolution of Lorentzian lineshape (peaks correspond to the identifications in iXFiber sample presented in Table 5.2.3) [97, 98].

We exclude the physics of low frequency $(<100\,\mathrm{cm}^{-1})$ Raman spectra, containing a prominent glass features so–called Boson peak (BP) that has complex physical origin. Thus, we chose to deconvolute the continuous Raman spectrum of a fiber into constituent peaks, to track specific vibrational information of different chemical bonds on the Raman scattering profile. All the observed Raman spectra are fitted using a least squares routine to a superposition of peaks and these component bands are labeled by Arabic numbers $\#\,1$, $\#\,2$, $\#\,3$,.. $\#\,10$ in order of increasing frequency. The assignments are summarized in Table 5.2.3.

Band index/ frequency (cm⁻¹)	Assignment
Boson peak: ≃ 60	Universal feature of glass
Band 3: ~440	6-membered SiO₄ ring (main band) (superposed to 5- and 7-membered rings: components 1 and 2 in the deconvolution)
Band 4: ~495	4-membered ring defect (D₁ line)
Band 5: ~605	3-membered ring defect (D₂ line)
Band 7 } Band 8 750-850	Transverse optical (TO)/ longitudinal optical (LO) split (bending movement of bridging Oxygen)
Band 9 } 1060 Band 10 1190	TO/ LO split (asymmetric stretching movement of bridging Oxygen)

Figure 5.2.3: summary of Raman band assignments [97].

After the curve-fitting routine replicated for multiple data sets on the high temperature spectra, our attempt is to track any spectral changes as a function of temperature. We employ measurements under heat treatment in the room temperature to 1000 °C range and for this the quantitative analysis of the characteristic peaks with significant overlap, the peak heights, peak widths and peak positions are extracted [97].

Effects of temperature and annealing time

In the following section, the disucssed results are for samples with and without FBGs (iXFiber, PS1250/1500 fiber, SMF fiber, GF1B fiber). For this, a volume fraction of the total fiber is kept inside the heating zone of two types of electric furnace: a) 75 % of PS1250/1500 fiber in a muffle furnace (SNOL 8.2/1100 LHM01) and b) 0.5 % of SMF28–FBG and GF1B–FBG in a tube furnace (GSL–1100X–UL) that has an internal K–type thermocouple to measure temperature with an accuracy of ± 1 K [97]. The details of the fiber properties are provided in section 3.1.

(i) iXFiber

Figure 5.2.4(a) shows the Raman intensity–map over the extended temperature range reaching 1000 °C with the baseline corrected spectra, visualized in the time–dependent Raman shift 2 D image. The x–axis is the annealing time (in hour), the y–axis is the wavenumber (i.e., the Stokes Raman shift in cm⁻¹), and the z–axis (color bar) corresponds to Raman intensity. As outlined in the upper panel of figure 5.2.4(a), it involves mainly three measurement steps: constant rate heating and cooling cy-

cles on the right and left–sides, and isothermal annealing steps on the middle part. One can see subtle changes in Raman intensity visible on either sides of the map during annealing and cooling steps where these time scales on the x–axis are too small to observe. However at this point the observed spectral changes follow from anharmonicity and Bose–Einstein thermal population factor, this temperature and frequency dependence were not corrected in the present study. Moreover, as such spectral variations become particularly evident immediately at the beginning of annealing through few hours that reveals there is change of vibrational signature during annealing step, this effect decreases following the glass structural relaxation during annealing at 1000 °C, shown in figure 5.2.4(a) [98].
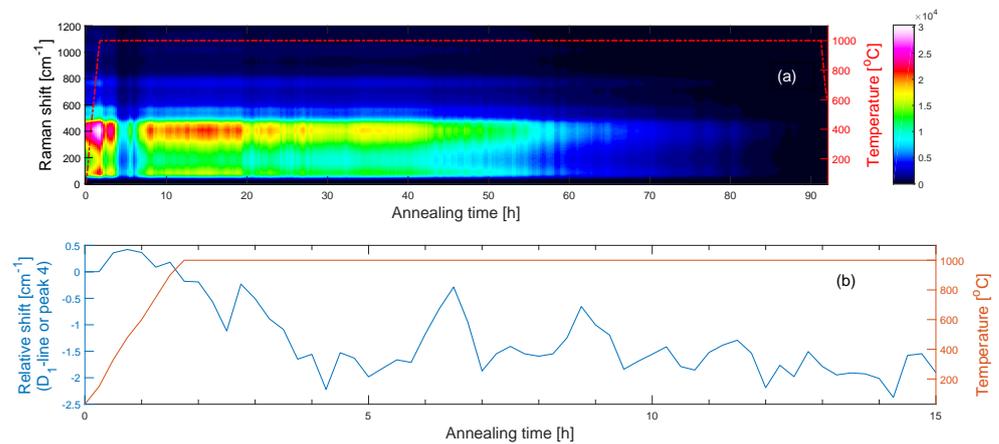
Figure 5.2.4: (a)Raman intensity map: Temperature evolution (between ambient to 1000 °C) and time evolution of Raman spectra (89 h 35 min isothermal annealing at 1000 °C) and (b)The vibrational displacement of D1 phonon band (peak 4 in figure 5.2.2) as a function of annealing time where the first four hours of Raman shift under an isothermal annealing invokes the independent measurement technique to extract the thermal expansion of chemical bond in fiber that primarily results from strain effect [98].

The change of intensity up to the point of complete loss of signal is primarily due to thermal drift of the coupling unit from the fiber to the microscope objective and

into the spectrometer. This occurs as an unintended consequence of measurement artefact in an experiment set up with less than $10\,\mu m$ precision over a time span of $3\,$days. The minor variations (periodic noise) along the time axis in figure 5.2.4(a) are due to a numerical interpolation of the data. At $1000\,°C$, due to the change of resulting stress inside the fiber (i.e. between core and cladding), the interface structures may be modified and relaxed. The overall glass relaxation is strongly influenced via thermo–optic effect that presumably reduces the index gradient around core-cladding interface and partly via cladding thermal expansion that also extends the inner glass portion of fiber. On the other hand, the variation in the structural relaxation can also result in a large difference in the fictive temperature between core–cladding regions consequently inducing strain in the network structures. Authors have made similar observations of strain effects in bulk glass, fiber silica glass and silica glass arc tube studies.

In figure 5.2.4(b), a subset of the data in 5.2.4(a), we fitted Lorentzians to the raw spectral data for the full heating cycle. The appreciable structural changes are observed within the core of the fiber as a function of time with increasing temperature and upon isothermal annealing at $1000\,°C$. These changes are manifested as modifications of atomic arrangements associated to D1 defect line in four fold rings. In fact, such an observation of the vibrational displacement associated to D1 band is a remarkable evidence to independently extract a thermal expansion in optical fiber. The increased anharmonicity, decrease in the Si–O–Si angle and increase in the Si–O bond length have been interpreted to account for the thermal expansion associated to high frequency bands [98].

On the one hand this also opens a new possibility to determine the thermo–optic value through temperature dependent Raman study. It is important to note here that we are investigating the shift of the peak labeled '4', the maximum of which is sitting on the negative slope of peak '3', figure 5.2.2. We are aware of the delicate procedure of extracting shifts and parameters under these conditions but we would like to emphasize the following: Figure 5.2.4(a) indicates a decrease of intensity of peak '3' within the first $4\,$hours. In such a case, the position of the maximum of peak '4' should experience a shift towards larger wavenumbers, simply because the slope on which it is sitting (the negative slope of peak '3') is decreasing. We do however observe a significance shift to smaller wavenumbers, even against the changing background slope imposed by peak '3'. As a result, we consider this shift of peak '4' a) real and b) significant, as our fitting method is underestimating the real amplitude of this effect.
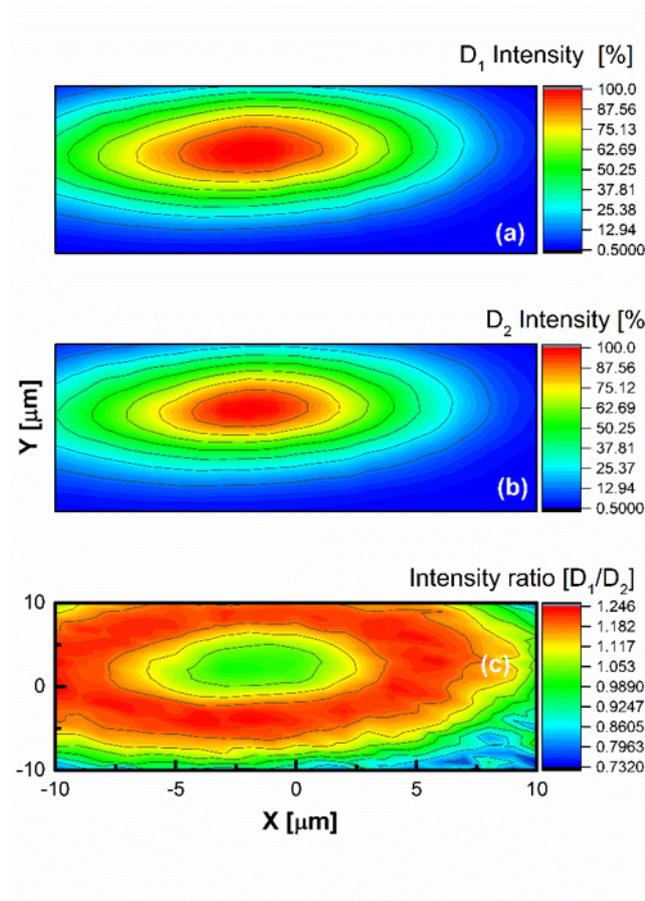
Figure 5.2.5: Raman intensity map across a fiber end of a)D1 band, (b)D2 band and (c)D1 and D2 ratio. The intensities of the two components are obtained from spectral deconvolution [98].

Figure 5.2.5 provides the Raman intensity map of D1 and D2 bands for which spectra are acquired from a $20 \times 20 \, \mu m^2$ transverse cross section of a cleaved fiber end at $1 \, \mu m$ distances in X and Y–directions. The center of the map is the fiber core (diameter $9 \, \mu m$) that is surrounded by a cladding ring. The intensities of D1 and D2 components are obtained from the curve fitting shown in figure 5.2.2, and normalized to a maximum intensity of 100. Figure 5.2.5(a) and 5.2.5(b) present the D1 and D2 peak intensities that constitutes below $25 \, \%$ in the cladding-portion, and a significant fraction is at the center of the fiber core (presence of GeO_2 content) whereas we also detect that an abundant defect sites reside in the core–cladding interface, figure 5.2.5(c). Quite the same way, Goutaland et al. have devoted to the same arguments on D1 and D2 that are concentrated at the interface based on luminescence study of defects in silica based optical fibers. This is further supported from a study of defects control in optical fiber using Cathodoluminescence by Atkins et al. We have mentioned indeed above, that inner core–cladding portion of the fiber has an important role in overall changes of glass fiber under annealing and therefore an additional subsequent investigation in this line is required for better

understanding [98].

Now, the focus is on the intensity monitoring, beyond–Raman–wavenumber–range, as a function of temperature before we present the fitting of luminescence spectra (for fiber samples with and without FBG i.e., PS1250/1500, SMF28, GF1B) using Gaussian functions and then a PL–derived thermally activated process, that is provided in sub–section 5.3. Figure 5.2.6 shows a photograph of a strong red luminescence along a 15 –mm FBG segment (visible to the naked eye) and a faint emission integrated along 3 m of pristine fiber length (too weak to be perceived) in the uncoated area beside the FBG as the blue laser (473 nm) is coupled into the fiber.
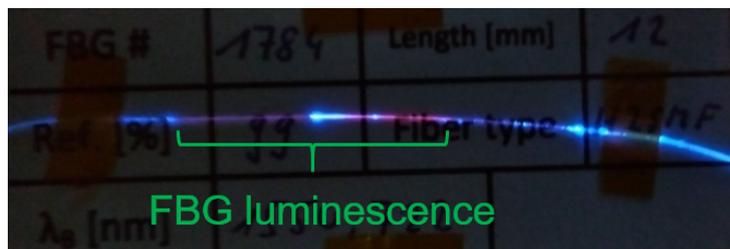
Figure 5.2.6: A strong luminescence of about 15 mm length can be observed at the location of the FBG. Additional but less intense red PL can be observed all over the uncoated area [97].

(ii) PS1250/1500 Fiber
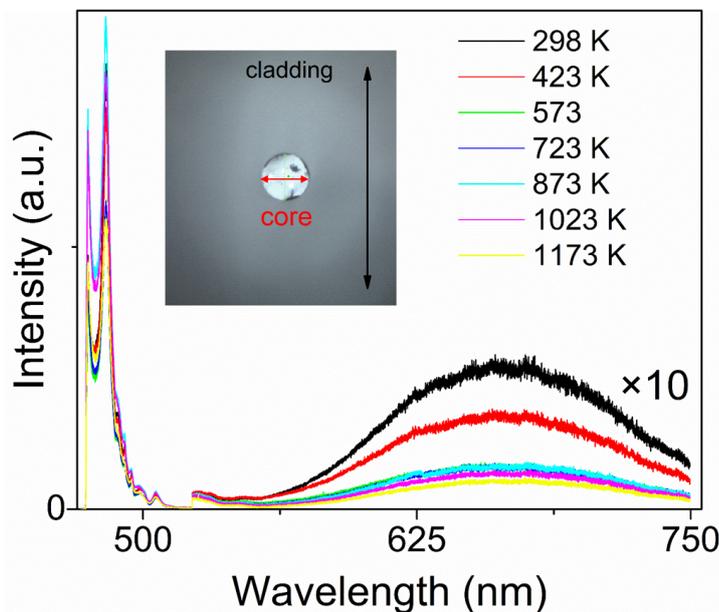
Figure 5.2.7: Raman and emission spectrum of a pristine PS1250/1500 fiber studied between ambient and 900 °C upon excitation by 473 nm light in the core. The inset shows the microscope image of the fiber cross-section with a core and the surrounding cladding [97].

Figure 5.2.7 shows the room temperature (300 K) spectrum of a pristine fiber of type PS1250/1500 with a maximum emission near 650 nm. The inset in figure 5.2.7 shows the cross–section profile of the cleaved fiber–end taken with the microscope.

(iii) SMF Fiber

The measurements of the SMF–28 fiber samples were done with acquisition times of 5 s, 2 accumulations of the signal and a high resolution grating with 2400 *grooves*/mm. For the regeneration process, the fibers were heated up to 950°C in steps of 150 K and subsequently cooled back to room temperature in the same step size (heating and cooling rate of approx. 10 K/ min). After finishing the first cycle, the measurement was repeated with the same fiber and parameters to clarify reversible and irreversible processes in the fiber. The spectra were then normalized to the main peak at 430 cm^{-1} after background subtraction, as described in the literature [99]. The first measurement for the SMF-28 fiber is shown in figure 5.2.8.
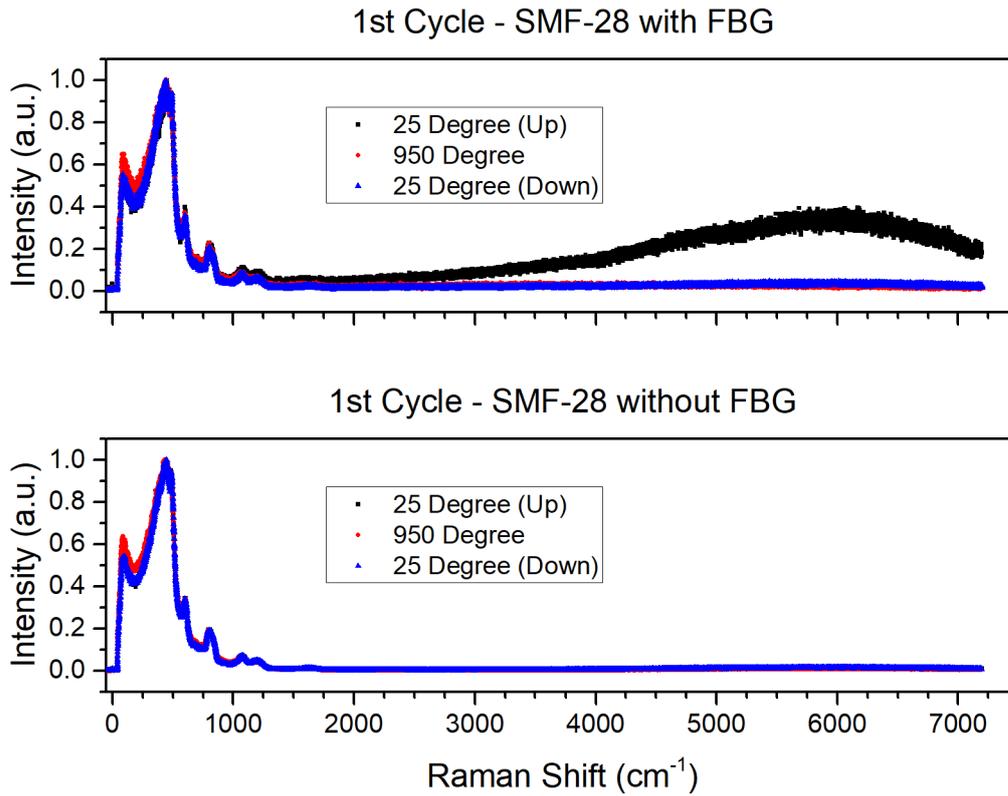
Figure 5.2.8: 1st regeneration cycle of the SMF–28 fiber. The upper graph displays the signal for the fiber containing an FBG. Here, the black curve is the initial spectrum at room temperature, the red curve is the spectrum at the regeneration temperature ($950\,°C$) and the blue curve is the final spectrum back to room temperature. At the beginning, a substantial photoluminescence is observable which vanishes during regeneration. The bottom graph shows the regeneration of a bare fiber without FBG. The curve colors and temperatures are the same as for the top graph. Here, no photoluminescence was observable.

In the upper graph of figure 5.2.8, almost no change in the Raman region ($<2000\,\mathrm{cm}^{-1}$) is observable. Thus, the fitting of the peaks is very inaccurate and the errors are bigger than the changes of the peaks. Hence, no confident statement can be made about the behavior of single peaks or group of peaks in the Raman signal. In addition to the Raman signal, photoluminescence (PL) ($>2000\,\mathrm{cm}^{-1}$) can be observed in the fiber containing the FBG which is irreversibly erased after the regeneration process. Contrary to the observations of the fiber with FBG, the fiber without FBG shows no photoluminescence (figure 5.2.8, bottom graph).

After the first regeneration cycle, the regeneration process was repeated with the same parameters. The results of the second heating cycle are depicted in figure 5.2.9.
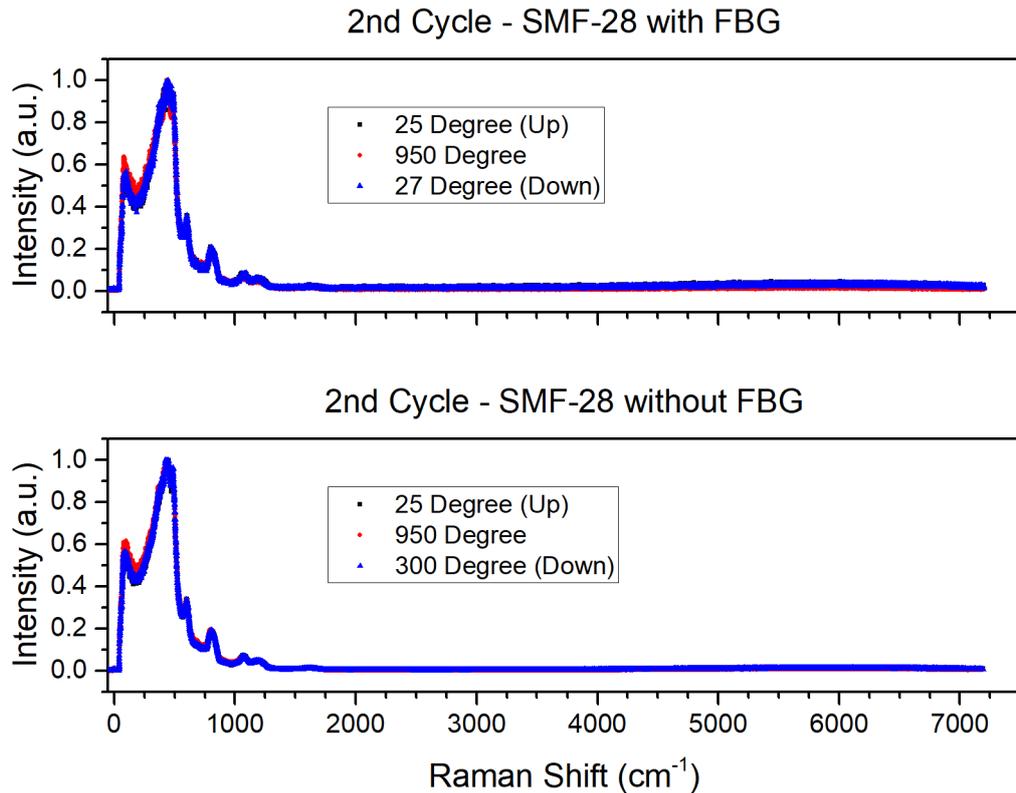
Figure 5.2.9: 2nd regeneration cycle of the SMF–28 fiber. The upper graph displays the signal for the fiber containing a FBG. Here, the black curve is the initial spectrum at room temperature, the red curve is the spectrum at the regeneration temperature (950 °C) and the blue curve is the final spectrum back at room temperature. The bottom graph shows the regeneration of a bare fiber without FBG. The curve colors and temperatures are the same as for the top graph.

The upper graph in figure 5.2.9 indicates, that the ongoing process for the PL is irrevesible since it does not occur again. Thus, the process might be related to hydrogen and hydrogen bonds in the fiber which are ruptured during the heating process. The fiber without FBG (figure 5.2.9, bottom graph) shows no significant changes. In additon, the last value under cooling is at 300 °C and not at room temperature (25 °C).

(iv) GF1B Fiber

For the measurement of the GF1B regeneration process, the fiber was placed in the setup as described above. The measurement of the GF1B fiber samples was done with the same acquisition parameters as for the SMF–28 fiber. For the regeneration process, the fibers were heated up to 950 °C in steps of 150 K and subsequently cooled back to room temperature in the same step size (heating and cooling rate of

approx. $10\,\mathrm{K/min}$). After finishing the first cycle, the measurement was repeated with the same fiber and parameters to clarify reversible and irreversible processes in the fiber. After measuring, the spectra were again normalized to the main peak at $430\,\mathrm{cm^{-1}}$. The first regeneration cycle for the GF1B fiber is shown in figure 5.2.10.
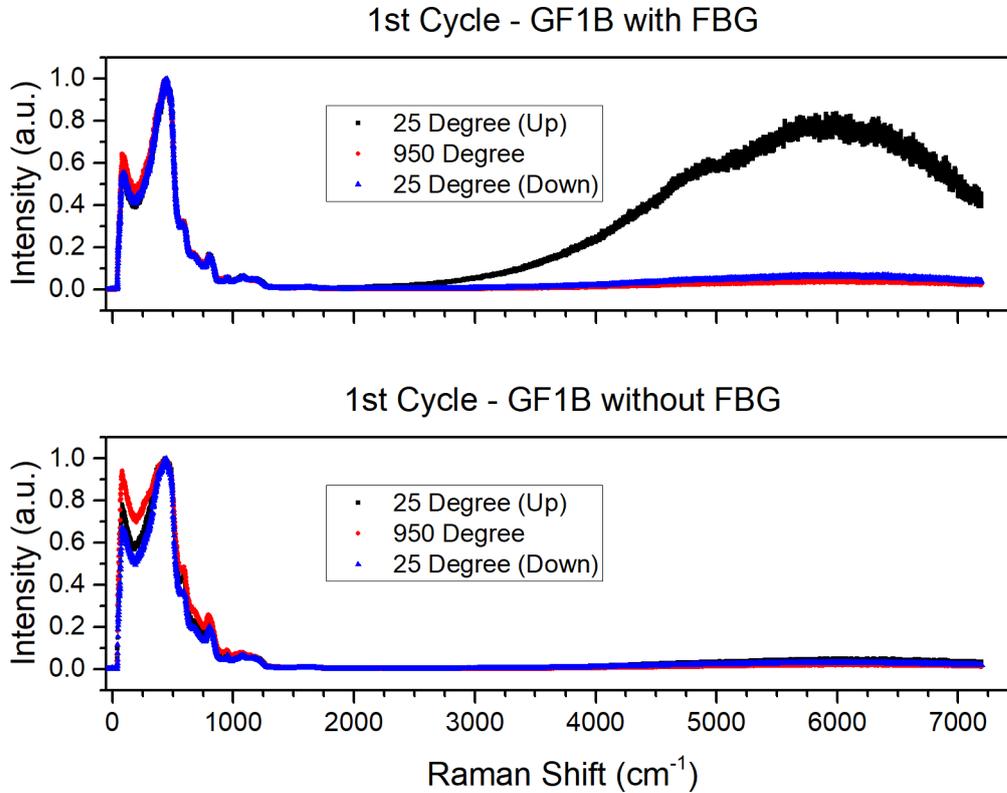
Figure 5.2.10: 1st regeneration cycle of the GF1B fiber. The top graph shows the signals for the fiber containing a FBG whereas the bottom graph shows the signals for the fiber without FBG. The colors are the same for both graphs and indicate room temperature at beginning (black), regeneration temperature (red) and room temperature at the end (blue). However, the top graph shows a photoluminescence for the fiber containing an FBG at the beginning which decreases during regeneration whereas the bare fiber in the bottom graph show subtle photoluminescence.

As figure 5.2.10 indicates, photoluminescence occurs also in the GF1B fiber only subtle as compared to the fiber with FBG. As for the SMF–28 fiber, the PL vanishes during the regeneration process and is completly erased after the cooling. For clarification, the results of the second regeneration cycle are shown in figure 5.2.11.
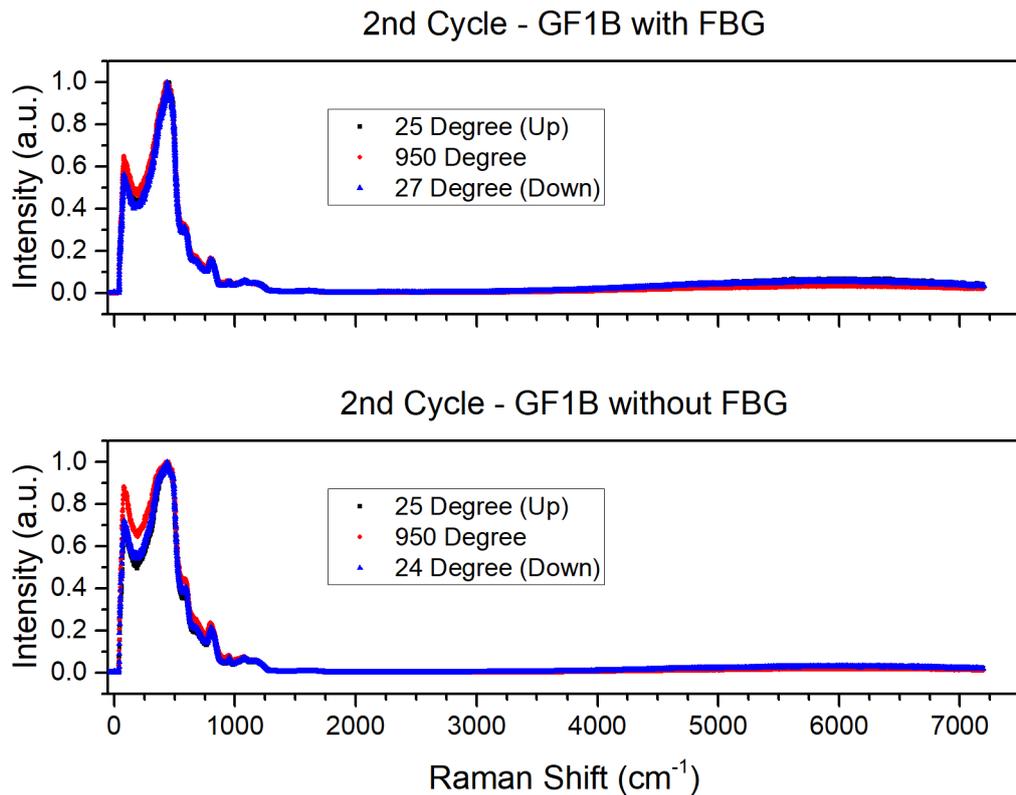
Figure 5.2.11: 2nd regeneration cycle of the GF1B fiber. The top graph shows the 2nd cycle of the fiber containing a FBG. Here, photoluminescence was not observable anymore. For comparison, the bottom graph shows the 2nd regeneration cycle of the bare fiber. The colors are the same for both graphs and indicate room temperature at beginning (black), regeneration temperature (red) and room temperature at the end (blue).

Figure 5.2.11 shows an irreversible thermal process in fibers containting a FBG. Furthermore, it can be seen that a new peak is observable in the spectra of the GF1B fiber (around $950\,\mathrm{cm}^{-1}$) which was not present in the SMF–28 fiber.

Comparative analysis of photosensitive fibers

By comparing a fiber with known composition to a fiber with unknown composition, possible dopants can be identified. For this, the spectrum of the known fiber is divided by the spectrum of the unknown fiber. As a result, a horizontal line at 1 (in the ordinate) should occur if there are no differences and anything different than 1 indicates deviations from the standard fiber. These deviations can be compared with values obtained from literature to gain informations about the unknown fiber. Figure 5.2.12 shows the difference between a standard telecom fiber (SMF–28) [95] which is only germania doped and a photosensitive GF1B fiber (dopants unknown) [100].
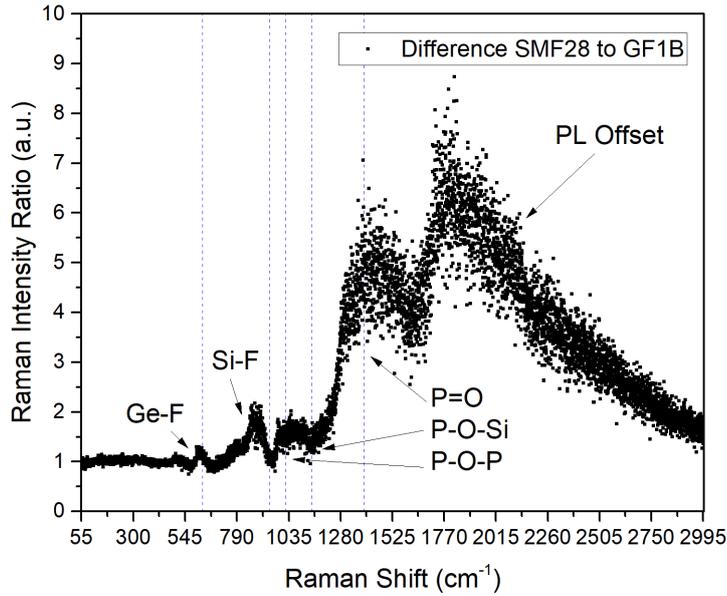
Figure 5.2.12: Ratio between the standard SMF–28 fiber and the photosensitive GF1B fiber. The dotted vertical blue lines depict the Raman shift for each component taken from literature: Ge-F at $628\,\mathrm{cm^{-1}}$ [101], Si–F at $945\,\mathrm{cm^{-1}}$ [40], [34], P-O-Si at $1020\,\mathrm{cm^{-1}}$ and P–O–P at $1200\,\mathrm{cm^{-1}}$ [102] and P=O at $1390\,\mathrm{cm^{-1}}$ [103]. The differences at higher wavenumbers ($\approx 1770\,\mathrm{cm^{-1}}$) are due to the different offsets of the photoluminescence (refer section 5.3 for photoluminescence).

In figure 5.2.12, black arrows indicate the fiber compositions known from literature (literature value located by the blue vertical dotted lines). Here, the peaks at $630\,\mathrm{cm^{-1}}$ and $945\,\mathrm{cm^{-1}}$ are assigned to the fluorine doping. The peaks at $1020\,\mathrm{cm^{-1}}$ and $1200\,\mathrm{cm^{-1}}$ are stretching modes from the P-O-P and P-O-Si. The peak around $1390\,\mathrm{cm^{-1}}$ is assigned to a double bond of one Phosphorus (P=O) surrounded by 4 oxygen atoms (3 normal bonds and one double bond) similar to SiO_4 tetrahedra. Despite all of the small peaks, a big peak with a decaying side slope at $1770\,\mathrm{cm^{-1}}$ can be seen. This peak originate from the photoluminescence (see section 5.3) which is much stronger in the GF1B fiber than in the SMF-28 fiber. However, some peaks differ from the literature value which comes partly from calibration (uncertainty of approx. $\pm 2\,\mathrm{cm^{-1}}$) which gives a slightly different x-axis for each fiber hence the division of both spectra is not at the same x values (the average of both wavenumbers was taken for plotting). Another influence comes from internal stresses, e.g. caused by the inner cladding of the GF1B fiber [104], since the literature values are for bulk materials with different fictive temperatures (fluorine doped silica glasses [40], [34], $P_2O_5 - SiO_2$ glass [102], [103]) and gas (Ge-F stretching mode can be expected between $(600 - 700)\,\mathrm{cm^{-1}}$ [101]), respectively. Lastly, in [102] it was stated that the

obtained values can differ much with the used production method as well as with the dopant concentration of the glass. Since the photosensitive GF1B fiber contains only fluorine and phosphorus, the main reason for the increased photosensitivity must be a higher content of germania since the phosphorus is supposed to be only in the inner cladding and not in the core (the measured phosphorus peaks are from the core/cladding interface). Hence, the phosporus should not affect the refractive index in the core region during inscription. Although fluorine does not contribute to the photosensitivity, it encourages structural relaxation which is already known to be a significant effect for RI changes in doped glasses by UV irradiation [105]. Nevertheless, the results provide a better understanding of the used photonsensitive fiber and its dopants which can play a major role in the effect of double regeneration [104].

In addition to the identification of dopants, the dopant concentration can be estimated by using the linear relationship found by Awazu et al. [91]. For this, the intensities of the $800 \, \text{cm}^{-1}$ and $945 \, \text{cm}^{-1}$ peaks (figure 5.2.10) are used to estimate the doping concentration.
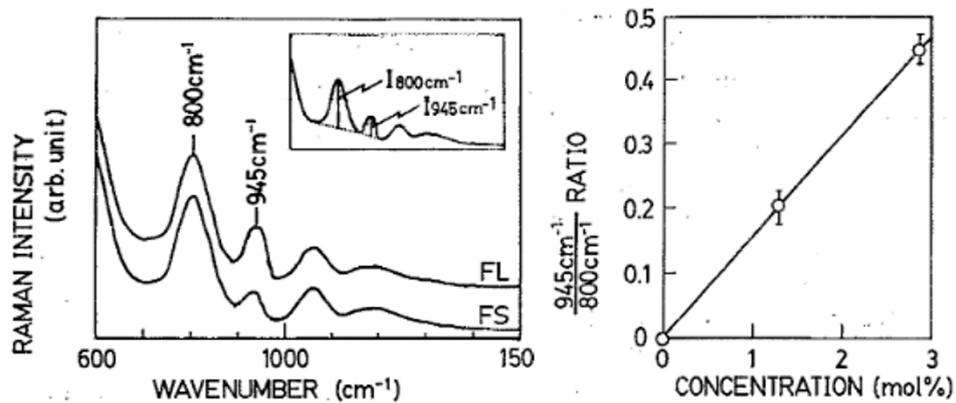
Figure 5.2.13: Left: Section of a Raman spectra for fluorine doped glasses with different fluorine concentrations (FL= $2.8 \, mole\%$ and FS= $1.3 \, mole\%$). The peak around $945 \, \text{cm}^{-1}$ is related to the Si-F bond. Right: Correlation of the intensity ratio to the doping concentration [91].

From the obtained intensities of 0.164 at $800 \, \text{cm}^{-1}$ band and 0.05 at $945 \, \text{cm}^{-1}$ band, intensity ratio of ≈ 0.3 is calculated. By comparing this value to the linear correlation found by Awazu et al., a fluorine doping concentration of $\approx 2 \, \text{mol}\%$ can be determined.

5.3 Photoluminescence measurements

The very first attempt to *ex–situ* PL measurements of RFBGs was undertaken by our group, Barba et al. [1]. The PL of the fiber along the excitation path perpendicular to the fiber is spatially mapped to monitor the PL from defect centers inside core and outer cladding parts of FBG. Two wavelengths, 355 nm and 532 nm, are used for excitation and focused 45 µm under the fibers surface. Figure 5.3.1 shows the PL of the Ge–doped fiber excited by 355 nm.
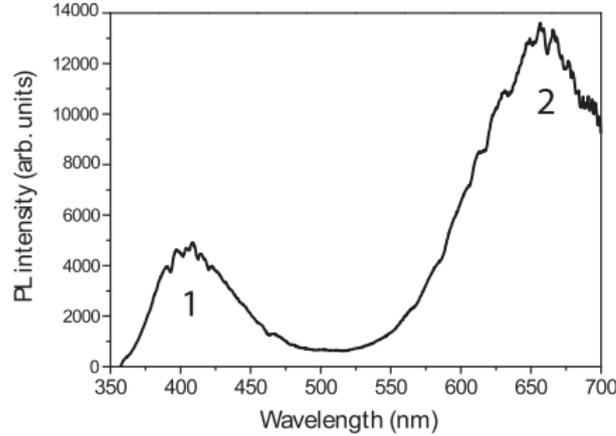
Figure 5.3.1: PL of a Ge–doped fiber excitated with 355 nm. Two PL peaks are observable after excitation. (1) at ≈ 450 nm belongs to ODC and (2) at ≈ 650 nm belongs to NBOHC [1].

The scanning achieved diagonally over the fiber while capturing the PL with a resolution of 546 nm and 361 nm, respectively. Afterwards, the scans is used to produce an intensity PL map, figure 5.3.2.
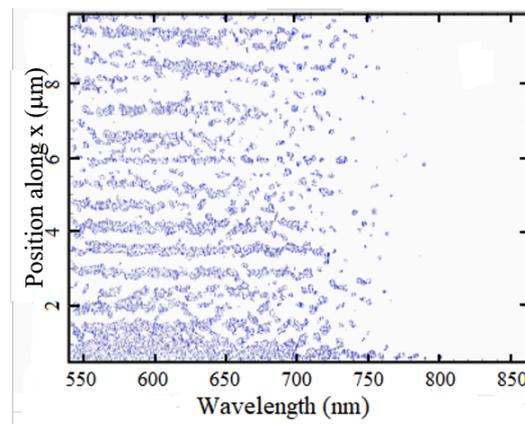
Figure 5.3.2: Spatial itensity PL map of the 650 nm peak. One can see the spatial periodicity of the NBOHC which equals the grating period of $\Lambda \approx$ 0.5 µm [1].

Here, a spatial periodicity of the 650 nm peak (NBOHC) is observable which cor-

responds to the grating period of $\Lambda \approx 0.5\,\mu m$. This PL is directly related to the generation of NBOHC during the inscription process. Then, investigation of the the influence of hydrogen on the PL of FBGs [28] were performed. Hereby, the observation of a remarkable *ex–situ* decay of the PL is highlighted after the regeneration process (heating to 775°C) of FBGs written in deuterium loaded photosensitive fibers. The decrease of PL and the measurement setup are depicted in figure 5.3.3.
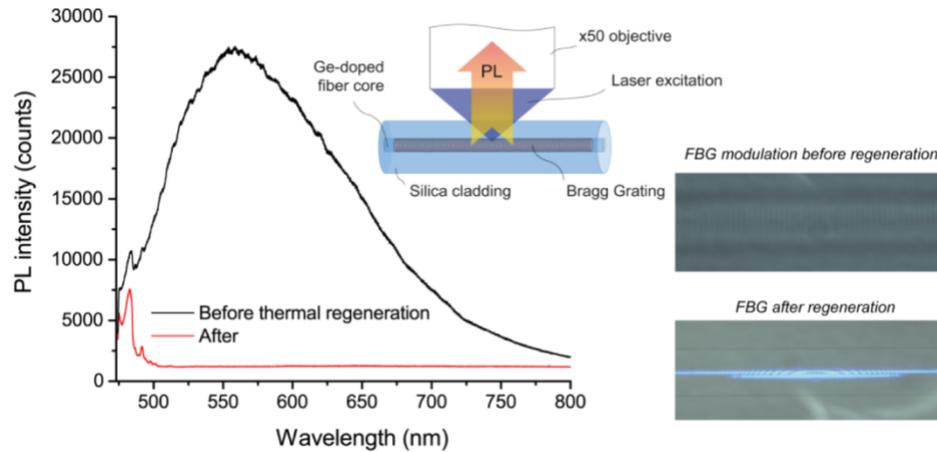
Figure 5.3.3: Left: Decrease of the PL around 550 nm after thermal regeneration. Top: Measurement setup for the PL measurements. Right: Light scattering out of the fiber before and after regeneration [28].

The conclusion is that the decrease of the PL in the fiber is due to diffusion processes of oxygens defects leading to a densification. However, the PL in figure 5.3.3 is different than the one observed by Barba et al. (peak at 650 nm instead of 550 nm, refer figure 5.3.1). A possible reason for the difference might be species related to deuterium which was used prior inscription and heat threatment. Nevertheless, PL measurements by Goutaland have shown that hydrogen loading can lead to PL 650 nm, too [54]. Therefore, the difference is mostly due to the deuterium loading. Differences in the Raman spectrum of hydrogen and deuterium loaded fibers were measured by Cordier et al. [96].

In–situ PL measurement

The next attempt is to switch from *ex–situ* to *in–situ* as the previous measurements of the regeneration process (from section 5.2) have shown qualitative and quantitative temperature behavior of the photoluminescence, it is further investigated in this section. For further PL analysis of the obtained results, one way is to integrate the PL band and other is fitting the band to extract the meaningful parameters both of these are discussed below.

(i) Integrating spectral PL band

For this, the area of the PL ($> 1800\,\mathrm{cm}^{-1}$) is integrated (to ensure a decreasing intensity does not result in a large FWHM) and depicted over temperature. For comparison, the normalized spectra from the regeneration process is used.

SMF Fiber

First, the PL for the SMF–28 fiber was evaluated with the plot as shown in figure 5.3.4.
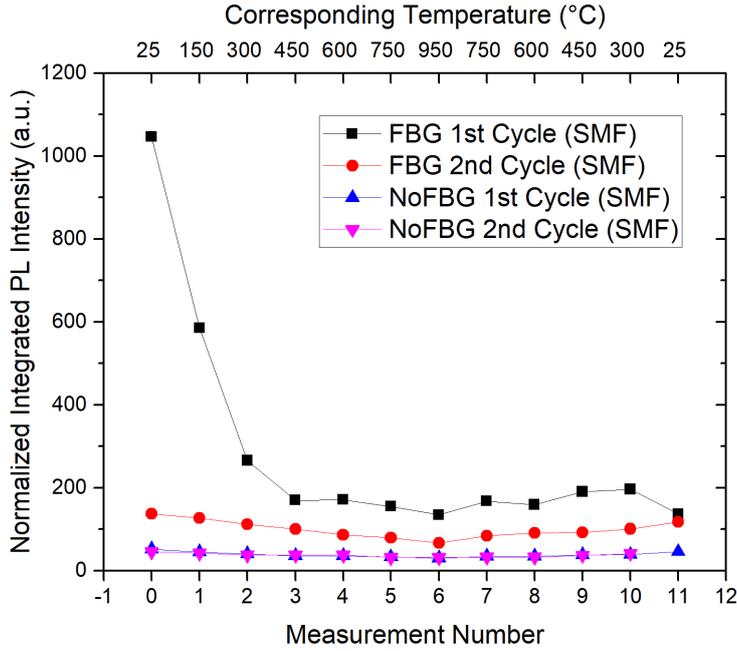
Figure 5.3.4: The SMF28 fiber with the seed gratings (black and red curves) show PL whereas the fiber without an FBGs (blue and purple curves) show subtle or no PL. Further, the seed grating decays with increasing temperature during the first heating cycle and reaches a stable value after approx. $450\,^{\circ}\mathrm{C}$ (same value as at the start/end of the second cycle). The decay of the seed grating occurs only during the first heating and not during the second cycle (red curve, same starting and end values).

The decay of the PL starts during the heating process of the first cycle and reaches its minimum at 450°C as figure 5.3.4 indicates. However, the second cycle FBG shows a lower PL than during the heating process of the first cycle. In general, the PL seems to be higher for the fiber containing an FBG than for bare fibers. As the data indicates, the PL may come from a inscription and/or hydrogen related defect and thus no PL is observable in bare fibers.

GF1B Fiber

Second, similar to the analysis of the SMF–28 fiber the PL of the normalized GF1B spectra was integrated and plotted over temperature (figure 5.3.5). In addition, a non–hydrogen loaded fiber containing an FBG was also measured.
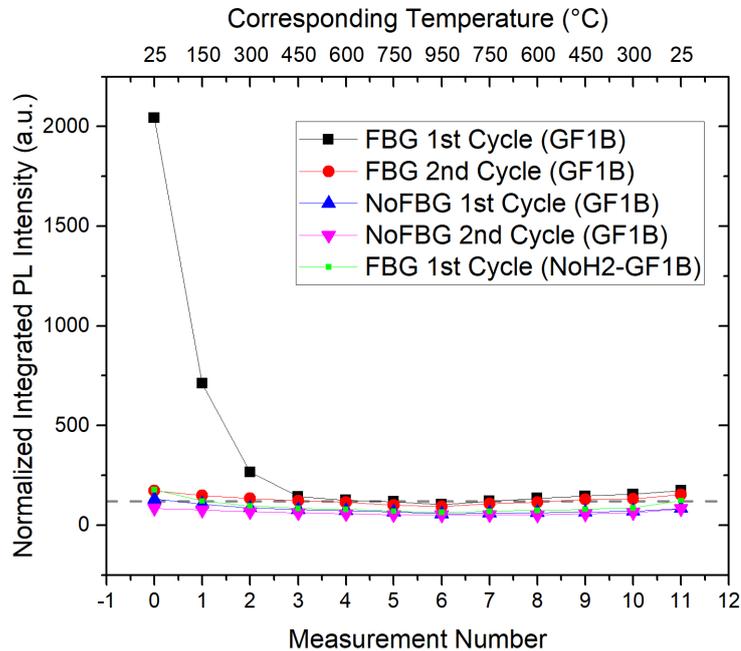
Figure 5.3.5: The GF1B fiber with the seed gratings (black and red curves) show PL whereas the fiber without FBGs (blue and purple curves) show no PL and the FBG in a non–hydrogen loaded fiber (green curve) shows less PL. Further, the seed grating in the hydrogen loaded fiber decays with increasing temperature during the first heating cycle and reaches a stable value after approx. 450 °C (same value as at the start and end of the second cycle) whereas the FBG in the non–hydrogen loaded fibers decays earlier and reaches the stable value after approx. 150 °C (see grey dashed line). The decay of the seed grating occurs only during the first heating and not during the second cycle (red curve, same starting and end values).

Figure 5.3.5 shows as similar behavior as for the SMF–28 fiber with decreasing PL intensity which is also erased around 450 °C. In addition, the non–hydrogen loaded fiber with FBG shows insignificantly higher PL than the bare fibers which vanishes around 150°C, see figure 5.3.6.
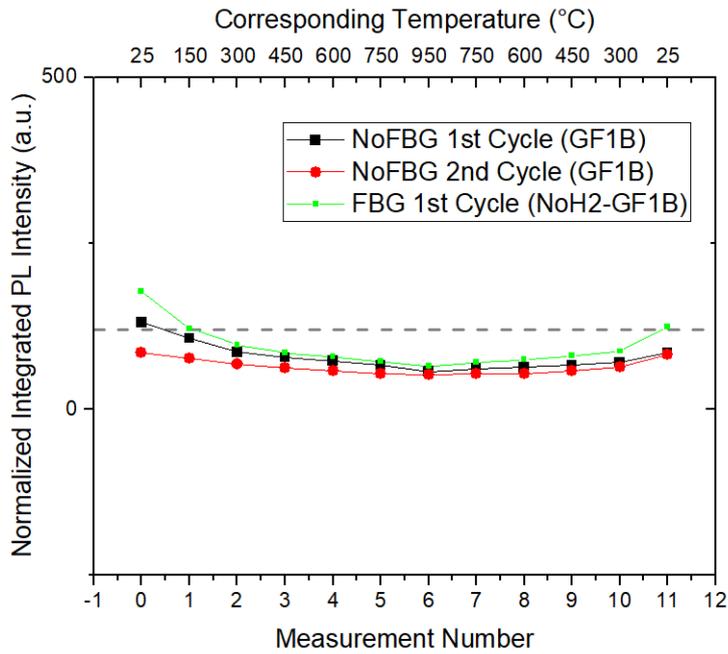
Figure 5.3.6: A non–hydrogen loaded FBG in a GF1B fiber (green line) shows a small amount of PL (compared to bare fibers). With increasing temperature the PL of the FBG decays and is fully erased around 150 °C.

The effect of PL in non–hydrogen loaded FBGs and bare fibers is mainly due to NBOHC which are present in bare fibers as well as the generation of NBOHC during type I inscription. However, also for the GF1B fiber, the PL intensities for fibers with FBG are higher than for the fibers without FBG.

(ii) Gaussian fit of the PL band and procedure for thermal activation extraction

As shown in the figure 5.3.7, the shape of the red emission band on the wavenumber regime above $2000\,\mathrm{cm^{-1}}$ (upper panel) is fitted with a single Gaussian curve (middle panel) where the residuals (lower panel) indicate that there is single emission peak in this spectral range.
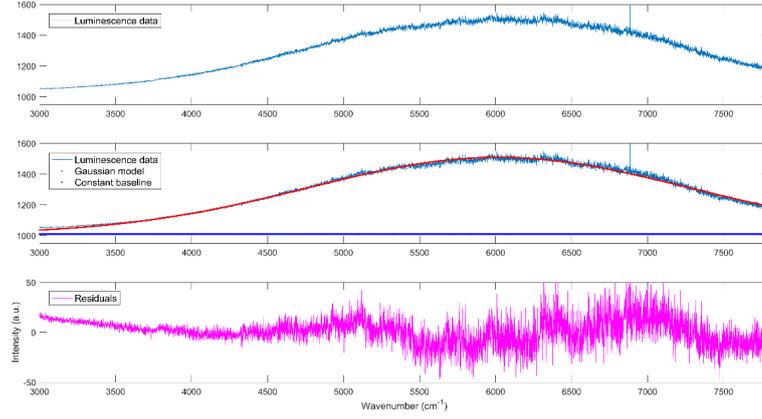
Figure 5.3.7: Spectral shape of the emission band (upper panel) fitted to a single Gaussian curve (middle panel) showing the fit residual (lower panel) [97].

The Gaussian fit results are used to extract the PL band intensity variation at each temperature step. The thermally activated processes are then investigated for the identification of activation energy values. However, given the limits on the time resolution for different heating rate, photoluminescence spectra are not acquired as a continuous heating, but in steps of 20 minutes dwell time between each heating rate thus only the qualitative extraction of the activation results are possible from the derived results. To begin the analysis of the temperature-dependent luminescence, we plot the natural logarithm of intensity, $\ln[\left(\frac{I_0}{I}-1\right)]$, against the reciprocal of absolute temperature ($\frac{1}{T}$). Here, I_0 and I represent the PL intensity at ambient and other temperature, respectively. For this, a common expression (given in equation 5.1) related to the diffusion and complex chemical kinetics in the logarithmic form can be found elsewhere [97].

$$\ln(\frac{I_0}{I}-1) = -\frac{E_a}{k_B} \cdot \frac{1}{T} + \ln(A) \tag{5.1}$$

where $\ln A$ is a constant, k_{B} is the Boltzmann's constant and E_{a} expresses the activation energy [1]. Using equation 5.1, the activation energies (E_{a}) are extracted from the linear fits of the Arrhenius plots in three fibers and FBGs (for measurements between $25-950°C$). The uncertainty in the slope obtained from the linear regression is between $3-15$ percent.

---

[1]The values labelled $'E_a'$ in the figures below are no activation energies in the common sense as they also reflect the heating rate towards the final temperature.
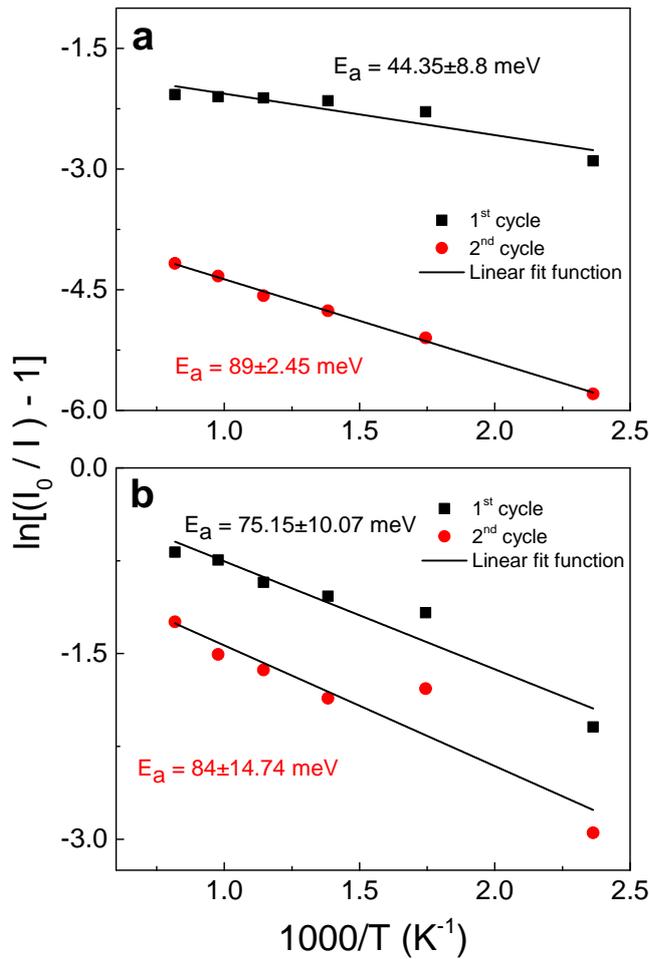
Figure 5.3.8: Arrhenius plot of PL intensity between ambient and 950 °C for (a) grating in SMF28 fiber and (b) SMF28 pristine fiber [97].

The high $GeO_2 \cdot F$-doping in GF1B is ascribed to higher activation energies observed in GF1B compared to SMF28 with FBGs (Figures 5.3.8(a) and 5.3.9(a)) and unperturbed ones (Figures 5.3.8(b) and 5.3.9(b)) for same annealing cycle and fiber types. It is suggested that the enhancement of activation energy is mainly due to fluorine doping, indicating that fluorine related reactions can be deliberately enhanced or suppressed upon annealing as proposed by Itoh et al [97].
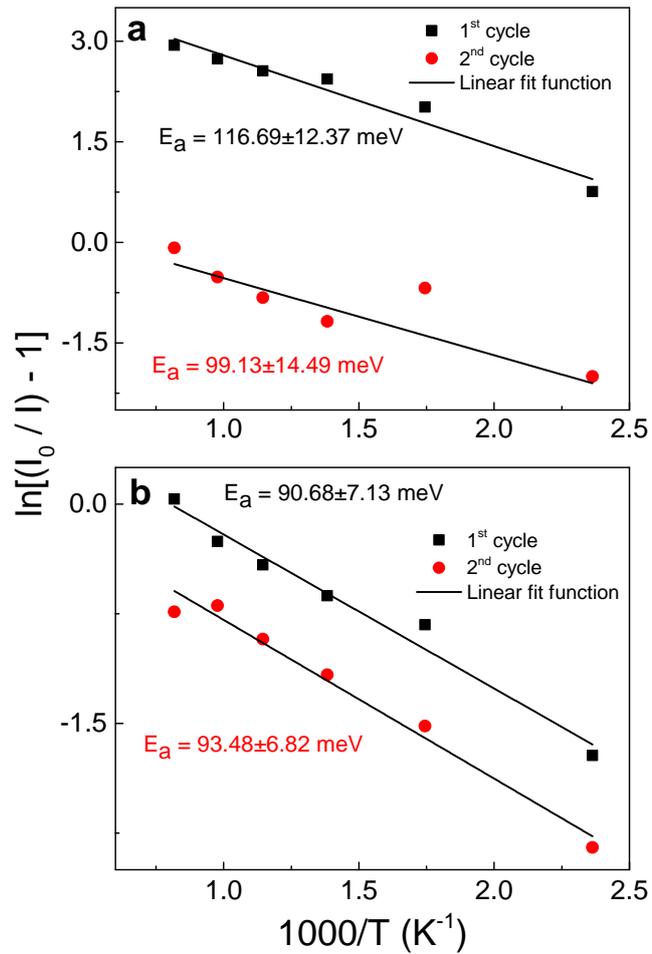
Figure 5.3.9: Arrhenius plot of PL intensity between ambient and 950 °C (repeated cycles) for (a) grating in GF1B fiber and (b) GF1B pristine fiber [97].

Likewise, Figure 5.3.10 displays the Arrhenius linearization of PL intensity under two subsequent thermal cycles in PS1250/1500 pristine fiber. This fiber type shows the highest activation energy among the investigated fibers with ∼145 meV. The temperature dependence of the activation process in fibers containing FBGs, Figures 5.3.8(a) and 5.3.9(a), stand in contrast to the one encountered in pristine fibers, Figures 5.3.8(b), 5.3.9(b) and 5.3.10.
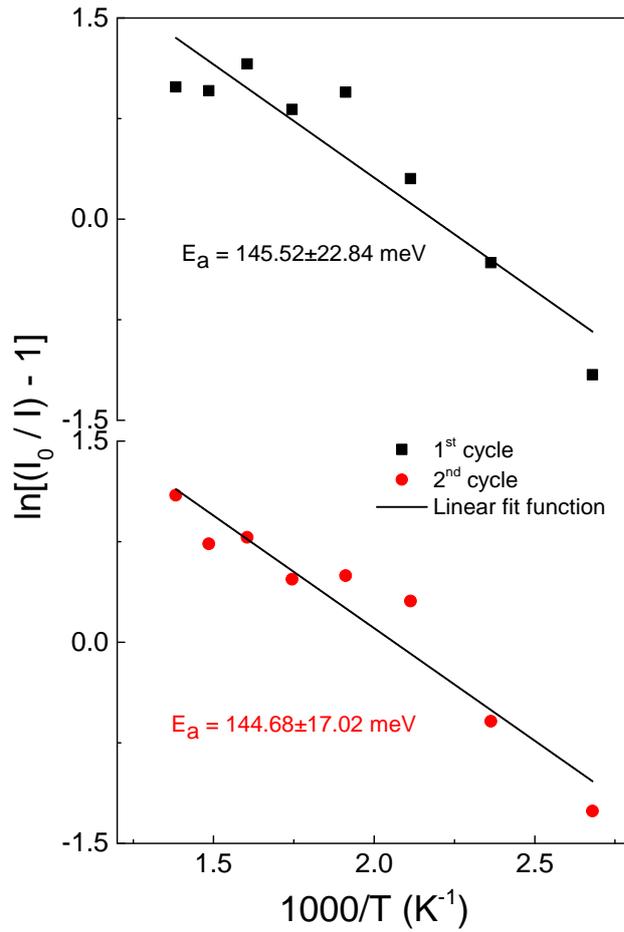
Figure 5.3.10: Arrhenius plot of PL intensity between ambient and 950 °C (repeated cycles) for PS1250/1500 pristine fiber [97].

In Figures 5.3.8(b) and 5.3.9(b), a slightly different activation energy was observed for the SMF28 and GF1B pristine fibers. These differences might be caused by different core dopants (e.g. fluorine in GF1B) and can be associated to intrinsic glass features as for example NBOHC.

The higher activation energy in PS1250/1500 could be attributed to the high content of $GeO_2 \cdot B_2O_3$-doping. The second annealing cycles in SMF28-FBG and GF1B-FBG show similar activation energies, which is in accordance with the values obtained for the pristine fibers. However, the first cycle of the fibers containing FBGs systematically shows a lower activation energy. This indicates that the temperature-dependent changes in FBGs occur mostly during the first thermal cycle unlike in pristine fiber. The interpretation is that the larger activation energy of the first cycle of FBGs is mostly due to hydrogen-associated defects.

Discussion

Fluorine as a core dopant with a concentration of $\approx 2\,\mathrm{mol}\%$ and phosphorus were identified, the later could be diffusion related from the inner cladding. Fluorine can enhance the structural relaxation in glasses as shown by Shimodaira et al. and Saito et al. [40], [34]. Since the used photosensitive fiber contains an inner cladding, the effect of relaxation could be much stronger than for glasses as observed by Polz et al. [104].

Most important is the temperature behavior of the PL. The temperature dependence of the PL in germania doped silica fibers was not measured before. Although there are no reported absorption bands around $2.62\,\mathrm{eV}^2$, PL was observable. The reason for the PL around $2\,\mathrm{eV}$ is heavily discussed in literature (see section 3.6), even though NBOHC are the most favoured reason in the literature. Despite the NBOHC, there are a few different suggestions for the absorption:

(i) Ge-H: Goutaland et al. proposed several reactions for the origin of the $2\,\mathrm{eV}$ PL. Their most favoured solution was the generation of Ge-H from a reaction involving NBOHC, GeE′ and hydrogen. As a result of this reaction, Ge-H and Si-OH is generated, see equation 5.2 [54].

$$\equiv \mathrm{Ge}^{\bullet} + {}^{-}\mathrm{O} - \mathrm{Si} \equiv\, + \mathrm{H}_2 \longrightarrow\, \equiv \mathrm{Ge} - \mathrm{H} +\, \equiv \mathrm{Si} - \mathrm{OH} \tag{5.2}$$

Both, GeE′ and Si-OH are known to be generated during the FBG inscription process and both contribute to the refractive index change in the fiber while NBOHC are intrinsically available in the fiber [106]. However, this alone would not explain the PL in the non–hydrogen loaded fiber as it was observed (figure 5.3.5).

(ii) GeX: The origin of an unknown effect with absorption at $2.64\,\mathrm{eV}$ was proposed by Neustruev in 1994 [45]. In his work he investigated different color centres in glasses including hydrogen related effects. Hereby, he discovered a new absorption band at $2.61\,\mathrm{eV}$ which he named GeX defect. He further stated that the GeX effect only occurs after exposure to UV ($> 5\,\mathrm{eV}$) or γ-irradiation with Ge(1) as the precursor. He also observed temperature stability until $150\,\mathrm{°C}$ with subsequently decreasing intensity of the PL and in additon photobleaching with blue lasers which we did not observe.

(iii) Germyl: In 1993, Awazu et al. proposed a model based on a germyl radical which is responsible for the red luminescence around $650\,\mathrm{nm}$ [107]. In addition, they

---

^{2}Energy of the used excitation wavelength of $473\,\mathrm{nm}$.

showed a dependency of the strength of the PL based on hydrogen loading and γ-irradiation. In their theory, a GLPC (which is created during hydrogen inscription) reacts with a hydrogen atom to form a germyl radical as equation 5.3 illustrates.

$$=\mathrm{Ge}\colon + \ \mathrm{H} \longrightarrow =\mathrm{Ge}^{\bullet} - \mathrm{H} \qquad (5.3)$$

Additionally to their theory, they specified the thermal stability of this compound to 200°C. Nevertheless, the GLPCs have an apsorption band of 5.14 eV and thus would require a two photon process. The proposed reaction would require free hydrogen atoms within the fiber since the PL occurs during the formation of the germyl radical out of the relaxation of an excited GLPC. Contrary to the work of Awazu et al., Poulios et al. confirmed the existence of germyl too but as a single photon process at 370 nm with a dependency on the initial GODC concentration in the glass [108]. In addition, he observed the PL only in fibers which were loaded with hydrogen prior to X-ray irradiation.

(iv) Ge-Nanocrystals: A lot of theories suggest Ge-nanocrystals and their precursors as the reason behind the 2 eV PL in Ge-doped glasses [107, 109–111]. However, it is not clear how the nanocrystals are generated in hydrogen loaded fibers via UV exposure but it seems they have a temperature dependency as measured by Kawamura et al. of about 700°C. During heating the crystals and/or their precursors were oxidized and thus not emitting PL anymore. However, other possible reasons for the 2 eV PL can be found in literature as e.g. self trapped excitons [112].

Regarding thermally activated processes, we measure the temperature dependence and degradation dynamics of PL in the red spectral range as detected in transmission through the fiber core for excitation at 473 nm in three types of germanosilicate pristine fibers and in hydrogen loaded fibers with type–I gratings. The results are summarized as follows:

(i) Two types of luminescence were observed in this spectral range, one stable and intrinsic to the fiber, the other one as a consequence to the FBG and more volatile. As for the luminescence (of both FBG and pristine fibers), a Gaussian fit provided good agreement with experimental data. Both types of luminescence intensity obey an Arrhenius law, and can thus be characterized by thermally activated processes. The intrinsic luminescence is stable under repetitive heating cycles, thus based on a reversible process while the luminescence associated to the FBG luminescence in both 'SMF28, H_2-loaded' and 'GF1B double-clad, H_2-loaded' fibers almost completely disappeared at $\sim$ 600–650K. This significant attenuation with the increase of temperature is interpreted as hydrogen induced defect, since it is only present in

fibers that are hydrogen-loaded whereas the second cycle observations are attributed to the recombination of NBOHCs, generally arising from Si–O bonds breakage.

(ii) It is not very likely that the activation energies obtained in FBG samples are assigned to diffusion processes in the fiber. Values in literature state activation energies for hydrogen diffusion in the order of 400 meV and higher [113]. However, Revesz stated that the activation energy for the annealing of charge trapped at SiOH has an activation energy of around 300 meV which can be lowered by structural channels consisting of hydroxyl groups [114]. Since the inscription process periodically generates hydroxyl groups, this could be part of an explanation of the observed low values.

(iii) The photosensitivity depends on interlinked fiber parameters, many of which a susceptible to thermal, mechanical or even chemical treatment. The higher activation energy exhibited by pristine PS1250/1500 fiber compared to GF1B and SMF28 pristine fibers during the first cycle is associated to the influence of B_2O_3 co-doped photosensitivity, indicating different structural or chemical induced changes. The influence of co-dopants on the activation energy is further complemented through the observation of higher activation energies for hydroxyl formation in fluorine co-doped SiO_2–GeO_2 glass compared to undoped SiO_2–GeO_2 by Itoh et al. [115]. However, the formation energies of hydroxyl were reported to be 0.69 eV and 0.91 eV for SiO_2–GeO_2 and F-doped SiO_2–GeO_2, respectively.

6 Conclusions and Perspectives

This thesis sought to explore a number of questions raised by the temperature sensitive refractive index structure observed to exist in the core of a phase-mask-written UV-induced type I FBG. The investigations have shown the combined ease of optical technique shedding some light on the underlying materials physics and chemistry of the optical glass fiber materials that I will explain in the following paragraphs.

This thesis has addressed two main concerns regarding the mechanisms leading to a substantial loss of FBG reflectivity after recovery at elevated temperatures:

- Is it possible to optimize the FBGs operation by tailoring the regeneration process for temperature sensing at elevated temperatures and otherwise harsh environments?

Annealing behavior of gratings in standard telecom grade fibers were investigated with a dedicated setup that allowed for temperature cycles below $1000\,°C$. With the reflectivity and the peak width as observables, a competing gratings model demystifying the regeneration process was developed. As such, in terms of understanding about the annealing effect on regeneration of fiber Bragg gratings and from the analysis of time- and temperature-dependent sequence of spectra has shown that the higher the temperature the grating has seen during the thermal cycle, the less remains of it. In this work, the higher residual reflectivity ($\approx 85\,\%$) and long–term stability of FBGs being subjected to multi-step annealing up to a temperature of $1000\,°C$ was obtained. The refractive index structures and the spectral consequences of the observed refractive index structures as a function of temperature and time were investigated in chapters 2, 3 and 4.

- Is there a quantitative correlation of macroscopic observations such as regeneration and the refractive index contrast with microscopic features?

As a first step, the optical system was upgraded from an existing Raman spectrometer and the approach relying on spectroscopy along the fiber core was established. This takes an advantage of long interaction lengths compared to conventional microscopy approaches. And, on the other hand, it holds the experimental challenges

due to temperature drift of the fiber coupling that limits the time resolution for isothermal luminescence decay experiments. By exciting fibers (with and without FBG) at 473 nm and peak shift vs annealing temperature ranging from room temperature up to 1000 °C were investigated using a dedicated fitting procedure of extracting shifts (towards larger or smaller wavenumbers) and parameters under conditions exhibiting a decrease or increase of intensity. As well the thermal activation energies were monitored for the defect-related luminescence (collected at 650 nm) in different types of glass fibers with and without fiber Bragg gratings in hydrogen-loaded fibers, for example, analyzing qualitative data for two consecutive heating cycles confirmed two distinct activation energies. These are covered in chapters 3 and 5.

As an outlook, the set-up below would allow simultaneous in-line reflectivity and Raman spectra measurement of the glass structure upon FBG regeneration via reflectivity or even the correlation studies of luminescence decay and loss of refractive index modulation in the fiber core.
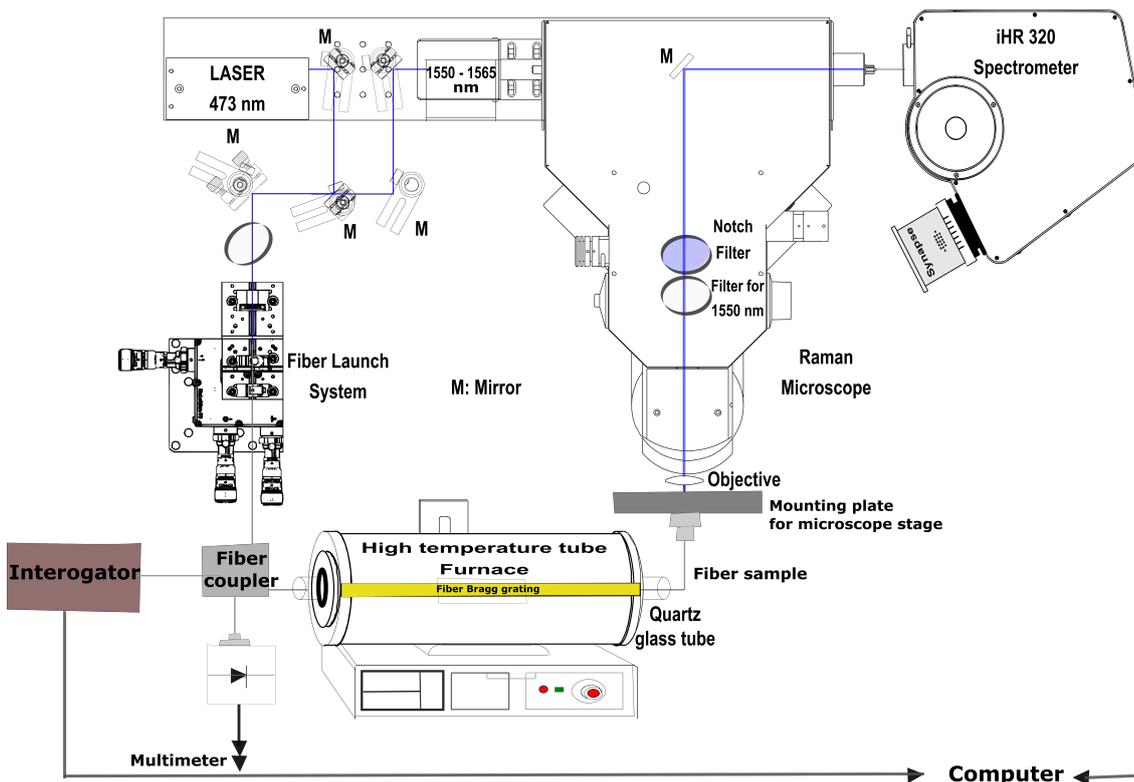
Figure 6.0.1: Improved measurement setup. A 90/10 fibercoupler allows simultaneous measurements of the Raman signal and the laser power. Additionally, the reflected power of the FBG and the Bragg wavelength during the Raman measurements can be measured by an interrogator system.

The above configuration allows not only the direct correlation of Raman and Bragg wavelength data for an interferometric changes of lengths in a fiber Bragg grat-

ing and Raman peak shifts under annealing conditions but many other directions that potentially can be explored concerning influence of FBG profile function upon regeneration, as in these examples:

(i) influence of diffraction orders other than the plus and minus first orders which disturb the FBG index distribution and

(ii) possible impact of undesired standing optical waves formation in the grating region.

7 Directories

List of Figures

List of Tables

Bibliography

[1] D. Barba, F. Martin, K. Tagziria, M. Nicklaus, E. Haddad, F. Rosei, and A. Ruediger, "Photoluminescence mapping of oxygen-defects emission for nanoscale spatial characterization of fiber Bragg gratings," *Journal of Applied Physics*, vol. 116, no. 6, pp. 064 906–1–064 906–5, Aug 2014.

[2] K. O. Hill and G. Meltz, "Fiber Bragg grating technology fundamentals and overview," *Journal of lightwave technology*, vol. 15, no. 8, pp. 1263–1276, 1997.

[3] R. Kashyap, *Fiber Bragg Gratings.* ACADEMIC PR INC, 2009.

[4] D. S. del Castillo (FIDAMC), "Monitorization with FBG sensors of thermoplastics materials manufacturing processes." [Online]. Available: http://fidamc.es/en-us/News/New-Detail/Article/94/ Monitorization-with-FBG-sensors-of-thermoplastics-materials-manufacturing-proce

[5] N. Theune, M. Muller, H. Hertsch, J. Kaiser, M. Willsch, P. Krammer, and T. Bosselmann, "Investigation of stator coil and lead temperatures on high voltage inside large power generators via use of fiber Bragg gratings," in *Proceedings of IEEE Sensors.* IEEE, 2002.

[6] I. Mckenzie and N. Karafolas, "Fiber optic sensing in space structures: the experience of the european space agency (invited paper)," in *17th International Conference on Optical Fibre Sensors.* SPIE, May 2005.

[7] S. R. K. Morikawa, C. S. Camerini, D. R. Pipa, J. M. C. Santos, G. P. Pires, A. M. B. Braga, R. W. A. Llerena, and A. S. Ribeiro, "Monitoring of flexible oil lines using FBG sensors," in *19th International Conference on Optical Fibre Sensors*, D. D. Sampson, Ed. SPIE, Apr 2008.

[8] M. Fokine, "Underlying mechanisms, applications, and limitations of chemical composition gratings in silica based fibers," *Journal of Non-Crystalline Solids*, vol. 349, pp. 98–104, Dec 2004.

[9] J. Canning, M. Stevenson, S. Bandyopadhyay, and K. Cook, "Extreme silica optical fibre gratings," *Sensors*, vol. 8, no. 10, pp. 6448–6452, Oct 2008.

[10] T. Erdogan, V. Mizrahi, P. J. Lemaire, and D. Monroe, "Decay of ultraviolet-induced fiber Bragg gratings," *Journal of Applied Physics*, vol. 76, no. 1, pp. 73–80, Jul 1994.

[11] M. Lancry, C. Depecker, B. Poumellec, and M. Douay, "H-bearing species migration during UV writing of Bragg gratings in germanosilicate optical fibers," *Journal of Non-Crystalline Solids*, vol. 353, no. 5-7, pp. 451–455, Apr 2007.

[12] M. Lancry, K. Cook, B. Poumellec, and J. Canning, "Investigation of structural glass relaxation in regenerated fiber Bragg gratings," in *Photonics and Fiber Technology 2016*, no. JT4A.27.   Optical Society of America, 2016.

[13] D. Grobnic, C. Hnatovsky, R. Lausten, and S. J. Mihailov, "Dynamics of the fluorescence intensity during fiber Bragg gratings inscription in SMF 28 and pure silica core fiber using 800 nm fs radiation," in *Photonics and Fiber Technology 2016*, no. BTh3B.7.   Optical Society of America, 2016.

[14] C. Hnatovsky, D. Grobnic, and S. J. Mihailov, "In situ monitoring of fiber Bragg grating evolution during femtosecond-laser inscription process," in *Photonics and Fiber Technology 2016*, no. BTh3B.2.   Optical Society of America, 2016.

[15] B. Bastola, D. Barba, M. Celikin, K. Tagziria, E. Haddad, F. Rosei, and A. Ruediger, "Temperature-dependent Raman spectroscopy studies of fibers," in *Photonics and Fiber Technology 2016*, no. JT4A.28.   Optical Society of America, 2016.

[16] B. Bastola, B. Fischer, J. Roths, and A. Ruediger, "In-situ Raman investigation of optical fiber glass structural changes at high temperature," in *Proceedings Volume 10208, Fiber Optic Sensors and Applications XIV*, no. 102080L. SPIE, 2017.

[17] A. Agarwal, K. M. Davis, and M. Tomozawa, "A simple ir spectroscopic method for determining fictive temperature of silica glasses," *Journal of Non-Crystalline Solids*, vol. 185, no. 1-2, pp. 191–198, 1995.

[18] F. Galeener and J. Mikkelsen, "Raman studies of the thermal oxide of silicon," *Solid State Communications*, vol. 37, no. 9, pp. 719–723, 1981.

[19] G. Scherer, "Relaxation in glass and composites," *Wiley New York*, 1986.

[20] P. Tandon, "Effect of stress on the structural relaxation behavior of glasses," *Journal of Non-crystalline solids*, vol. 351, no. 27, pp. 2210–2216, 2005.

[21] S. M. Oh, "Effects of gasses on E-glass fibers," PhD thesis, Iowa State University, 1975.

[22] A. Alessi, S. Girard, C. Marcandella, M. Cannas, A. Boukenter, and Y. Ouerdane, "Raman investigation of the drawing effects on Ge-doped fibers," *Journal of Non-Crystalline Solids*, vol. 357, no. 1, pp. 24–27, Jan 2011.

[23] M. Lancry, E. Regnier, and B. Poumellec, "Fictive temperature in silica-based glasses and its application to optical fiber manufacturing," *Progress in Materials Science*, vol. 57, no. 1, pp. 63–94, Jan 2012.

[24] M. Dutreilh-Colas, A. Canizares, A. Blin, S. Ory, and P. Simon, "In situ Raman diagnostic of structural relaxation times of silica glasses," *Journal of the American Ceramic Society*, vol. 94, no. 7, pp. 2087–2091, 2011.

[25] F. L. Galeener and A. Geissberger, "Vibrational dynamics in Si 30-substituted vitreous SiO_2," *Physical Review B*, vol. 27, no. 10, p. 6199, 1983.

[26] D. Goller, R. Phillips, and I. Sayce, "Structural relaxation of SiO_2 at elevated temperatures monitored by in situ Raman scattering," *Journal of Non-Crystalline Solids*, vol. 355, no. 34, pp. 1747–1754, 2009.

[27] G. S. Henderson, D. R. Neuville, B. Cochain, and L. Cormier, "The structure of GeO_2-SiO_2 glasses and melts: A Raman spectroscopy study," *Journal of Non-Crystalline Solids*, vol. 355, no. 8, pp. 468 – 474, Apr 2009.

[28] M. Celikin, D. Barba, B. Bastola, A. Ruediger, and F. Rosei, "Development of regenerated fiber Bragg grating sensors with long-term stability," *Optics Express*, vol. 24, no. 19, p. 21897, Sep 2016.

[29] M. Fokine, "Photosensitivity, chemical composition gratings, and optical fiber based components," PhD thesis, Royal Institute of Technology, 2002.

[30] B. Zhang and M. Kahrizi, "High-temperature resistance fiber Bragg grating temperature sensor fabrication," *IEEE Sensors Journal*, vol. 7, no. 4, pp. 586–591, Apr 2007.

[31] P. S. Russell, "Photonic-crystal fibers," *Journal of Lightwave Technology*, vol. 24, no. 12, pp. 4729–4749, Dec 2006.

[32] C. B. Carter and M. G. Norton, *Ceramic Materials*. Springer New York, 2007.

[33] O. Butov, K. Golant, A. Tomashuk, M. van Stralen, and A. Breuls, "Refractive index dispersion of doped silica for fiber optics," *Optics Communications*, vol. 213, no. 4-6, pp. 301–308, Dec 2002.

[34] K. Saito and A. Ikushima, "Effects of fluorine on structural relaxation, and absorption edge in silica glass," *Jorunal of Applied Physics*, vol. 91, no. 8, pp. 4886–4890, Apr 2002.

[35] R. Engelbrecht, *Nichtlineare Faseroptik*. Springer Berlin Heidelberg, 2015.

[36] J. F. Shackelford and R. H. Doremus, Eds., *Ceramic and Glass Materials*. Springer Science+Business Media, LLC, 2008.

[37] M. Micoulaut, L. Cormier, and G. S. Henderson, "The structure of amorphous, crystalline and liquid GeO_2," *Journal of Physics: Condensed Matter*, vol. 18, no. 45, pp. R753–R784, Oct 2006.

[38] V. Swamy, S. K. Saxena, B. Sundman, and J. Zhang, "A thermodynamic assessment of silica phase diagram," *Journal of Geophysical Research*, vol. 99, no. B6, pp. 11 787–11 794, Jun 1994.

[39] S. K. Sharma, D. W. Matson, J. A. Philpotts, and T. L. Roush, "Raman study of the structure of glasses along the join SiO_2:GeO_2," *Journal of Non-Crystalline Solids*, vol. 68, no. 1, pp. 99–114, Oct 1984.

[40] N. Shimodaira, K. Saito, and A. Ikushima, "Raman spectra of fluorine-doped silica glasses with various fictive temperatures," *Journal of Applied Physics*, vol. 91, no. 6, pp. 3522–3525, Mar 2002.

[41] A. Q. Tool, "Relaxation between inelastic deformability and thermal expansion of glass in its annealing range," *Journal of American Ceramic Society*, vol. 29, no. 9, pp. 240–253, Sep 1946.

[42] D. P. Hand and P. S. J. Russell, "Photoinduced refractive-index changes in germanosilicate fibers," *Optics Letters*, vol. 15, no. 2, p. 102, Jan 1990.

[43] M. M. Broer, R. L. Cone, and J. R. Simpson, "Ultraviolet-induced distributed-feedback gratings in Ce^{3+}-doped silica optical fibers," *Optics Letters*, vol. 16, no. 18, p. 1391, Sep 1991.

[44] A. Othonos and K. Kalli, *Fiber Bragg Gratings: Fundamentals and Applications in Telecommunications and Sensing*. ARTECH HOUSE INC, 1999.

[45] V. B. Neustruev, "Colour centres in germanosilicate glass and optical fibres," *Journal of Physics: Condensed Matter*, vol. 6, no. 35, pp. 6901–6936, Aug 1994.

[46] M. J. Yuen, "Ultraviolet absorption studies of germanium silicate glasses," *Applied Optics*, vol. 21, no. 1, p. 136, Jan 1982.

[47] F. Bridges, G. Davies, J. Robertson, and A. M. Stoneham, "The spectroscopy of crystal defects: a compendium of defect nomenclature," *Journal of Physics: Condensed Matter*, vol. 2, no. 13, pp. 2875–2928, Apr 1990.

[48] T.-E. Tsai, G. M. Williams, and E. J. Friebele, "Index structure of fiber Bragg gratings in Ge–SiO$_2$ fibers," *Optics Letters*, vol. 22, no. 4, p. 224, Feb 1997.

[49] P. Kaiser, "Drawing-induced coloration in vitreous silica fibers," *Journal of the Optical Society of America*, vol. 64, no. 4, p. 475, Apr 1974.

[50] Y. Hibino and H. Hanafusa, "ESR study on E'-centers induced by optical fiber drawing process," *Japanese Journal of Applied Physics*, vol. 22, no. Part 2, No. 12, pp. L766–L768, Dec 1983.

[51] C. Dalle, P. Cordier, C. Depecker, P. Niay, P. Bernage, and M. Douay, "Growth kinetics and thermal stability of UV-induced H-bearing species in hydrogen loaded germanosilicate glasses," in *Bragg Gratings, Photosensitivity, and Poling in Glass Waveguides.* OSA, 1999.

[52] J.-W. Hong, S.-R. Ryu, M. Tomozawa, and Q. Chen, "Investigation of structural change caused by UV irradiation of hydrogen-loaded ge-doped core fiber," *Journal of Non-Crystalline Solids*, vol. 349, pp. 148–155, Dec 2004.

[53] V. Grubsky, D. S. Starodubov, and J. Feinberg, "Photochemical reaction of hydrogen with germanosilicate glass initiated by 3.4–5.4 eV ultraviolet light," *Optics Letters*, vol. 24, no. 11, p. 729, Jun 1999.

[54] F. Goutaland, H. Kuswanto, A. Yahya, A. Boukenter, and Y. Ouerdane, "Luminescence spectroscopy of hydrogen-associated defects in hydrogen-loaded and heated germanosilicate optical fibres," *Philosophical Magazine B*, vol. 79, no. 11/12, pp. 2137–2143, Nov 1999.

[55] J. Shelby, "Radiation effects in hydrogen-impregnated vitreous silica," *Journal of Applied Physics*, vol. 50, no. 5, pp. 3702–3706, 1979.

[56] B. Greene, D. Krol, S. Kosinski, O. Lemaire, and P. Saeta, "Thermal and photo-initiated reactions of H$_2$ with germanosilicate fibers," *Journal of Non-Crystalline Solids*, vol. 168, pp. 195–199, 1994.

[57] N. F. Borrelli, C. Smith, D. C. Allan, and T. P. Seward, "Densification of fused silica under 193-nm excitation," *Journal of the Optical Society of America B*, vol. 14, no. 7, p. 1606, Jul 1997.

[58] C. Smith, N. Borelli, J. Price, and D. Allan, "Excimer laser-induced expansion in hydrogen-loaded silica," *Applied Physics Letters*, vol. 78, no. 17, pp. 2452–2454, Apr 2001.

[59] N. H. Ky, H. G. Limberger, R. P. Salathé, F. Cochet, and L. Dong, "Hydrogen-induced reduction of axial stress in optical fiber cores," *Applied Physics Letters*, vol. 74, no. 4, pp. 516–518, Jan 1999.

[60] S. J. Mihailov, "Fiber Bragg grating sensors for harsh environments," *Sensors*, vol. 12, no. 2, pp. 1898–1918, 2012.

[61] Q. Chai, J. Zhang, J. Yang, J. Canning, G. Peng, Y. Chen, and L. Yuan, "Thermo-optic coefficient dependent temperature sensitivity of FBG-in-SMS based sensor," in *24th International Conference on Optical Fibre Sensors*, H. J. Kalinowski, J. L. Fabris, and W. J. Bock, Eds.   SPIE, Sep 2015.

[62] G. Ghosh, "Model for the thermo-optic coefficients of some standard optical glasses," *Journal of Non-Crystalline Solids*, vol. 189, no. 1-2, pp. 191–196, Aug 1995.

[63] K. O. Hill, Y. Fujii, D. C. Johnson, and B. S. Kawasaki, "Photosensitivity in optical fiber waveguides: Application to reflection filter fabrication," *Applied Physics Letters*, vol. 32, no. 10, pp. 647–649, May 1978.

[64] J. Albert, M. Fokine, and W. Margulis, "Grating formation in pure silica-core fibers," *Optics Letters*, vol. 27, no. 10, p. 809, May 2002.

[65] D. Williams and R. Smith, "Accelerated lifetime tests on UV written intra-core gratings in boron germania codoped silica fibre," *Electronics Letters*, vol. 31, no. 24, pp. 2120–2121, Nov 1995.

[66] S. Kannan, J. Guo, and P. Lemaire, "Thermal stability analysis of UV-induced fiber Bragg gratings," *Journal of Lightwave Technology*, vol. 15, no. 8, pp. 1478–1483, 1997.

[67] S. Baker, H. Rourke, V. Baker, and D. Goodchild, "Thermal decay of fiber Bragg gratings written in boron and germanium codoped silica fiber," *Journal of Lightwave Technology*, vol. 15, no. 8, pp. 1470–1477, 1997.

[68] G. Brambilla and H. Rutt, "Fiber Bragg gratings with enhanced thermal stability," *Applied Physics Letters*, vol. 80, no. 18, pp. 3259–3261, May 2002.

110

[69] C. G. Askins, G. M. Williams, M. Bashkansky, and E. J. Friebele, "Fiber Bragg reflectors by single excimer pulse," in *Fiber Optic Smart Structures and Skins V*, vol. 1798. International Society for Optics and Photonics, 1993, pp. 66–72.

[70] J. L. Archambault, L. Reekie, and P. S. J. Russell, "100% reflectivity Bragg reflectors produced in optical fibres by single excimer laser pulses," *Electronics Letters*, vol. 29, no. 5, pp. 453–455, 1993.

[71] K. Cook, L.-Y. Shao, and J. Canning, "Regeneration and helium: regenerating Bragg gratings in helium-loaded germanosilicate optical fibre," *Optical Materials Express*, vol. 2, no. 12, p. 1733, Nov 2012.

[72] J. Canning, E. Lindner, K. Cook, C. Chojetzki, S. Bruckner, M. Becker, M. Rothhardt, H. Bartelt, and K. Chen, "Regeneration of gratings by post-H_2 loading," in *2011 International Quantum Electronics Conference (IQEC) and Conference on Lasers and Electro-Optics (CLEO) Pacific Rim incorporating the Australasian Conference on Optics, Lasers and Spectroscopy and the Australian Conference on Optical Fibre Technology.* Institute of Electrical and Electronics Engineers (IEEE), Aug 2011.

[73] E. Haddad, R. Kruzelecky, K. Tagziria, B. Aissa, I. McKenzie, A. Guelhan, J.-M. Muylaert, M. Celinkin, and D. Barba, "High temperature optical fiber sensor for atmospheric reentry," in *International Conference on Space Optics—ICSO 2016*, vol. 10562. International Society for Optics and Photonics, 2017, p. 105620Z.

[74] G. Adamovsky, D. Varga, and B. Floyd, "Development and performance evaluation of optical sensor for high temperature engine applications," in *AIAA Infotech@ Aerospace 2010*, 2011, p. 3310.

[75] M. Fokine, "Formation of thermally stable chemical composition gratings in optical fibers," *JOSA B*, vol. 19, no. 8, pp. 1759–1765, 2002.

[76] ——, "Underlying mechanisms, applications, and limitations of chemical composition gratings in silica based fibers," *Journal of Non-Crystalline Solids*, vol. 349, pp. 98–104, 2004.

[77] J. Canning, S. Bandyopadhyay, M. Stevenson, and K. Cook, "Fiber Bragg grating sensor for high temperature application," in *Opto-Electronics and Communications Conference, 2008 and the 2008 Australian Conference on Optical Fibre Technology. OECC/ACOFT 2008. Joint conference of the.* IEEE, 2008, pp. 1–2.

[78] S. Bandyopadhyay, J. Canning, M. Stevenson, and K. Cook, "Ultrahigh-temperature regenerated gratings in boron-codoped germanosilicate optical fiber using 193 nm," *Optics letters*, vol. 33, no. 16, pp. 1917–1919, 2008.

[79] P. Holmberg, F. Laurell, and M. Fokine, "Influence of pre-annealing on the thermal regeneration of fiber Bragg gratings in standard optical fibers," *Optics Express*, vol. 23, no. 21, pp. 27 520–27 535, 2015.

[80] R. H. Doremus, "Diffusion of water in silica glass," *Journal of Materials Research*, vol. 10, no. 9, pp. 2379–2389, 1995.

[81] B. Poumellec, P. Bernage, and I. F. Riant, "Mechanisms of refractive index change under UV irradiation in some doped SiO_2 core optical fibers," in *Doped Fiber Devices*, M. J. F. Digonnet and F. Ouellette, Eds. SPIE, Nov 1996.

[82] S. Wiederhorn, S. Freiman, E. Fuller Jr, and C. Simmons, "Effects of water and other dielectrics on crack growth," *Journal of Materials Science*, vol. 17, no. 12, pp. 3460–3478, 1982.

[83] P. Ostojic, "Stress enhanced environmental corrosion and lifetime prediciton modelling in silica optical fibres," *Journal of Materials Science*, vol. 30, no. 12, pp. 3011–3023, Jun 1995.

[84] W. Demtröder, *Laserspektroskopie: Grundlagen und Techniken (German Edition)*. Springer, 2007.

[85] L. Yadav, *Organic Spectroscopy*. Springer Netherlands, 2005.

[86] W. W. Parson, *Modern Optical Spectroscopy*. Springer Berlin Heidelberg, 2007.

[87] D. A. Long, *The Raman Effect: A Unified Treatment of the Theory of Raman Scattering by Molecules*. Wiley, 2001.

[88] A. Pasquarello and R. Car, "Identification of Raman defect lines as signatures of ring structures in vitreous silica," *Physical Review Letters*, vol. 80, no. 23, pp. 5145–5147, Jun 1998.

[89] W. S. Yoo, J. H. Kim, and S. M. Han, "Multiwavelength Raman characterization of silicon stress near through-silicon vias and its inline monitoring applications," *Journal of Micro/Nanolithography, MEMS, and MOEMS*, vol. 13, no. 1, p. 011205, Feb 2014.

[90] S. Wartewig, *IR and Raman Spectroscopy*. Wiley-VCH Verlag GmbH & Co. KGaA, 2003.

[91] K. Awazu, H. Kawazoe, and K.-I. Muta, "Simultaneous generation of the 7.6 eV optical absorption band anf F_2 molecule in fluorine doped silica glass under annealing," *Journal of Applied Physics*, vol. 69, no. 8, pp. 4183–4188, Apr 1991.

[92] H. El Hamzaoui, M. Bouazaoui, and B. Capoen, "Raman investigation of germanium- and phosphorus-doping effects on the structure of sol-gel silica-based optical fiber preforms," *Journal of Molecular Structure*, vol. 1099, pp. 77–82, Nov 2015.

[93] S. A. Vasil'ev, E. M. Dianov, V. V. Koltashev, V. M. Marchenko, V. M. Mashinskii, O. I. Medvedkov, V. G. Plotnichenko, Y. N. Pyrkov, O. D. Sazhin, and A. A. Frolov, "Photoinduced changes in the Raman spectra of germanosilicate optical fibres," *Quantum Electronics*, vol. 28, no. 4, pp. 330–333, 1998.

[94] M. Takahashi, T. Uchino, and T. Yoko, "Correlation between macro- and microstructural changes in Ge:SiO_2 and SiO_2 glasses under intense ultraviolet irradiation," *Journal of the American Ceramic Society*, vol. 85, no. 5, pp. 1089–1092, May 2002.

[95] Corning, "Corning SMF-28 Optical Fiber," datasheet.

[96] P. Cordier, C. Dalle, C. Depecker, P. Bernage, M. Douay, P. Niay, J.-F. Bayon, and L. Dong, "Uv-induced reaction of h_2 with germanosilicate and aluminosilicate glasses," *Journal of Non-Crystalline Solids*, vol. 224, no. 3, pp. 277–282, Apr 1998.

[97] B. Bastola, B. Fischer, J. Roths, and A. Ruediger, "Qualitative photoluminescence study of defect activation in telecommunication fibers and Bragg gratings in hydrogen-loaded fibers," *Optical Materials*, vol. 81, pp. 134–139, 2018.

[98] ——, "Raman microstructural investigation of optical fiber at elevated temperature," *Optical Engineering*, vol. 56, no. 9, p. 097104, 2017.

[99] M. Lancry, K. Cook, B. Poumellec, and J. Canning, "Investigation of structural glass relaxation in regenerated fiber Bragg gratings," in *Nonlinear Photonics*. Optical Society of America, 2016, pp. JT4A–27.

[100] Nufern, "Photosensitive Single-Mode Fiber," datasheet.

[101] G. Adams, J. L. Margrave, and P. W. Wilson, "The preparation and some properties of a new germanium fluoride," *Journal of Inorganic and Nuclear Chemistry*, vol. 33, no. 5, pp. 1301–1306, May 1971.

Bibliography

[102] N. Shibata, M. Horigudhi, and T. Edahiro, "Raman spectra of binary high-silica glasses and fibers containing GeO_2, P_2O_5 and B_2O_3," *Journal of Non-Crystalline Solids*, vol. 45, no. 1, pp. 115–126, Jul 1981.

[103] F. Galeener, J. Mikkelsen Jr., R. Geils, and W. Mosby, "The relative Raman cross sections of vitreous SiO_2, GeO_2, B_2O_3, and P_2O_5," *Applied Physics Letters*, vol. 32, no. 1, pp. 34–36, Jan 1978.

[104] L. Polz, Q. Nguyen, H. Bartelt, and J. Roths, "Fiber Bragg gratings in hydrogen-loaded photosensitive fiber with two regeneration regimes," *Optics Communications*, vol. 313, pp. 128–133, Feb 2014.

[105] D. Williams, B. Ainslie, J. Armitage, R. Kashyap, and R. Campbell, "Enhanced UV photosensitivity in boron codoped germanosilicate fibres," *Electronics Letters*, vol. 29, no. 1, pp. 45–47, Jan 1993.

[106] A. Trukhin, J. Jansons, H.-J. Fitting, T. Barfels, and B. Schmidt, "Cathodo-luminescence decay kinetics of Ge^+, Si^+, o^+ implanted SiO_2 layers," *Journal of Non-Crystalline Solids*, vol. 331, no. 1-3, pp. 91–99, Dec 2003.

[107] K. Awazu, K.-I. Muta, and H. Kawazoe, "Formation mechanism of hydrogen-associated defect with an 11.9 mT doublet in electron spin resonance and red luminescence in $9SiO_2$:GeO_2 fibers," *Journal of Applied Physics*, vol. 74, no. 4, pp. 2237–2240, Jun 1993.

[108] D. Poulios, J. Spoonhower, and N. Bigelow, "Influence of oxygen deficiencies and hydrogen-loading on defect luminescence in irradiated Ge-doped silica glasses," *Journal of Luminescence*, vol. 101, no. 1-2, pp. 23–33, Jan 2003.

[109] Y. Maeda, "Visible photoluminescence from nanocrystallite Ge embedded in a glassy SiO_2 matrix: Evidence in support of the quantum-confinement mechanism," *Physical Review B*, vol. 51, no. 3, pp. 1658–1670, Jan 1995.

[110] S. Okamoto and Y. Kanemitsu, "Photoluminescence properties of surface-oxidized ge nanocrystals: Surface localization of excitons," *Physical Review B*, vol. 54, no. 23, pp. 16 421–16 424, Dec 1996.

[111] K.-I. Kawamura, H. Hosono, and H. Kawazoe, "Proton-implantation-induced nanosized Ge crystal formation in SiO_2:GeO_2 glasses," *Journal of Applied Physics*, vol. 80, no. 3, pp. 1357–1363, Aug 1996.

[112] A. N. Trukhin, "Localized states in germanate glasses. study of luminescence," *Journal of Non-Crystalline Solids*, vol. 189, no. 3, pp. 291–296, Aug 1995.

[113] D. Fink, J. Krauser, D. Nagengast, T. A. Murphy, J. Erxmeier, L. Palmetshofer, D. Bräunig, and A. Weidinger, "Hydrogen implantation and diffusion in silicon and silicon dioxide," *Applied Physics A*, vol. 61, no. 4, pp. 381–388, 1995.

[114] A. Revesz, "The role of hydrogen in SiO$_2$ films on silicon," *Journal of the Electrochemical Society*, vol. 126, no. 1, pp. 122–130, 1979.

[115] H. Itoh, Y. Ohmori, and M. Nakahara, "Loss increases due to chemical reactions of hydrogen in silica glass optical fibers," *Journal of lightwave technology*, vol. 3, no. 5, pp. 1100–1104, 1985.